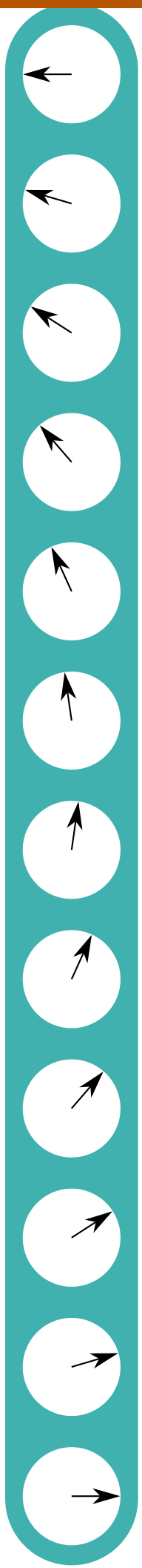

Inelastic scanning tunneling spectroscopy: magnetic excitations on the nanoscale

Timofey Balashov

Universität Karlsruhe (TH), Physikalisches Institut

January 2009

Inelastic scanning tunneling spectroscopy : magnetic excitations on the nanoscale

Zur Erlangung des akademischen Grades eines
DOKTORS DER NATURWISSENSCHAFTEN
vor der Fakultät für Physik der
Universität Karlsruhe (TH)

genehmigte

DISSERTATION

von

Dipl.-Phys. Timofey Balashov
aus Moskau, Russland

Tag der mündlichen Prüfung 13. Februar 2009

Referent Prof. Dr. Wulf Wulfhekel
Korreferent Prof. Dr. Georg Weiß

Contents

Chapter 1

Introduction

The last twenty years have seen an unprecedented rise in the interest to magnetic nanostructures and their interaction with the electric current. From the discovery of the giant magnetoresistance (GMR) effect in 1988 [1, 2], this field has been constantly developing and novel systems have been explored and exploited. Hand in hand with the progress in the fundamental understanding of the physics of the magnetic state went the technological advances in magnetic data storage, increasing the storage density by a factor of ten every five years by incorporating a lot of the results of the fundamental research [3]. The GMR is still used in modern hard disks and shows no sign of recessing, but the miniaturisation trend starts to reach its limits. Already magnetic bits of $25 \times 80\,\mathrm{nm}^2$ are used [4], and the magnetic stability starts to be an issue. When a magnetic system shrinks to a size of a hundred of atoms, its behaviour is hardly describable by a macroscopic model, such as the one used to explain the GMR and current-driven magnetisation reversal [5]. The interaction of an electric current with a magnetic cluster has to be tracked down to single electrons and elementary excitations of the magnetic system, i.e. *magnons* or *spin waves*. And here lies a problem: the interesting systems are not fully accessible with the theoretical or experimental approaches. The magnetic systems in question are too big to be calculated *ab initio* while fully accounting both for magnetic and electron-electron interactions. At the same time most of the experimental techniques used to investigate spin waves have difficulties when working with very small systems.

There are several established methods for the investigation of spin waves. They can be classified by the interaction used to excite spin waves. One of these techniques is neutron scattering. A neutron carries a magnetic moment, which couples to the magnetisation of the sample. An interaction between a neutron and a magnetic system can then lead to a transfer of angular momentum and to excitation or annihilation of magnons. The first investigation of spin waves with this technique dates back to 1957, when spin waves in magnetite were observed [6]. The measurement method allows one to register both the energy and momentum loss of the incident neutron, so the magnon dispersion was measured with this method

for most of the significant materials. The method has a good energy resolution of 0.1 meV, but the highest measurable energy is normally limited to a hundred meV, depending on the neutron source and the monochromator. The biggest limitation of the method is, however, a weak interaction of neutrons with matter, requiring macroscopic samples. For some systems that cannot be stabilised in the bulk (like fcc Co or fct Mn) one even has to change the composition of the crystal by adding stabilising admixtures. This limitation makes the investigation of spin waves a challenge already in thin magnetic films, and only a few studies deal with such systems [7].

Another technique, namely Brillouin light scattering, uses photons as interacting particles [8]. When light is shone on a magnetic sample, the interaction of photons with the magnetisation through changes of magneto-optical coupling can lead to creation and annihilation of magnons. However, the accessible wavevectors in this case are limited by the wavevector of the incident light, and cover only the lower part of the Brillouin zone. The spatial resolution of the method is also limited and so far this method has mostly been applied to bulk materials and thin magnetic films.

A similar technique, called ferromagnetic resonance, uses higher energy microwave photons to excite the magnetic waves [9]. Although the accessible energy range for this technique is higher, the wavevector limitation persists, rendering the method incapable of studying excitations in really small systems.

Another idea is to use the electron as the scattering particle, as implemented in the experimental method called spin-polarised electron energy loss spectroscopy [10]. Here a spin-polarised electron beam is shone onto the sample, resulting in magnon creation via spin flips of the incident electrons and a corresponding spin exchange between the electron and the magnetic system. This technique has a good energy resolution and can access the whole Brillouin zone. However, the smallest system that can be investigated is that of a thin film, due to the limits of focusing the electron beam.

In this work, we explore yet another technique, that also uses the electron as the interacting particle, but provides a better control of the measurement location. This technique is scanning tunnelling microscopy, combined with the inelastic scanning tunnelling spectroscopy (ISTS). The high lateral resolution of the scanning tunneling microscope (STM) allows one to find an exact position on the surface with a sub-Angström precision, so that the electrons tunnel at an exact location, and the energy of an inelastic excitation in the sample, such as a magnon, is determined with ISTS. ISTS has been successfully applied to studies of the vibrational modes of individual molecules [11] with a high energy resolution and a noticeable chemical contrast. Investigations of magnetic properties of nanosystems have also been conducted with inelastic tunnelling spectroscopy [12]. The systems used in these experiments are placed on an insulating layer to increase the intensity of the inelastic features. That, however, prohibits magnetisation dynamics studies. In this work all the investigated systems are fully metallic and closer to applications.

ISTS has a decent energy resolution of the order of meV and access to the lifetimes of the excited states. The wavevector is not directly accessible, but, as will be shown in Chapter 5, under certain assumptions, even this parameter can be determined. The ISTS has no upper energy limitations, meaning that the whole Brillouin zone is accessible for the measurement.

This thesis shows the capabilities of STM and ISTS when applied to magnon investigation. We show magnon excitations in six different magnetic systems, ranging from bulk magnets to single magnetic atoms, and explore the advantages and limitations of this new technique. Chapter 2 deals with the basics of STM and ISTS and describes a general mechanism for magnon creation and annihilation. Chapter 3 addresses the experimental setup and measuring conditions. Chapter 4 shows general results of magnon creation in a simple bulk magnetic system and explores the mechanism of electron-magnon interaction. In Chapter 5 the dimensionality of the investigated systems is reduced, and the access to magnon wavevector through quantisation of magnon modes in thin magnetic films is discussed. Chapter 6 exposes the nature of magnetic excitations in single magnetic atoms and clusters and presents the most elementary magnetic excitation. The last chapter summarises the work and proposes a way further.

All the first-principles calculations used in this work have been done by A. Ernst and coworkers from the Max-Plank-Institute for Microstructure Physics in Halle, Germany. Specifically, densities of states of bulk and thin film systems for Chapter 4 as well as the RKKY potential shape have been calculated by M. Däne, magnon densities for Ni/Cu(100) in Chapter 5 by P. Buczek and L. Sandratskii, and single Fe and Co atoms potentials on Pt(111), spin magnetic moments of these atoms and their magnetic anisotropy in Chapter 6 by S. Ostanin and J. Henk.

Chapter 2

Theoretical framework

2.1 Principles of STM

The scanning tunnelling microscope (STM) is an acclaimed technique of nanometre-scale surface investigation [13]. The precision of the STM is largely due to the exponential dependence of the tunnelling current on the distance between two electrodes in vacuum: an atomically sharp tip and a conducting sample to be investigated.

In the simplest picture, tunnelling of electrons can be described by a motion of a plane wave in the potential on Fig. 2.1. The wave is partially reflected from the barrier, and partially transmitted. Inside the barrier the wave exponentially decays. The transmission of the barrier is given by $T = |D|^2$ for the wave function written in the form

$$\psi = \begin{cases} \mathrm{e}^{ikx} + R\,\mathrm{e}^{-ikx} & x < 0, \\ A\,\mathrm{e}^{-\varkappa x} + B\,\mathrm{e}^{\varkappa x} & 0 < x < a, \\ D\,\mathrm{e}^{ikx} & x > a, \end{cases} \tag{2.1}$$

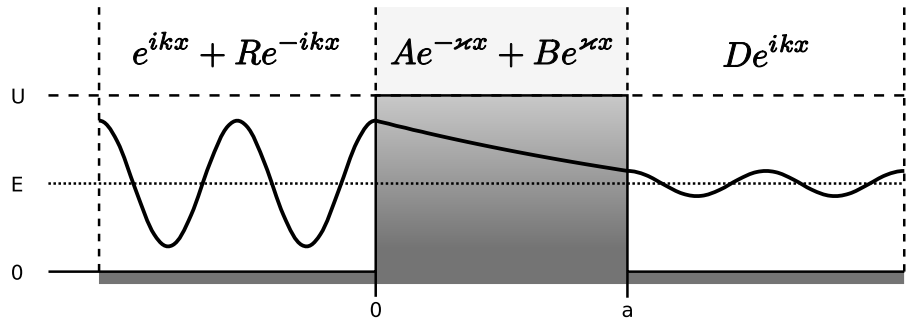

Figure 2.1: The simplest picture of a tunnelling junction.

where

$$k = \sqrt{2mE}/\hbar, \tag{2.2}$$

$$\varkappa = \sqrt{2m(U-E)}/\hbar. \tag{2.3}$$

and the individual parts of the wavefunction are solutions of the Schrödinger equation in the corresponding areas of the potential. By stitching wavefunction parts and their derivatives at $x = 0$ and $x = a$, one gets

$$T = |D|^2 = \left[1 + \frac{4k^2\varkappa^2}{(k^2+\varkappa^2)^2}\sinh^2 \varkappa a\right]^{-1}, \tag{2.4}$$

In the STM geometry $\mathrm{e}^{-\varkappa a} \ll 1$, and the above becomes

$$T \simeq \frac{16k^2\varkappa^2}{(k^2+\varkappa^2)^2}\,\mathrm{e}^{-2\varkappa a} \tag{2.5}$$

This function decays rapidly when the width of the barrier increases.

Although this can only be a rough description of the tunnelling in the STM, it does convey the main idea of STM operation. A sharp (ideally, atomically sharp, with a single atom at its apex) conducting tip is placed in vacuum, about a nanometre away from the sample surface. Then one applies an electric potential between the tip and the sample, and a tunnelling current arises. The current is proportional to the transmission coefficient above and therefore depends strongly on the tip-sample distance. For a metallic sample, $\varkappa$ is of the order of $1\,\text{Å}^{-1}$, meaning that a single atomic step (3 Å) on the surface increases the current by a factor of 10^3. So, when the tip moves along the surface, even sub-Angström changes in surface topography produce a noticeable change in the current. In a typical experiment scheme, called *constant current mode*, the changes in the current are immediately compensated by moving the tip perpendicular to the surface. Thus, the position of the tip mirrors the sample topography. The mechanism of tip and sample positioning has sub-Angström precision in all directions, allowing addressing individual atoms on the surface.

However, the tunnelling barrier model is insufficient to explain some of the features registered in the STM experiments, such as the chemical contrast. A more precise treatment of tunnelling between two electrodes was performed by Bardeen [14]. The current, regarded as a time-dependent perturbation, is given in the first order by

$$I = \frac{2\pi e}{\hbar}\sum_{\tau\sigma} f(E_\tau)[1 - f(E_\sigma + \mathrm{e}U)]|M_{\tau\sigma}|^2\delta(E_\tau - E_\sigma - \mathrm{e}U), \tag{2.6}$$

where the states τ and σ belong to different electrodes. Thus when a potential U is applied between the electrodes, electrons from state τ with energy E_τ can tunnel to a state σ with the same energy, with a probability given by the transmission

efficiency between the two states $|M_{\tau\sigma}|^2$ and by the population of the two states given by the Fermi function $f(E)$. Bardeen has shown that

$$M_{\tau\sigma} = \frac{\hbar^2}{2m} \int \left(\psi_\tau^* \vec{\nabla} \psi_\sigma + \psi_\sigma^* \vec{\nabla} \psi_\tau\right) \mathrm{d}\vec{S}, \tag{2.7}$$

where ψ_τ and ψ_σ are the wavefunctions of the corresponding states in the absence of tunnelling, and the integral is taken over any surface lying entirely within the barrier region. Further evaluation of $M_{\tau\sigma}$ is only possible for a fixed electrode geometry. For an STM this was first done by J. Tersoff and R. Hamann [15]. They have calculated the tunnelling current analytically in the limit of small voltages and temperatures for a locally spherical STM tip of radius r. If only the states close to the Fermi energy E_F contribute to tunnelling,

$$I \propto \rho_\tau(E_\mathrm{F}) \rho_\sigma(\vec{r}_0, E_\mathrm{F}) U \phi^4 \, \mathrm{e}^{2r\sqrt{2m\phi}/\hbar}, \tag{2.8}$$

where $\rho_\tau(E_\mathrm{F})$ is the tip density of states (DOS) at Fermi energy, $\rho_\sigma(\vec{r}_0, E_\mathrm{F})$ is the DOS of the sample at the centre of the tip sphere, and ϕ is the workfunction of the tip and the sample. ρ_σ can be more conveniently written in the form

$$\rho_\sigma(\vec{r}_0, E) = \rho_\sigma(E) T(E, U, s), \tag{2.9}$$

where s is the distance from the surface to tip centre, and $T(E, U, s)$ is the transmission coefficient, depending only on the properties of the tunnelling barrier. T decreases exponentially with tip-sample distance, conforming to the result obtained for a simple tunnelling barrier. This dependence has also been measured experimentally by Olesen *et al.* [16].

To account for larger biases, the current in Eq. 2.8 has to be integrated over all of the contributing states,

$$I \propto U \int_0^{eU} \rho_\tau(E_\mathrm{F} - eU + \epsilon) \rho_\sigma(E_\mathrm{F} + \epsilon) T(E_\mathrm{F} + \epsilon, U, s) d\epsilon, \tag{2.10}$$

where ϵ is the energy of the tunnelling electron with respect to E_F. In the case of flat tip and sample DOS, the current rises with voltage as

$$I \propto U\sqrt{\phi - \mathrm{e}U} \exp\left(-s/\hbar\sqrt{8m(\phi - \mathrm{e}U)}\right) \tag{2.11}$$

2.1.1 STM current with magnetic electrodes

The model above does not take into account the possible spin polarisation of the DOS, which will influence the tunnelling current when the tip and the sample are magnetic. If the magnetisations of tip and sample are collinear, one can strictly separate the two spin channels, assuming the spin of the electron does not change

during tunnelling[1]. Thus, for a parallel configuration, spin-up (spin-down) electrons from the tip tunnel into spin-up (spin-down) states of the sample and vice versa [17]:

$$I_{\uparrow\uparrow} \propto \rho_\tau^\uparrow \rho_\sigma^\uparrow + \rho_\tau^\downarrow \rho_\sigma^\downarrow,$$

In the antiparallel configuration the situation changes to the opposite, with spin-up electrons tunnelling to the spin-down states

$$I_{\uparrow\downarrow} \propto \rho_\tau^\uparrow \rho_\sigma^\downarrow + \rho_\tau^\uparrow \rho_\sigma^\downarrow$$

In case of arbitrary angle Θ between the magnetisations, the spin-up electrons can tunnel to both spin-up and spin-down states, with the probabilities of $\cos^2(\Theta/2)$ and $\sin^2(\Theta/2)$ respectively, leading to a general formula [5]

$$I(\Theta) = I_0(1 + P_\tau P_\sigma \cos\Theta),$$

where

$$P = \frac{\rho^\uparrow - \rho^\downarrow}{\rho^\uparrow + \rho^\downarrow} \tag{2.12}$$

defines the *spin polarisation* of the density of states.

2.2 Principles of STS

By studying the dependence of the tunnelling current on the bias voltage, one can greatly increase the amount of information that can be obtained with an STM. As follows from the Tersoff-Hamann model, $I(U)$ depends on the tip and sample densities of states, and one can extract them from the data obtained. It is much easier to do that from the first derivative of the tunnelling current $\mathrm{d}I/\mathrm{d}U$.

The first derivative of the tunnelling current in the Tersoff-Hamann model is

$$\begin{aligned}
\mathrm{d}I/\mathrm{d}U &\propto \frac{\mathrm{d}}{\mathrm{d}U}\int_0^{\mathrm{e}U} \rho_\tau(E_\mathrm{F} - \mathrm{e}U + \epsilon)\rho_\sigma(E_\mathrm{F} + \epsilon)T(\epsilon, U, s)d\epsilon \\
&= \rho_\tau(E_\mathrm{F})\rho_\sigma(E_\mathrm{F} + \mathrm{e}U)T(\mathrm{e}U, U, s) + \\
&\quad + \int_0^{\mathrm{e}U} \frac{\mathrm{d}}{\mathrm{d}U}\rho_\tau(E_\mathrm{F} - \mathrm{e}U + \epsilon)\rho_\sigma(E_\mathrm{F} + \epsilon)T(\epsilon, U, s)d\epsilon + \\
&\quad + \int_0^{\mathrm{e}U} \rho_\tau(E_\mathrm{F} - \mathrm{e}U + \epsilon)\rho_\sigma(E_\mathrm{F} + \epsilon)\frac{\mathrm{d}}{\mathrm{d}U}T(\epsilon, U, s)d\epsilon
\end{aligned}$$

The second and the third terms can be discarded in favour of the first one, assuming slowly changing $\rho_\tau(E)$ and $T(E, U, s)$ around E_F at small biases, such that $\mathrm{d}I/\mathrm{d}U$ is given by

$$\mathrm{d}I/\mathrm{d}U \propto \rho_\sigma(E_\mathrm{F} + \mathrm{e}U)$$

[1]This assumption is based on the conservation of angular momentum and on the absence of possible angular momentum sources/sinks in the tunnelling junction.

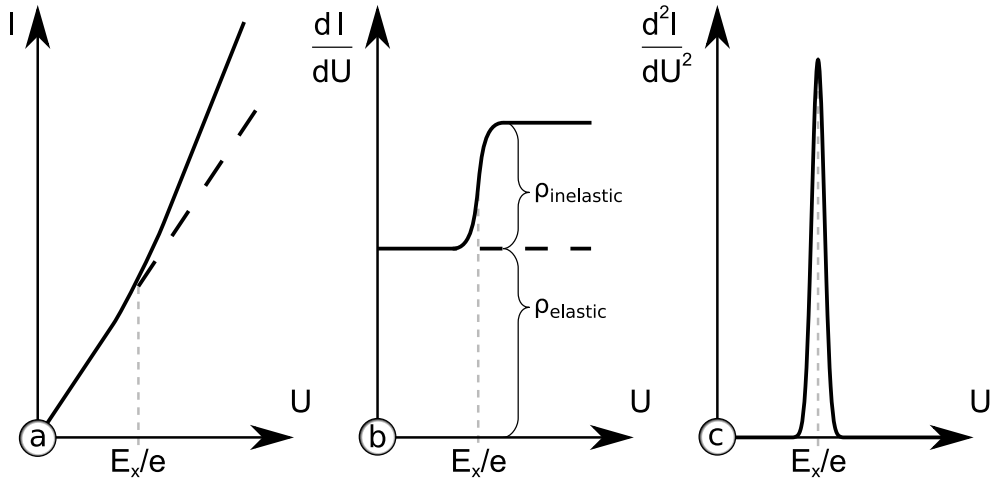

Figure 2.2: (a) $I(U)$, (b) $\mathrm{d}I/\mathrm{d}U$, and (c) $\mathrm{d}^2I/\mathrm{d}U^2$ in case of constant tip and sample DOS, with (solid line) and without (dashed line) an inelastic excitation of energy E_x.

2.2.1 Inelastic STS

The processes described so far correspond to elastic tunnelling, i.e. the final energy of the electron with respect to the Fermi edge is its starting energy plus the sample bias eU. However, this does not cover all the possible processes. The tunnelling electron can also lose energy by interacting with the tip or the sample. Such a process is called inelastic tunnelling, and has a distinct signature in the $I(U)$.

Let E_x be the inelastic process energy cost. Then at biases smaller than E_x/e and low temperatures all the electrons will tunnel elastically, as there will be no empty states at $E_\mathrm{F}+\mathrm{e}U-E_\mathrm{x}$ for the scattered electron to occupy. However, as soon as the E_x/e boundary is crossed, a second (inelastic) channel opens, i.e. more final states appear, the full DOS increases ($\rho = \rho_\mathrm{elastic} + \rho_\mathrm{inelastic}$), and the $I(U)$ shows a kink (see Fig. 2.2). The inelastic interaction cross-section is usually not very big, and thus the inelastic processes are better monitored in $\mathrm{d}I/\mathrm{d}U$ or $\mathrm{d}^2I/\mathrm{d}U^2$. The $\mathrm{d}I/\mathrm{d}U$ displays a step, and $\mathrm{d}^2I/\mathrm{d}U^2$ a peak at E_x/e [18]. In case the inelastic excitation can be created independently on the tunnelling direction, the features in the spectra will appear both for $U = +E_\mathrm{x}/\mathrm{e}$ and $U = -E_\mathrm{x}/\mathrm{e}$. For the $\mathrm{d}^2I/\mathrm{d}U^2$, the inelastic feature at negative bias appears as a dip.

A variety of excitations in the sample can be studied that way, including phonons [19, 20], plasmons [20], and magnons [21]. Unfortunately there is no easy way to distinguish between different kinds of excitations, as the produced spectral features are almost excitation-independent. One of the possible ways is the analysis of the excitation energy range, as it may be quite different for different excitation types. Another criterion is the cross-section of the excitation process, as the fraction of the inelastic contribution is immediately visible in the $\mathrm{d}I/\mathrm{d}U$ as the relationship between the step height ($\rho_\mathrm{inelastic}$) and the total DOS.

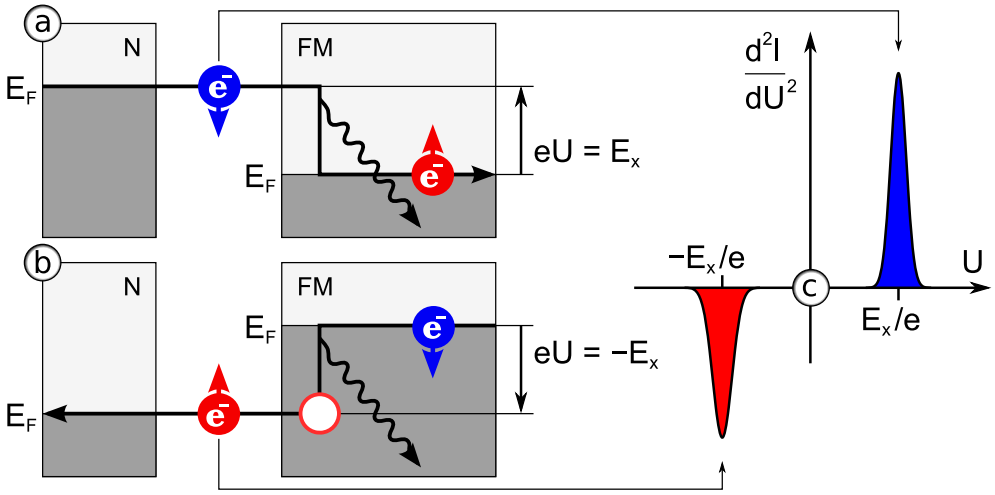

Figure 2.3: Magnon creation for two tunnelling directions. If the sample bias is positive and high enough, tunnelling minority electrons can scatter into majority states, creating magnons (a). This process is manifested by a peak in $\mathrm{d}^2I/\mathrm{d}U^2$ at $U = E_\mathrm{x}/\mathrm{e}$ (c). For negative bias, tunnelling majority electrons leave majority holes behind, that can in turn be filled with minority electrons leading again to magnon creation (b). A signature of this process is a dip in $\mathrm{d}^2I/\mathrm{d}U^2$ at $U = -E_\mathrm{x}/\mathrm{e}$ (c).

In case the excitations do not appear at discrete energies, but rather have a dispersion $\varepsilon(\vec{k})$ and a density of states $\rho_\mathrm{x}(\varepsilon)$, the picture is more complicated. For this case the cross-section $\Sigma(\varepsilon)$ of the excitation might also depend on energy. Thus, the probability $p(\varepsilon)$ of the inelastic process at the energy ε and respectively the shape of $\mathrm{d}^2I/\mathrm{d}U^2$, is given by

$$p(\varepsilon) = \rho_\mathrm{x}(\varepsilon) \cdot \Sigma(\varepsilon) \tag{2.13}$$

If the interaction potential of the hot electron with the sample or tip $\phi(\vec{r})$ is known, the cross-section can be calculated using the Born approximation [22]

$$\Sigma(q) = |\Phi(q)|^2, \tag{2.14}$$

where $\Phi(q)$ is the Fourier transform of $\phi(\vec{r})$. Transferring that into energy space yields

$$p(\varepsilon) = \rho_\mathrm{x}(\varepsilon)|\Phi(q(\varepsilon))|^2. \tag{2.15}$$

2.2.2 Exciting magnons with electrons

The aim of this work is to investigate the possibility of magnon creation in a tunnelling experiment. Magnons are elementary excitations of the magnetic subsystem of the material, classically depicted as propagating spin precession waves [23].

These quasiparticles are characterised by their energy and wavevector, and have a spin[2] of $-\hbar$, i.e. the creation of a magnon lowers the sample magnetisation by $2\mu_B$.

In the STM experiments of this work magnons are excited by electrons tunnelling between the tip and a magnetic sample. As the angular momentum of the system has to be conserved, the spin of the interacting electron has to change if the magnon is to be created or annihilated. An electron carries a spin of $\pm\frac{1}{2}\hbar$, so in case of magnon creation, the spin of the electron has to change from $-\frac{1}{2}\hbar$ (minority state) to $\frac{1}{2}\hbar$ (majority state), and in the opposite way for magnon annihilation.

As has been demonstrated in spin-polarised electron energy loss spectroscopy studies [10], magnon annihilation by electrons at room temperature can be neglected when compared to magnon creation. Possible reasons include short magnon lifetimes as compared to the tunnelling event frequency and low probability of thermal excitation of magnons. At 4 K thermal excitations are even less probable. Therefore, we only have to consider magnon creation, i.e. electron spin flips from minority to majority states. A magnon of energy E_x can be created if there is an occupied minority state at E_0 and an empty majority state at $E_0 - E_x$. Assuming a sharp Fermi edge so that all the states above E_F are unoccupied, such a situation occurs either when a minority electron tunnels into the sample to a state with energy higher than $E_F + E_x$, or when a majority electron tunnels out from a state with energy lower than $E_F - E_x$ (see Fig. 2.3). It follows that magnon creation happens independently of the tunnelling direction, but for forward, i.e. tip-to-sample tunnelling, it will occur only in the minority spin channel, and for backward tunnelling in the majority spin channel.

If one of the channels is dominant, i.e. the tunnelling current is spin-polarised, such than the amounts of tunnelling minority and majority electrons differ substantially, the probability of magnon creation will be affected. In this case one can expect a strong inelastic signal only for one tunnelling direction.

2.3 Magnons in different dimensions

The standard way to describe magnetic excitations in a localised spin picture is the Heisenberg Hamiltonian [24],

$$\mathcal{H} = -\sum_{i<j} J_{ij}\vec{S}_i\vec{S}_j,$$

where J_{ij} is the exchange constant between spins $\vec{S}_i$ and $\vec{S}_j$, given by the overlap between the electron wavefunctions. It drops quickly with distance, so the sum is usually taken only over nearest-neighbour pairs. Typical values of $J_{n.n.}$ are in the region of meV, e.g. 19.5 meV for bulk bcc iron and 14.8 meV for bulk fcc cobalt [25]. Note that in this description the dipolar interaction between the

[2]Here and further on, the sign of the spin is defined with respect to sample magnetisation. Thus, the minority electrons of the sample have a spin $-\frac{1}{2}\hbar$ and majority electrons a spin of $+\frac{1}{2}\hbar$.

spins has been neglected. Thus, this approach only considers the exchange interaction and leads to exchange-dominated spin waves. This assumption only holds for magnon wavevectors larger than $10^{-2}\,\text{Å}^{-1}$ [26], i.e. the model does not accurately describe magnons in the centre of the Brillouin zone, corresponding to energies lower than 1 meV. The energy resolution of our experiments is, however, about 2 meV, so only exchange-driven spin waves will have a noticeable influence on our results.

In a ferromagnet ($J > 0$) the eigenfunctions of this Hamiltonian can be written in the form

$$\Psi = \sum_m A_m S_-^m \left|\uparrow\right\rangle,$$

expressing a superposition of individual excited states (cf. Stoner excitations), where $\left|\uparrow\right\rangle$ is the ground state with maximum magnetisation.

2.3.1 3D

The eigenstates of the Schrödinger Hamiltonian for a periodical lattice of magnetic moments with $J > 0$ have a form

$$\left|\vec{q}\right\rangle = \frac{1}{\sqrt{2S}} \sum_m \mathrm{e}^{i\vec{q}\vec{R}_m} S_-^m \left|\uparrow\right\rangle,$$

where $\vec{q}$ plays a role of the excitation wavevector.

The corresponding energies are

$$E(\vec{q}) = E_0 + \hbar^2 JS \sum_{\vec{\delta}} \left(1 - \cos \vec{q}\vec{\delta}\right),$$

where E_0 is the energy of the ground state, and $\vec{\delta}$ iterates over nearest neighbours.

For small wavevectors $\left|\vec{q}\right| a \ll 1$ (with a denoting the lattice constant), the dispersion takes the form

$$E \approx E_0 + \hbar^2 JS \sum_{\vec{\delta}} \left(1 - 1 + (qa)^2/2\right) = E_0 + D_{\vec{q}} \left|\vec{q}\right|^2,$$

where D is called the *stiffness* of the spin wave. In general, D depends on the wave propagation direction, but is isotropic for a cubic lattice. D is equal to $\hbar^2 JSa^2$ for any cubic lattice with a lattice constant a. Typical values of D are of the order of hundreds meV·Å^2 [25].

2.3.2 2D

If the dimension of the system is reduced by only working with a thin magnetic film, the behaviour of the magnon dispersion changes. Wave propagation in the

direction perpendicular to the film plane is forbidden due to the presence of two interfaces with non-magnetic materials. This leads to a quantisation of magnon states.

A general form for the wavefunction is

$$\Psi = \sum_k A^k \sum_{j \text{ in } k} \mathrm{e}^{i\vec{q_\parallel}\vec{R}_j} S_-^j \left|\uparrow\right\rangle ,$$

where k enumerates the N atomic layers, j goes over individual spins in layer k and $q_\parallel$ is the in-plane wave vector. Solving the Schrödinger equation gives an $N \times N$ matrix, whose eigenvalues are the state energies and eigenvectors describe the behaviour of spins in individual layers (for more details see Section A.3.4). In the limit of small $q_\parallel$ a general solution exists, allowing the introduction of a quasi-wavevector $q_\perp$ in the perpendicular direction. This wavevector is quantised, such that

$$q_\perp = \frac{\pi}{a}\frac{n}{N}, n = 0, 1, \ldots, N-1$$

The corresponding energies are

$$E_n = 2z\hbar^2 JS(1 - \cos q_\perp a),$$

with a the interlayer distance and z the number of nearest neighbours in the layer for an atom from another layer. This description will be used later in Chapter 5.

2.3.3 0D

The Schrödinger equation is exactly solvable for rings and linear chains of interacting spins. A system with N atoms will have N states

$$E_\mathrm{x}^j = 2\hbar^2 JS(1 - \cos q_j a),$$

where a is the interatomic distance. The values q_j for $j = 0, 1, \ldots, N-1$ are

$$q_j = \frac{\pi}{a}\frac{j}{N}$$

for a linear chain and

$$q_j = \frac{\pi}{a}\frac{2j}{N}$$

for a ring.

This means that a single magnetic atom has only one excitation mode — a simple precession. If one increases the size of the cluster, the number of excited states will increase. A dimer has a second state at $E_\mathrm{x} = 2\hbar^2 JS$, a compact trimer has a double degenerate $E_\mathrm{x} = 3\hbar^2 JS$, and a linear trimer has the second state at $\hbar^2 JS$ and a third at $3\hbar^2 JS$. These results will be used in Chapter 6.

2.3.4 Magnetic anisotropy

The solution for every system mentioned above includes a mode with $E_{\mathrm{x}} = 0$, classically describable as a uniform rotation of all the moments in the system. In reality the energy of this excitation is not zero due to the magnetic anisotropy, present in virtually any magnetic system. The Heisenberg Hamiltonian is isotropic, i.e. the energy does not depend on the absolute orientation of individual spins, but rather on their relative orientations. This is a simplistic view, that takes into account neither the dipolar interaction between the neighbouring spins nor the spin-orbit interaction. Taking these contributions into account makes the Hamiltonian anisotropic; there is an energy cost for rotating the magnetisation and consequently the lowest magnon mode has $E_{\mathrm{x}} > 0$. In bulk systems like Fe, Co or Ni, the resulting gap is below $100\,\mu$eV, and will be disregarded in the experimental chapters of this work, as it is well below the experimental resolution. The gap is, however, more significant in systems of reduced dimensions, and can be accessed with ISTS.

In thin films and even more in adsorbed atoms and clusters, the magnetic anisotropy is defined by the uniaxial anisotropy term. The corresponding magnetic anisotropy energy (MAE) is classically defined as the energy required to rotate the magnetisation by 90 °. The value of the MAE depends strongly on the dimensionality of the system: it has been shown e.g. for cobalt that the MAE per atom changes from 0.04 meV for bulk Co through 0.14 meV for thin Co films on Pt(997) to 2.0 meV for Co chains on the same substrate [27] and 9.6 meV for Co atoms on Pt(111) [28]. This increase of MAE goes hand in hand with an increase of the orbital momentum and can therefore be explained as originating from the spin-orbit interaction [29].

To describe the effect of the magnetic anisotropy on the magnon dispersion, it is more useful to consider the quantum-mechanical anisotropy-related term of a general form $E_{\mathrm{anis}} = DS_z^2$. One can express the classical uniaxial MAE as the energy difference between the ground state $S_z = S$ and the state $S_z = 0$, giving a total of DS^2. A magnon only reduces the total spin by $\hbar$, so the energy of the lowest mode is not equal to the MAE, but has to be calculated from the total spin of the system. Magnetic anisotropy will therefore shift the whole magnon spectrum to higher energies, but as follows from the experimental MAE values, this shift is insignificant in large systems. In systems, consisting only on a few atoms, however, the shift is significant and will be used to determine the MAE from the excitation energies in Chapter 6.

Chapter 3

Experimental setup

Investigation of nanosystems requires an absolute cleanness of the investigated surfaces and total control of the composition of investigated materials. To achieve this, all experiments were performed in ultra-high vacuum (UHV), and the sample quality was monitored at all stages. A typical pressure in the apparatus was below $5 \cdot 10^{-11}$ mbar.

As shown in figure 3.1, the machine can be divided into three main parts — the loadlock (red), the preparation chamber (blue) and the STM chamber (green). The two-stage loadlock allows degassing of the samples at low pressures ($\approx 5 \cdot 10^{-9}$ mbar), before transferring them into the UHV chambers.

The preparation chamber was designed with study of thin magnetic films in mind. Simultaneous deposition of three different materials using molecular-beam epitaxy (MBE) is possible, as well as magneto-optic Kerr effect measurements of the magnetisation of resulting films. The chamber is equipped with an electron gun for electron diffraction studies and Auger spectroscopy. An ion gun for sputtering samples is also available.

3.1 Samples

After a new sample is introduced into the machine, it is left to degas in the high-vacuum stage of the loadlock, till a reasonable pressure is established. The sample is then transferred to the preparation chamber, where it is subjected to multiple cycles of sputtering and annealing. The sputtering with 1.5 keV Ar^+ ions for 60 to 90 minutes serves to remove the contaminants from the surface. After each sputtering procedure, the sample is annealed with an electron beam from a filament mounted behind the sample on the sample holder to remove residual Ar atoms and to smooth the surface. The annealing temperature and electron energy are different for different samples used in this study (see table 3.1 for details). In the first couple of cycles the annealing temperature is kept low, to prevent the diffusion of surface adsorbates into the sample.

After several such cycles, Auger spectroscopy is performed. Auger spectra are

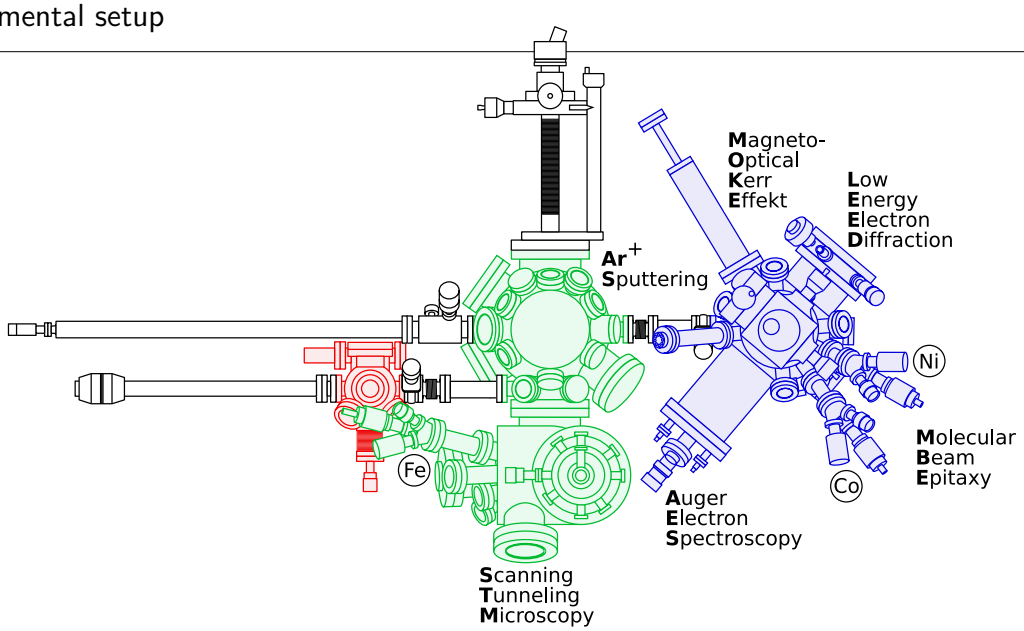

Figure 3.1: A top view of the experimental apparatus. The three main parts — loadlock system, preparation chamber and STM cryostat — are marked with red, blue and green, respectively.

compared to known data for clean materials, and the cycles are continued, till the spectra show no contamination. Low energy electron diffraction (LEED) is also performed, to ensure high crystallographic quality of the sample. The LEED pattern is compared to the expected pattern for the investigated crystal surface. Possible problems detectable in this way include graining, adsorbate superstructures and insufficient overall crystal quality [30].

When none of the methods reveal any surface contamination, the final check is done using the STM. The STM scans might reveal large-scale (dislocation bunches, terracing) as well as small-scale (individual adsorbates) irregularities on the surface. The cleaning process is continued up to the point where STM scans show a clean surface, with atomically flat areas at least $1000\,\mathrm{nm}^2$ in size.

To study a thin film magnetic system, magnetic material is deposited on the substrate, prepared as described before. The deposition is performed in the preparation chamber. The chamber construction allows cooling of the sample with liquid nitrogen, if low deposition temperature is needed. Sample temperature down to at least 200 K can be obtained.

Table 3.1: Main properties of samples used in the experiment.

Sample	Crystallographic structure	Annealing temperature
Fe(100)	bcc	850 K
Cu(100) & Cu(111)	fcc	750 K
Pt(111)	fcc	1100 K

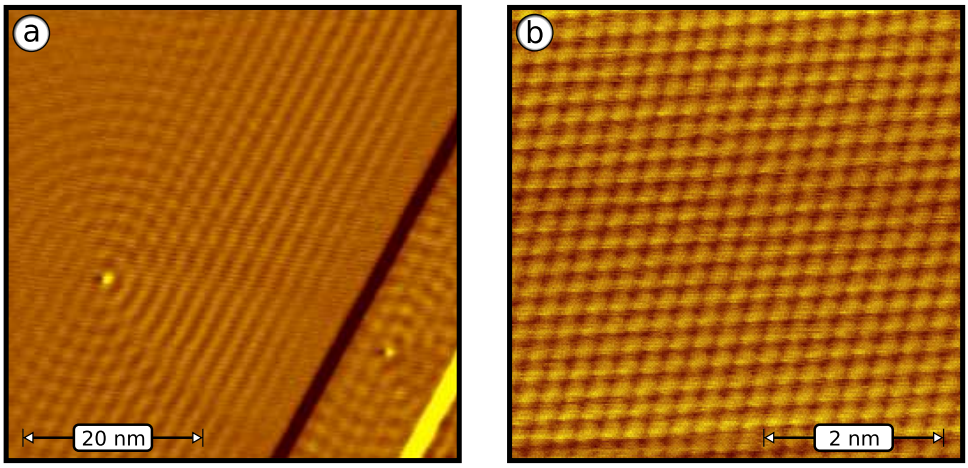

Figure 3.2: (a) A standing surface state on Cu(111). The picture does not represent topography, but a laterally resolved $\mathrm{d}I/\mathrm{d}U$ at 50 mV bias. (b) Atomically resolved Cu(111) surface. The hexagonal symmetry is not perfect due to a slight drift in x direction.

Fe, Co and Ni films used in the experiment were deposited from pure (99.9+ %) materials. The evaporators consist of a metal rod coaxial with a ring filament just in front of it. A high potential difference ($\approx$ 900 V) is applied between the rod and the filament to accelerate electrons emitted from the filament. A typical filament current is 2 A, a typical emission current 10 mA. Metal atoms, evaporated from the heated rod, can escape the evaporator inner space through a small opening of $\approx 5\,^\circ$. This metal gas is partially ionised by incident electrons and therefore an ion flux can be detected by a flux meter located in the opening. Typical flux currents are $\approx$ 30 nA, corresponding to the evaporation rate of 0.7 ML/min. The calibration of the deposition rate is performed in two ways: by either medium-energy electron diffraction (MEED) at grazing angles, or by estimating the deposited amount from an STM scan. The former method is more precise in case the material shows a layer-by-layer growth pattern. An electron beam is directed at the sample at angles about 2–3 $^\circ$ to the surface, resulting in several reflection maxima. The intensity of the maxima is monitored during deposition and varies depending on the roughness of the film, with a maximum for full coverage and a minimum for a half-filled layer, giving an oscillating signal during film growth.

3.2 Tips

The STM tips are first etched in air via electrochemical etching in 5 % NaOH from 400 μm thick tungsten wire. The estimated radius of the tip apex after etching is $\approx$ 10 nm. After being transferred into the vacuum and degassed, the tips are subjected to electron beam heating from a filament mounted on the transfer tipholder about 0.5 mm away from the tip. The acceleration potential is 800 V. For the first

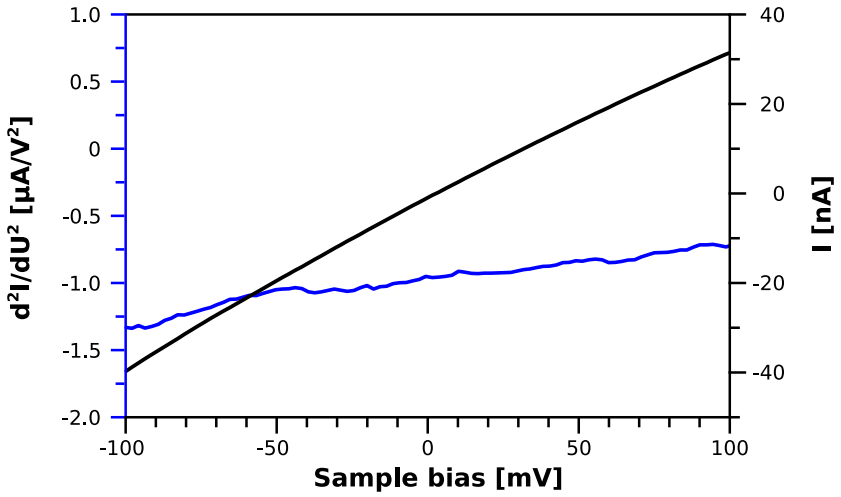

Figure 3.3: $I(U)$ and $\mathrm{d}^2I/\mathrm{d}U^2$ obtained on clean Cu(100). The $I(U)$ is linear and $\mathrm{d}^2I/\mathrm{d}U^2$ is flat within the noise level.

cycle the beam current is higher to achieve a slight melting of the tip apex. Subsequent treatment is just harsh enough to remove adsorbates from the tip. In the case of a strong suspected tip contamination, the tip is also sputtered with Ar^+ ions.

Tip cleanness is tested by measuring the tunnelling current $I(U)$ for a large bias range on a clean Cu(111) sample. The $\mathrm{d}^2I/\mathrm{d}U^2$ in the region from -1 to 1 V should be featureless, except for a surface electronic state at -350 mV. The current should show a linear dependence on bias above E_F. In case of a dirty tip, additional features might appear, and the $I(U)$ curve might show pronounced bends. The sharpness of the tip can be tested by imaging the Cu(111) surface state and reaching atomic resolution. See figures 3.2 and 3.3 for examples.

3.3 STM details

The STM is mounted inside the innermost shield of a He^4 cryostat. The STM temperature measured with a Pt1000 thermometer is 11.50 Ω, corresponding to 4.3 K.

The microscope used in the experiments is a home-built instrument. The materials used in the construction are non-magnetic, as to eliminate their possible effect on the investigated system. The sample stage has full freedom in the xy-plane, so the whole sample, about 6 mm in diameter, can be accessed with the STM tip.

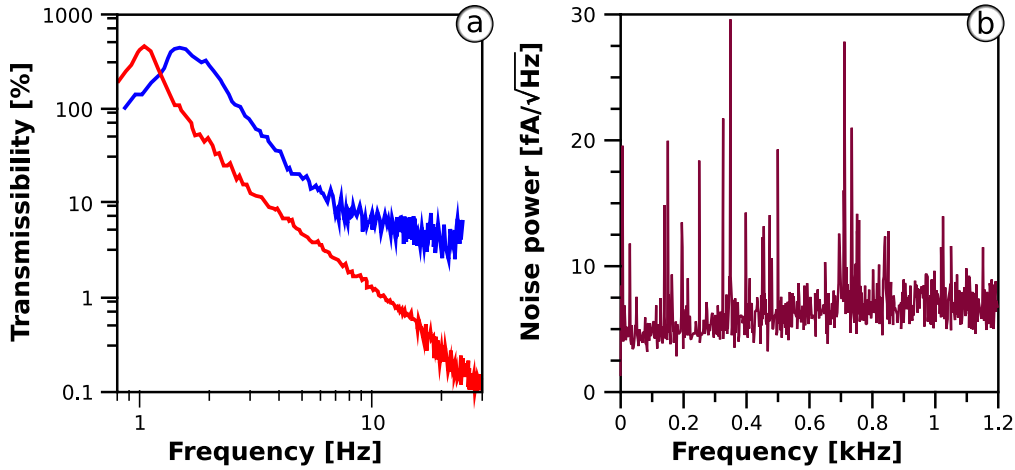

Figure 3.4: (a) Transmissibility curves of laminar-flow damping of vertical (red) and horizontal (blue) vibrations. (b) The noise level of the STM setup with the tip far away from the sample.

3.3.1 Damping

To filter out external mechanical vibrations, the machine is placed on four Newport I-2000 pneumatic insulators with laminar-flow damping. Their construction ensures low horizontal and vertical vibration transmissibility in the frequency region down to 10 Hz (see Fig. 3.4a). As an additional damping stage, the STM hangs on four BeCu25 springs, with a resonant frequency of 2.5 Hz, weakening vertical mechanical vibrations originating from inside the machine from 4 Hz up.

Four superconducting NbTi coils ($T_C = 8.7\,K$) are built into the STM housing and can produce magnetic fields up to 500 mT on the vertical axis and up to 200 mT in-plane. These coils are also used as a damping system, since a magnetic field generates Eddy currents in the moving copper body of the STM, that effectively damp vibrations. A vertical magnetic field of 50 mT was used for damping in cases where such a field has only negligible effects on the magnetic properties of the investigated samples.

3.3.2 Noise level

The tunnelling current is amplified outside of the cryostat with a commercial low-noise IV-converter (DLPCA-200 by FEMTO Messtechnik GmbH). The amplification factor used in the experiment is between 10^6 and 10^9 V/A. Special care is taken to properly ground the machine and to avoid ground loops in the cabling. The final noise power is below $30\,fA/\sqrt{Hz}$ with an average value less than $7\,fA/\sqrt{Hz}$ (see Fig. 3.4b).

The STM electronics is a commercially available SPM 100 from RHK Technology. It is an analog SPM controller sampling with 16 bit sampling and the ability

to record up to 10 channels simultaneously. A lock-in amplifier (Physical instruments 5209) is used to obtain the first and the second derivatives of the tunnelling current. Modulation voltages from 1 to 30 mV were used throughout this work with the frequency slightly below the IV-converter bandwidth, i.e. around 10 kHz.

Chapter 4

Magnons in bulk

To start with a development of a new technique one needs a prototype system with unambiguous properties and uncomplicated behaviour. Such a system for the investigation of magnetic excitations is provided by an Fe(100) whisker. This single crystal has a simple domain structure and a low coercive field of $\approx 10\,\mu$T [31]. Magnon dispersion in Fe spans the energy region from 0 to 600 meV [25]. Using a bulk system is also important in the likely case that the probability of magnon excitation depends on the amount of magnetic material. The experiment was done with a non-magnetic W tip to have simple selection rules for magnon creation as described in Sect. 2.2.2.

The $\mathrm{d}^2I/\mathrm{d}U^2$ spectrum taken for a range ± 400 meV shows several well-noticeable features (Fig. 4.1a). Comparing the spectrum with the local density of states (DOS) (Fig. 4.1b), one can see that the overall shape of the curve can be related to the shape of the DOS. The two main features are a minority surface state at ≈ 300 meV as also reported e.g. by Stroscio *et al.* [32], and a volume band edge at -130 meV.

However, the region just around E_F is more difficult to explain. The DOS is practically featureless, but the $\mathrm{d}^2I/\mathrm{d}U^2$ between -50 and 50 mV (see Fig. 4.2a) is not constant. Instead, one can see a relatively complex structure, dominated by a peak at around $+5$ mV. One also observes a small counter-peak at -5 mV, and some additional modulation above 25 mV on both sides.

The flat DOS and the small width of the peak lead to a conclusion that this structure is a signature of an inelastic excitation. There are two questions: first, what is the nature of this excitation, and can it be of magnetic origin, and second, why is there such a striking difference between peaks for forward and backward tunnelling?

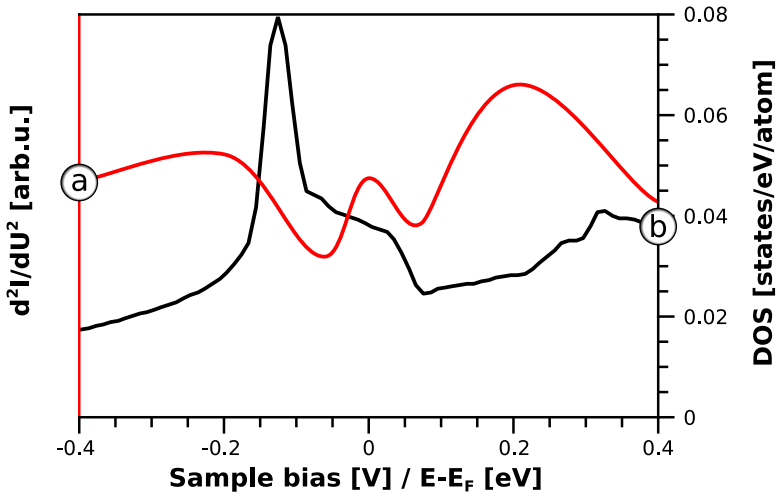

Figure 4.1: (a) $\mathrm{d}^2I/\mathrm{d}U^2$ taken with a W tip on Fe(100) whisker (30 mV modulation). (b) LDOS in STM geometry.

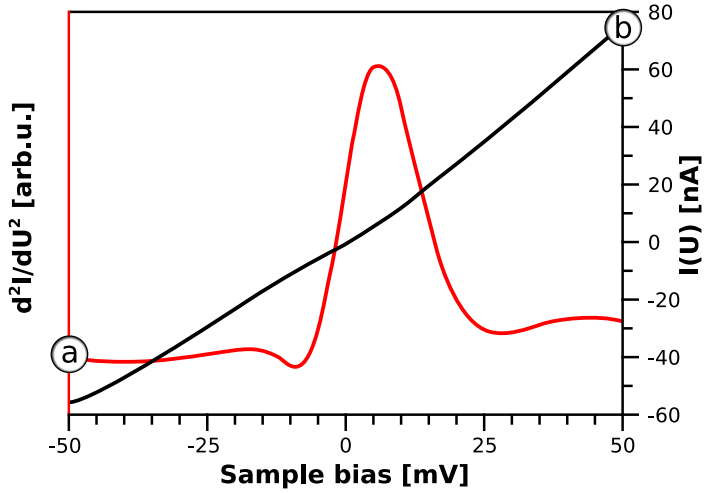

Figure 4.2: (a) $\mathrm{d}^2I/\mathrm{d}U^2$ and (b) $I(U)$ in a small energy range (1 mV modulation).

4.1 The nature of the peak

In the energy region of interest, that is, below 50 meV, only a small number of excitations exists. For example, the energy of plasmons is given by

$$E_{\mathrm{pl}} = \hbar\sqrt{\frac{\mathrm{e}^2 n_{\mathrm{e}}}{m_{\mathrm{eff}}\varepsilon_0}}, \tag{4.1}$$

where n_{e} is the charge carriers density and m_{eff} their effective mass. Taking into account that n_{e} is extremely large in metals (of the order of one electron per unit cell), E_{pl} evaluates to a few eV, immediately excluding the possibility of registering

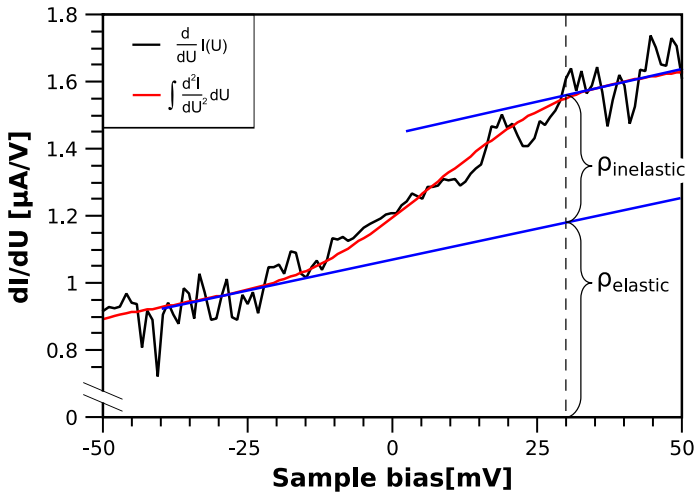

Figure 4.3: Calculation of the excitation cross-section. The numerically integrated $\mathrm{d}^2I/\mathrm{d}U^2$ (red) was fitted by scaling to the numerically differentiated $I(U)$ (black). The resulting curve was fitted with a linear regression (blue) at E_F and after the excitation. We neglect here the dip below E_F in $\mathrm{d}^2I/\mathrm{d}U^2$, as it is impossible to discern it in $\mathrm{d}I/\mathrm{d}U$. This can only result in a smaller cross-section.

plasmon excitations in our experiment.

This leaves two cases: phonons and magnons. Both exist in the meV region, and can be excited by electrons. Phonons have a linear dispersion up to $\approx 20\,\mathrm{meV}$, with the top of the band around 40 meV [33]. Magnons have a quadratic dispersion with a gap of less than 0.1 meV, with the top of the band at $\approx 600\,\mathrm{meV}$ [25]. However, the nature of the experiment and the limited energy resolution does not allow us to directly distinguish between these two cases by dispersions, as we have no access to q-space and cannot resolve the gap. The only criterion that we can use is the fact that phonons are not limited to magnetic materials, and are insensitive to the magnetic configuration of the system.

A direct comparison between magnetic Fe and non-magnetic Cu already hints on the magnetic origin of the excitation, since $\mathrm{d}^2I/\mathrm{d}U^2$ on Cu(111) (see Fig. 3.3) has no features at all below 50 meV, while the phonon dispersion in Cu is very similar to the one in Fe [34]. The excitation cross-section, calculated from numerically differentiated $I(U)$ (see Fig. 4.3), is $25\pm5\,\%$, which is also much higher than expected for phonon creation in iron at 4.2 K [35].

4.1.1 Checking magnetisation dependence (Fe(100), Fe/W tip)

If the observed excitation is a magnon, then it should follow the selection rules for magnons as explained in Sect. 2.2.2, i.e. for positive bias the probability of magnon creation should be zero for a fully spin-polarised majority current, since magnons

can only be created by minority electrons. Although it is not experimentally possible to get a 100 % spin polarisation, one should still register a change in the peak height if the majority/minority electron ratio changes. This change is inherent to the excitation of magnons, and should not be observed for phonons.

To be able to change the spin-polarisation of the tunnelling current we used a W tip coated with Fe. 10 monolayers (ML) of Fe were deposited on the tip and gently annealed (200 V, 5 mA), leading to formation of Fe clusters several tens of nm thick [36, 37, 38]. On planar W(100), these clusters were found to have large coercive fields around 35 mT [38], and an in-plane magnetisation [39], matching that of the sample. Prior to the measurement, the magnetic field in plane was ramped up to +45 mT, to orient the tip magnetisation along the whisker. The electrons coming from such a tip have a preferential spin direction (more than 60 % of the tunnelling electrons will be of minority character for the tip), and can be of majority or minority character with respect to the sample, depending on the sample magnetisation. If the tip and the sample are magnetised in the same direction, then the incoming electrons will be minority electrons for the sample, enhancing magnon creation. For the case of antiparallel magnetisations, most of the electrons are of majority character, and will not create magnons.

Spin-polarised $\mathrm{d}^2I/\mathrm{d}U^2$ curves on an Fe(100) whisker were recorded as function of polarity of an applied field of ± 7.5 mT. The field was applied along the easy axis of magnetisation, i.e. the [100] direction, parallel to the whisker axis. The coercivity of the Fe whisker was below 7.5 mT as measured *in situ* with the magneto-optic Kerr effect, ensuring full switching of the whisker in the applied field. At the same time the field is insufficient to switch the tip magnetisation. This allows to toggle between a parallel (or nearly parallel) and an antiparallel (or nearly antiparallel) orientation of tip and sample magnetisations.

The obtained spectra for Fe-Fe tunnelling are presented in Fig. 4.4. The structure of the features at E_F has changed strongly from a simple W tip - Fe sample case, showing in addition to a strong peak at positive bias, also a pronounced antisymmetric dip at negative bias. The dip is much more intense than in the non-magnetic-tip case, meaning that an additional magnon creation channel has appeared for electron tunnelling from the sample to the tip. An obvious explanation for this effect would be the presence of magnetic material on the tip, so that the minority electrons coming from the sample are able to scatter inelastically in the tip, creating magnons there.

As expected for a magnetic excitation, a noticeable difference is present in the spectra taken for different field directions. One also observes that the heights of the peak and the dip depend on the sign of the field, while the total peak-to-peak difference is not changing too much. To understand these observations, one can use the following model. The total tunnelling conductivity G is given by the sum of the partial conductivities, one for each spin channel. For a fixed bias, the amount of tunnelling electrons in a certain channel is proportional to the conductivity of this channel. The probability of magnon creation is then also proportional to this

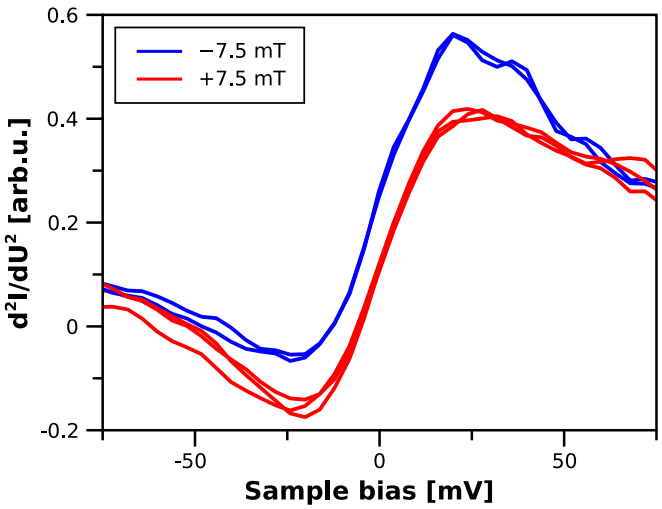

Figure 4.4: $\mathrm{d}^2I/\mathrm{d}U^2$ curves of Fe(100) taken with an Fe coated W tip in an applied field of $\pm 7.5\,\mathrm{mT}$ showing inelastic peaks $\approx 20\,\mathrm{mV}$ above and below E_F. The modulation amplitude was 10 mV. The height of the inelastic peaks vary with the sign of the field indicating a magnetic origin.

conductivity.

If the magnetisations of tip and sample are parallel (+7.5 mT), $G = G_{\uparrow\uparrow} + G_{\downarrow\downarrow}$, where $\uparrow$ denotes a majority state, and $\downarrow$ a minority state, i.e. the majority electrons of the tip tunnel into majority states of the sample and minority electrons of the tip tunnel into minority states of the sample. Magnons are created by majority electrons tunnelling out of the tip ($G_{\uparrow\uparrow}$), and minority electrons tunnelling into the sample ($G_{\downarrow\downarrow}$), meaning that magnon creation happens in both channels, with the total probability proportional to the full G. When the bias is reversed, the total probability stays proportional to G, as the magnons are still created in both channels. Then the magnon creation probability in both directions is proportional to G. Peaks of identical absolute height are expected in this case (a positive above and a negative below the Fermi energy).

If the magnetisations are antiparallel (-7.5 mT), G is given by $G_{\uparrow\downarrow} + G_{\downarrow\uparrow}$. In this case, majority electrons of the tip are minority electrons for the sample and vice versa, meaning that magnon creation will only happen in one channel, depending on the tunnelling direction. For positive bias, minority electrons, tunnelling out of the tip will create magnons neither in the tip nor in the sample. On the contrary, majority electrons tunnelling out of the tip can lead to magnon creation in the tip and coming as minority electrons to the sample can also create magnons there. Therefore, the height of the peak is proportional to $2G_{\uparrow\downarrow}$. Analogously, for negative bias, magnon creation only happens in the other channel, and the depth of the dip is proportional to $2G_{\downarrow\uparrow}$. In the likely case that the electronic structure of tip and sample are not identical, e.g. due to different crystallographic orientations, $G_{\uparrow\downarrow} \neq G_{\downarrow\uparrow}$, leading to different sizes of peak and dip.

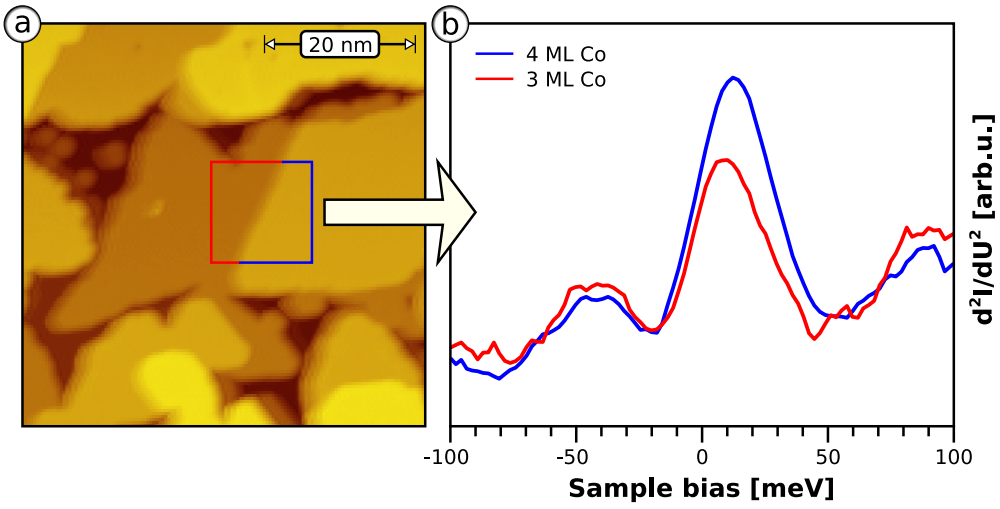

Figure 4.5: (a) Topographic image of 3 ML of Co deposited on Cu(111). Terraces of 3 and 4 ML are visible. (b) $\mathrm{d}^2I/\mathrm{d}U^2$ (5 meV modulation) averaged over the indicated region.

The sum of the peak and dip heights is equal to $2G$, independently on the magnetisation direction, and since before the measurement the tip was always stabilised at the same current and bias voltage, G did not change in the experiment. It follows that if the sample magnetisation is switched from a parallel to an antiparallel configuration, the sizes of peak and dip change in opposite directions, in full agreement with the observation.

Therefore, the observed features are in agreement with magnon excitation. For phonons the expected signal is independent on the magnetic field in contrast to the experimental observation, excluding phonons as a reason for the inelastic peaks.

4.1.2 Checking material dependence (Co/Cu(111), W tip)

To see in more details if the $\mathrm{d}^2I/\mathrm{d}U^2$ depends on the magnetic properties of the sample, we have performed similar measurements on thin magnetic films of Co on Cu(111). As the thickness of the film can be varied, and with it the amount of the magnetic material, we can check if the intensity of the inelastic features in the spectra changes with film thickness. For phonons one would expect that the excitation cross-section is similar for Co and Cu, and there should be little or no variation in peak height. On the contrary, magnons will be excited exclusively in Co, and taking into account the spin scattering length of several nanometres for low energy electrons in ferromagnets [40], one can expect a linear dependency on film thickness for low coverages.

A 3 monolayer (ML) thick Co film was deposited on Cu(111) at room temperature. In this magnetic film, terraces of several local film thicknesses could be observed simultaneously (Fig. 4.5b). The $\mathrm{d}^2I/\mathrm{d}U^2$ curves were recorded on 3 and 4 ML terraces within one measurement, ensuring identical tip conditions. Both

terraces display a $\mathrm{d}^2I/\mathrm{d}U^2$ signal quite similar to the one on Fe, with a peak—counter-peak structure and a similar slight increase of the signal after the peak. We can indeed see a difference in the peak height on terraces of different thickness.

Calculation of the cross-section from numerically differentiated $I(U)$, as described above (cf. Fig. 4.3), gives a cross-section of $\sigma_3 = 10 \pm 1\,\%$ for 3 ML and $\sigma_4 = 16 \pm 1\,\%$ for 4 ML, an almost linear dependence on thickness. If this excitation would be a phonon, such a dependence could only be explained by an exclusive excitation of phonons in the Co film, that has never been reported and does not fit to established solid state models. On the other hand, it fits perfectly to magnon excitation, that should only exist in the magnetic Co film. Assuming that a fixed percentage of electrons σ_1 scatter in every layer, the electron mean free path due to magnon creation can be calculated with $\lambda = -a_{\mathrm{Co}}/\ln(1-\sigma_1)$, where $a_{\mathrm{Co}} = 1.9\,\text{Å}$ is the interlayer distance in Co/Cu(111) following [41]. The average σ_1, obtained from σ_3 and σ_4, is equal to $3.8 \pm 0.2\,\%$/ML. This number includes all the electrons, i.e. including majority electrons that do not undergo spin-flip scattering. Thus, to get a more meaningful scattering probability, we take into account the ratio of minority and majority states at E_{F} of 63 % (see next section), to obtain the number of scattering minority electrons of $6.0 \pm 0.3\,\%$ per monolayer giving $\lambda = 3.0 \pm 0.2\,\mathrm{nm}$. This result is in agreement with theoretical calculations of the mean free path of $\approx 3\,\mathrm{nm}$ [42].

4.2 Asymmetry

It is time now to address the difference between peaks for forward and backward tunnelling in our $\mathrm{d}^2I/\mathrm{d}U^2$ spectra. As mentioned earlier, magnons are created with minority electrons tunnelling in and majority electrons tunnelling out of the ferromagnet. The original $\mathrm{d}^2I/\mathrm{d}U^2$ on Fe(100) has a peak-dip structure, corresponding to magnon creation for both tunnelling directions. The curves, however, clearly show that the probability of the excitation depends on bias polarity, i.e. more magnons are created by minority than by majority electrons. A straightforward explanation for this effect is given by different contributions from the two spin channels. From the Tersoff-Hamman model, in a system with one magnetic and one non-magnetic electrode, the minority current is proportional to $\rho_\tau \rho_\sigma^\downarrow$, and the majority current to $\rho_\tau \rho_\sigma^\uparrow$. Thus, in case the sample DOS ρ_σ is polarised, so is the current. If there are more minority states in the sample at $E_{\mathrm{F}} + \mathrm{e}U$, most of the tunnelling electrons are of minority character, independently on the tunnelling direction. This makes magnon creation for forward tunnelling more probable than for backward tunnelling and the peak at positive bias becomes more intense than for negative bias.

If we define the asymmetry of the observed peak/dip structure as

$$\mathcal{A} = \frac{I_\rightarrow - I_\leftarrow}{I_\rightarrow + I_\leftarrow}, \tag{4.2}$$

where $I_{\rightarrow/\leftarrow}$ are the peak/dip intensities, proportional to the DOS of the sample, then $\mathcal{A} = \frac{\rho_\downarrow - \rho_\uparrow}{\rho_{\text{total}}} = -P$, with P the polarisation of sample DOS as defined in Eq. 2.12.

To check this result, the DOS in the STM geometry was calculated within the Tersoff-Hamann approach at a tip height of about 4 Å above the surface layer reflecting the value estimated from point contact experiments [43]. The calculated DOS is strongly polarised — the minority density of states at E_{F} (0.03 states/eV) is more than three times larger than the majority DOS at the same energy (0.009 states/eV), meaning that in accordance with the experimental spectra, magnon creation should happen more often in the minority channel, i.e. for tip-to-sample tunnelling.

For a precise comparison, the $\mathrm{d}^2I/\mathrm{d}U^2$ was fitted with two Gaussians, one with a positive amplitude and one with negative, on top of a linear background, reflecting a smooth DOS (see Fig. 4.6). Calculating the asymmetry parameter as in Eq. 4.2 gives $\mathcal{A} = 61 \pm 4\,\%$. The polarisation of the DOS is -54 %[1], in a very good agreement with the experimental value.

As a cross-check, the same procedure of comparing the polarisation of the DOS with the asymmetry of the $\mathrm{d}^2I/\mathrm{d}U^2$ was applied to two more magnetic systems: 3 ML Co/Cu(111) and 2 ML Co/Cu(100). Thin magnetic films of Co were deposited on clean Cu(111) and Cu(100) substrates by molecular beam epitaxy with a rate of ≈ 0.7 ML/min at room temperature. Both systems show a nearly layer-by-layer growth at small thicknesses [44, 45], giving large enough flat terraces to reach the necessary signal quality. The experimental $\mathrm{d}^2I/\mathrm{d}U^2$ curves were averaged over at least 200 measurements done at different points of the same terrace. The $\mathrm{d}^2I/\mathrm{d}U^2$ curves of these systems also show an asymmetry (see Fig. 4.7), although a smaller one with respect to Fe(100) ($28 \pm 5\,\%$ for 3 ML Co/Cu(111) and $13 \pm 8\,\%$ for 2 ML Co/Cu(100)), fully supported by the calculated DOS polarisations ($P_{\text{Co/Cu(111)}} = -26\,\%$, $P_{\text{Co/Cu(100)}} = -14\,\%$).

A compilation of these results is shown on the Fig. 4.8. As one can see, the dots for all the investigated magnetic systems lie on the 1-to-1 correspondence line, justifying the proposed model. The probability of magnon creation, i.e. the transfer of spin moment between the current and the magnetisation, or in other words the spin torque in the classical description, is defined by the polarisation of the DOS. This dependence was often assumed in the works on the spin torque effect [46, 47] without experimental verification. Our data now experimentally prove this assumption.

[1]The polarisation was calculated at E_{F}, since the DOS varies very little in the energy region probed in the experiment

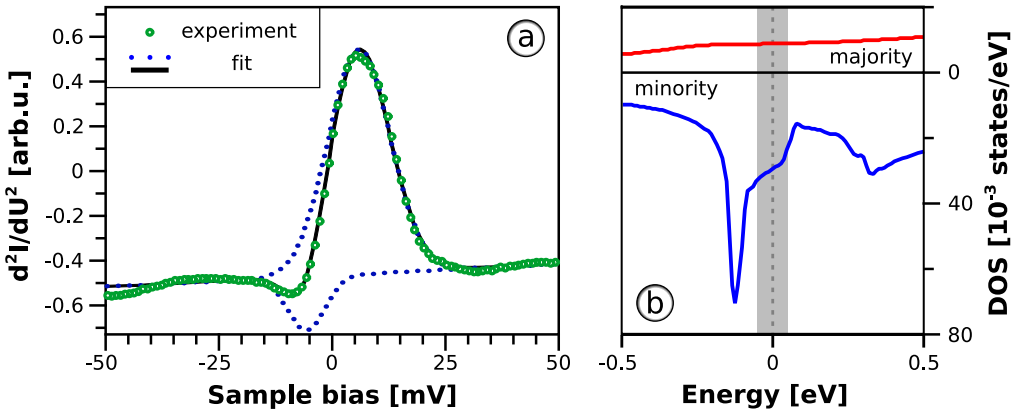

Figure 4.6: (a) Asymmetric Fe $\mathrm{d}^2I/\mathrm{d}U^2$ spectrum with a superimposed Gaussian fit of the data. (b) Spin-dependent DOS per atom of Fe(100) in STM geometry, 4 Å away from the surface. The grey area corresponds to the bias range of graph (a).

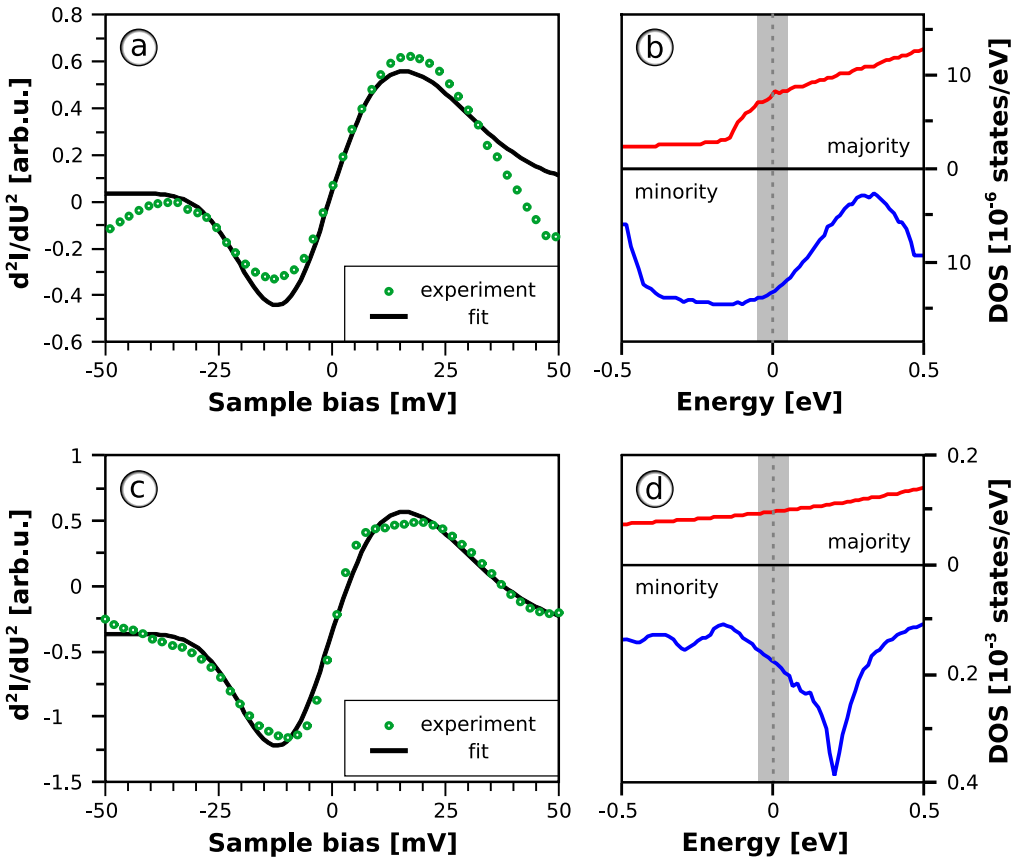

Figure 4.7: (a) and (c) inelastic $\mathrm{d}^2I/\mathrm{d}U^2$ spectra taken on 3 ML Co/Cu(111) and 2 ML Co/Cu(100) respectively with superimposed Gaussian fit. (b) and (d) DOS per atom of the two respective systems in STM geometry. The grey areas correspond to the bias range where the inelastic spectra were taken.

4.3 How magnons are created

Although magnons in Fe(100) can have energies up to 600 meV, our $\mathrm{d}^2I/\mathrm{d}U^2$ curves mostly show magnon creation below 50 meV. No peaks at energies higher than 100 meV have been found, meaning that it is highly improbable for an electron to create a high-energy magnon in our experiment. The reason for this must lie in the actual mechanism of the spin-flip scattering for tunnelling electrons.

A number of interactions could be proposed as the basis for the scattering mechanism of the hot electron with the electrons of the sample, including the standard Coulomb potential between two charges, the screened Coulomb potential[2], which is more appropriate in metals, or the Ruderman-Kittel-Kasuya-Yoshida (RKKY)-like exchange potential, describing the exchange interaction between delocalised electrons [25, 49]. For a given potential $V(\vec{r})$ one can calculate the interaction cross-section at different wavevectors using the Born approximation,

$$\frac{\mathrm{d}\sigma}{\mathrm{d}\Omega}(\vec{q}) \propto |\mathcal{V}(\vec{q})|^2, \tag{4.3}$$

where $\mathcal{V}(\vec{q})$ is a Fourier transform of $V(\vec{r})$. To relate the cross-section of the excitation to the experimentally measured $\mathrm{d}^2I/\mathrm{d}U^2$, one has to convert the former to the energy space. The first derivative of the tunnelling current at bias U is proportional to the amount of states the electrons with energy $E_\mathrm{F} + \mathrm{e}U$ can tunnel to. This includes the states with energy $E_\mathrm{F} + \mathrm{e}U$ (elastic tunnelling) and for each excitation of energy $E_\mathrm{x} < \mathrm{e}U$ the states with the energy $E_\mathrm{F} + \mathrm{e}U - E_\mathrm{x}$ (inelastic tunnelling). Assuming a constant DOS within the studied energy range, the second derivative

[2]The screening length in Fe was taken equal to 1.4 Å, following [48]

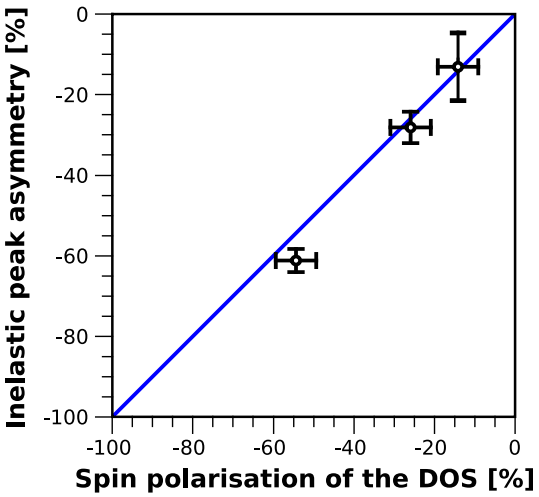

Figure 4.8: The relationship between peak asymmetry and DOS polarisation. A error of 5 % was assumed for the theoretical calculations. The uncertainty in the asymmetry value comes from the fitting procedure.

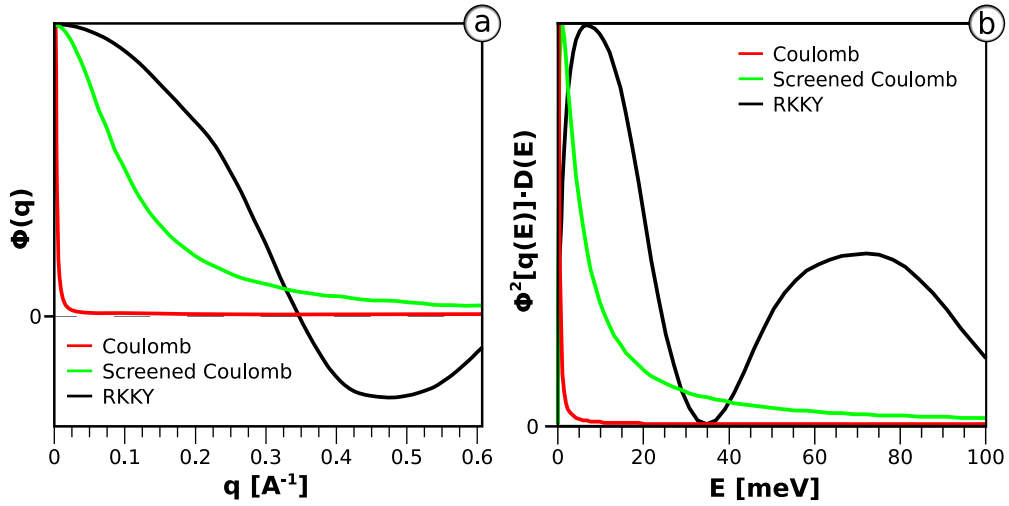

Figure 4.9: (a) q-space form of the Coulomb, screened Coulomb and the RKKY-like exchange potentials. (b) $\sigma(E)$ for the three potentials from (a).

at bias U is then proportional to the number of excited states with energy E_{x}, i.e. proportional to the magnon DOS $D(E)$. $\mathrm{d}^2I/\mathrm{d}U^2$ must also depend on the cross-section, i.e. on the probability of creating magnons with a given energy. Taking all this into account, we find

$$\mathrm{d}^2I/\mathrm{d}U^2 \propto |\mathcal{V}(q(E))|^2 \cdot D(E) \tag{4.4}$$

The three proposed interaction potentials and the resulting $\sigma(E)$ are shown on Fig. 4.9. The RKKY-like exchange potential was calculated from a classical

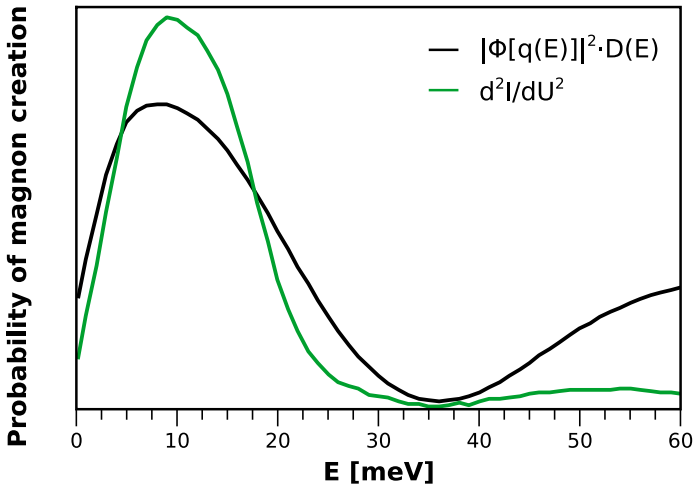

Figure 4.10: The green experimental curve has a close similarity to the black one, calculated from the RKKY-like exchange potential. The scale is arbitrary. The two curves have been normalised by the area under the first peak.

Heisenberg Hamiltonian and the magnetic force theorem [43]. Both the Coulomb and the screened Coulomb potentials show the maximum of the cross-section at less than 5 meV, and can therefore be rejected. The RKKY-like potential, however, gives a close resemblance to the experimental curve (Fig. 4.9), including a peak around 10 meV, a minimum at 35 meV, and a subsequent increase. The maximum is caused by the oscillatory nature of the RKKY-like exchange interaction, resulting in a peak in the reciprocal space that matches well with the observed peak in the $\mathrm{d}^2I/\mathrm{d}U^2$. The large discrepancy between experiment and theory observed at higher energies might be due to a saturation of the cross-section. The total electron-magnon scattering cross-section in Fe is 24 % of all electrons for forward tunnelling. Since the magnons are only created in the minority channel, which is, as we know, three times more pronounced than the majority channel, this means that more than 30 % of minority electrons scatter creating magnons. The large value breaks the assumptions of the Born approximation and leads to a higher predicted value when compared to experiment.

We can now conclude from the good agreement between experiment and theory, that the mechanism of spin transfer between a hot electron and the electrons of the sample is non-local. The exchange interaction behind it is not a point interaction, reflecting the itinerant character of electrons in iron. This leads, among other things, to a large final cross-section for magnon creation and a preferential magnon energy range between 5 and 20 meV.

4.4 Critique of the elastic spin torque

An STM with a magnetic tip and a magnetic sample is an example of a magnetic tunnel junction (MTJ). Such junctions have been widely studied with respect to their current-voltage characteristics. Two interesting effects observed in MTJs are the tunnelling magnetoresistance [17, 50] and the current-induced magnetisation switching [51]. The first effect describes the change of the MTJ resistance when the magnetisation direction of one of the electrodes is changed, and the second shows that the magnetisation of the electrode not only changes in external magnetic field, but may also be switched by a spin-polarised current through the junction. This switching can be described by a torque of the current acting on the magnetisation. As the change in the magnetisation is related to a spin transfer between the current and the magnetisation, this torque is commonly named *spin transfer torque* (STT). The standard phenomenological description of STT has been created by Slonczewski. This theory explains the STT by elastic electron scattering in the magnetic electrode. However, as we have seen in this chapter, the inelastic contributions to the STT cannot simply be discarded, as more than one quarter of all electrons scatter inelastically. This contribution may even be a dominant term at biases above 5 mV.

All of the results of the elastic model can be reproduced in the inelastic approach. First, the creation of magnons leads to changes in the magnetisation.

One magnon changes the z component of the total spin of the magnetic system $S^z = \sum S_i^z$ by one, and makes the local magnetisation precess around the equilibrium position, until the magnon is annihilated and the magnetisation is restored. Depending on the wavevector q of the magnon, also the total spin $S = \sum S_i$ may be changed in the process. In this case, the precession of the magnetisation is accompanied by a reduction of the average (effective) magnetisation. If more electrons tunnel, the magnetisation of the sample is lowered further, and can finally be totally reversed in case the currents are high enough. The elastic torque in a junction acts similarly, but affects all spins of the sample in parallel, leading to a collinear precession of spins with a constant magnitude of the magnetisation during switching. In other words, only the magnon with $q = 0$ is excited. We have shown, however, that most of the excited magnons have non-zero energies and therefore a non-zero wavevector. The inelastic torque created by a magnon with $q \neq 0$ describes a non-collinear state, such as the effective magnetisation of the sample, as considered in elastic STT, not only precesses around the equilibrium position, but is also reduced in magnitude due to a change in the total spin of the sample. The reduction of the effective magnetisation in magnetic nanostructures was observed in recent spin torque experiments [46], and thus the inelastic model has a better agreement with experiment than the elastic one. Second, the torque is an interfacial effect, as demonstrated by the mean free path of 3 nm, in agreement with the results of Slonczewski [5]. Third, as we have seen, the probability of magnon creation, proportional to the STT, is defined by the polarisation of the tunnelling current. This dependence was assumed in the elastic model, but never proved.

It has been shown that the elastic STT model fails to qualitatively predict the size of the spin torque and the oscillation frequencies, obtained experimentally [52, 53]. Our experiments show that the macrospin model is inherently flawed in the assumption of a constant effective magnetisation and only elastic scattering. Our last result, that the interaction between the tunnelling electrons and the magnetisation is non-local, seems to further discredit that model. We see, that the interaction between an electric current and a magnetic material cannot be treated macroscopically. A non-local exchange interaction requires a new model based on a true quantum-mechanical description of delocalised electrons for a correct description of the STT.

Chapter 5

Magnons in thin films

As we have discovered, our method to investigate magnons has a limitation in what concerns the range of available q-vectors, due to the very nature of the electron-electron interaction that leads to magnon creation. At a first glance, this kills the hope for measuring a full magnon dispersion. Indeed, it is so, at least for the bulk. What one needs is a system with a 'side' approach to the dispersion. Such a system is provided by a magnetic thin film.

A film is a two-dimensional system, i.e. magnons can only propagate freely in the plane of the film. In the out-of-plane direction (z axis) the propagation is forbidden, and the system behaves like a quantum well, forming discrete energy levels. Due to the discrete nature of the system itself, i.e. N discrete atomic layers, the number of magnon modes is finite and equal to N. Note that every mode still has a continuous dispersion in the xy-plane, such that the magnon spectrum consists of N branches (see Fig. 5.1a,b).

The modes for a given film can be calculated using the Heisenberg ferromagnet model (see A.3.4), provided the exchange constant J is known. The calculation shows that at the $\bar{\Gamma}$ point, i.e. $q_{\parallel} = 0$, the discrete modes closely follow the original bulk dispersion, if one assigns a virtual wave vector to each mode in the form

$$q_n = \frac{n}{N} Q_{\max}, n = 0, \ldots, N-1 \tag{5.1}$$

where $Q_{\max}$ is the Brillouin zone boundary in bulk for the z axis direction. Thus, the energy of the highest mode never reaches the top of the band as it can be observed in bulk (see Fig. 5.1).

An inelastic spectrum, taken on a thin magnetic film on a non-magnetic substrate, should show a multitude of peaks, corresponding to the discrete modes. As we know from the bulk, only the low-$q_{\parallel}$ part of the dispersion will contribute to the peak, and thus the position of the peaks should roughly correspond to the beginning of the bands at $\bar{\Gamma}$. As dictated by the inelastic tunnelling model, each peak at positive bias should also have a corresponding dip at negative bias. In the following this property will be used to identify magnon peaks in the spectra.

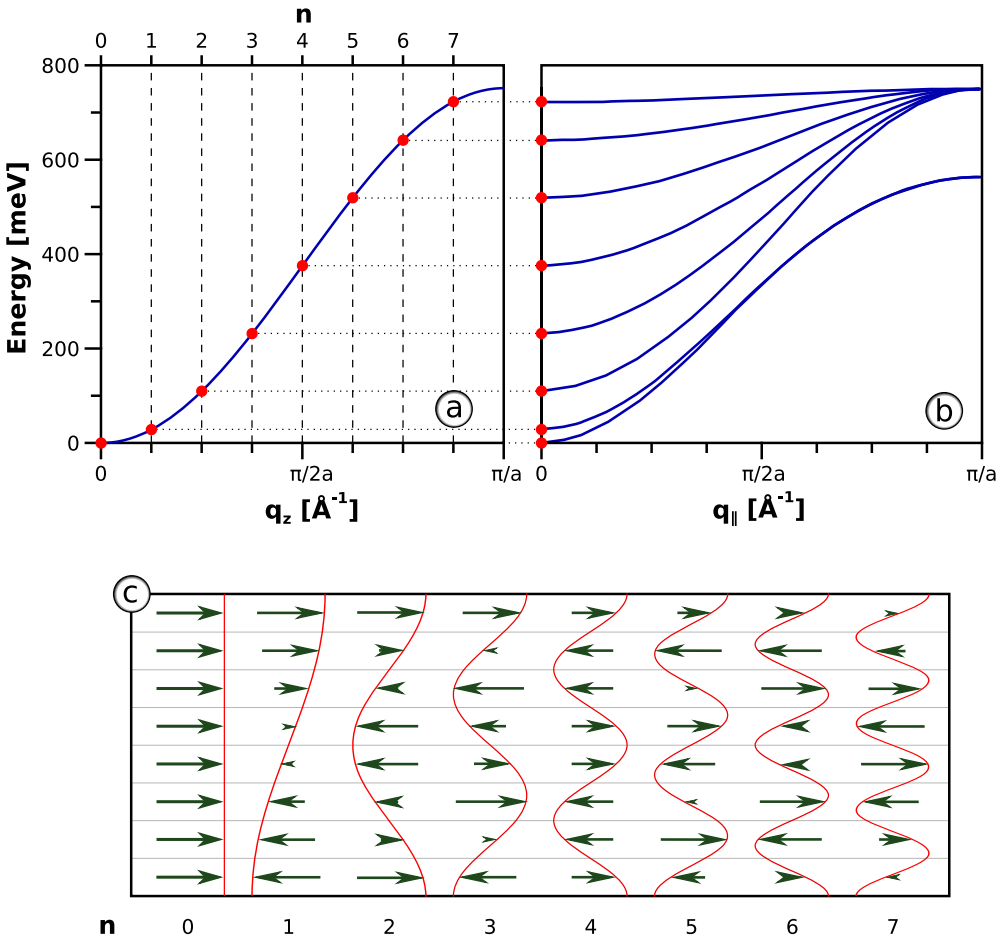

Figure 5.1: (a) Discrete modes in an 8 ML thick film of Co/Cu(100) superimposed on the dispersion for bulk fcc Co, as given by the Heisenberg model. (b) The eight magnon branches corresponding to the modes in (a), calculated using the model detailed in A.3.4. (c) The geometry of the standing modes. The arrows do not represent the magnetisation of the layer, but the amplitude of the oscillations. The mode index n gives the number of nodes in the standing magnon.

5.1 Thin film systems

Two systems were chosen for investigation of magnons in thin films, Co/Cu(100) and Ni/Cu(100). The first system has been thoroughly investigated in the past and can be considered a model system for thin film magnetism. The second system has a more complicated behaviour with several magnon bands.

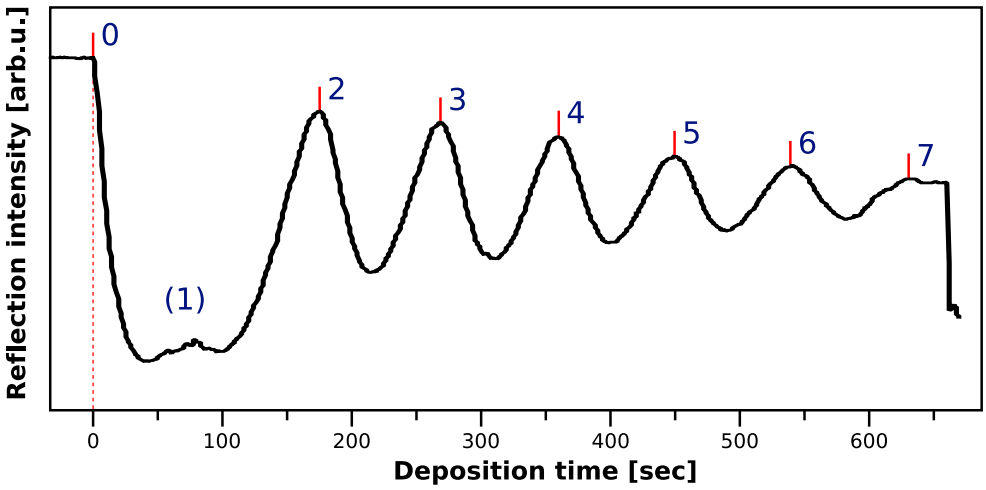

Figure 5.2: MEED oscillations for 7 ML Co/Cu(100). The oscillations stem from a periodic transition between a flat film at monolayer completion and a rough film at half-a-monolayer coverages.

5.1.1 Co/Cu(100)

Growth

At room temperature Co shows a good layer-by-layer growth, at least up to 15 monolayers (ML) [45], except for the first two layers, that grow together. The crystallographic structure of the film follows the fcc Cu substrate structure, with a slight tetragonal distortion due to a lattice mismatch of 1.7 %.

In full agreement with the above, the time-dependence of the reflected electron beam intensity observed during Co deposition as explained in Chapter 3, begins with a double dip (1) for the first two layers and has regular oscillations from there on (see Fig. 5.2). The decreasing intensity of the peaks indicates that the layer-by-layer growth is not perfect, and the new layer starts to grow before the layers underneath are complete.

Indeed, as seen in the STM topography pictures on Fig. 5.3a, as-deposited Co films are rough, exposing areas of three different local thicknesses. This roughness is observed for all the films investigated in this experiment. The size of the largest rectangular terrace reaches only $10\times10\,\mathrm{nm}^2$. Such an irregular surface might affect the magnon dispersion, and therefore a smoother film is required.

A direct approach to smoothing is to increase the temperature of the film, allowing atom diffusion on the surface. The small islands will in this case dissolve, when their atoms diffuse to fill in the holes in the bottom layer [54], leading to a much flatter surface (see Fig. 5.3b). However, annealing allows not only the diffusion of Co on the surface, but also the diffusion of Cu from the interface to the surface through the microscopic pinholes [55]. Luckily, this process is only present in films thinner than 6 ML. Therefore, Co films below 6 ML were not annealed

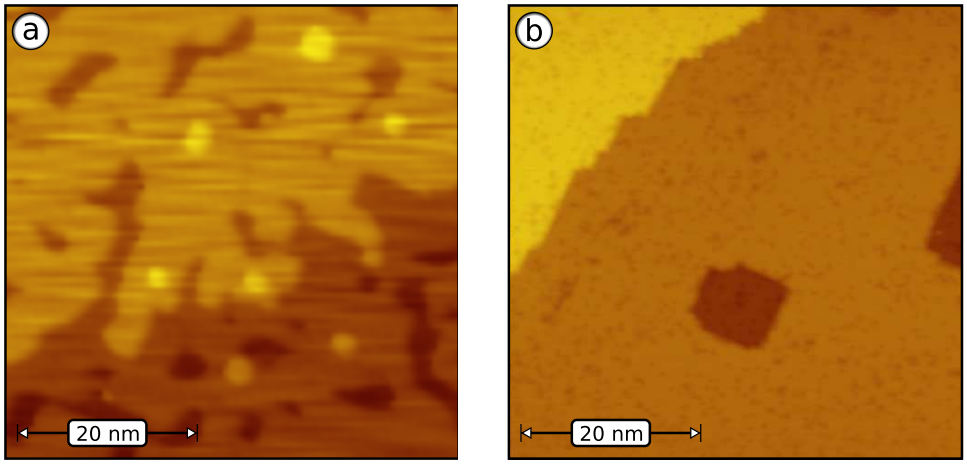

Figure 5.3: (a) As-deposited 7 ML Co/Cu(100) (b) Co/Cu(100) after annealing to 370 K

after deposition, but investigated *as is*, and films from 6 ML up were annealed up to 370 K for one minute.

Magnetism

Co films on Cu(100) are ferromagnetic with an in-plane easy axis, as indicated e.g. by ferromagnetic resonance [56]. There have been numerous investigations of the spin-wave behaviour in bulk fcc Co[1] and in Co/Cu(100) with neutron scattering, Brillouin light scattering and other techniques, as well as theoretical calculations. The experiments indicate a uniform single-band parabolic dispersion for small q-vectors with the spin-wave stiffness D between 370 and 450 meV Å^2 [57, 58, 59, 60, 10, 61]. Theoretical calculations show a much wider range of D values depending on the employed calculation method — from 250 to 800 meV Å^2 [62, 63, 64, 65, 66, 57]. According to the same calculations, the top of the magnon band lies between 600 and 800 meV.

5.1.2 Ni/Cu(100)

The second system chosen for investigation, Ni/Cu(100), is more sophisticated from the magnetic point of view. Although growth of Ni has been investigated in detail, its magnetic properties and especially magnetisation dynamics are considerably more complicated than those of Co and are not totally clear to this day.

[1]Since Co cannot be stabilised as an fcc bulk crystal, small amounts of Fe (8 %) were added to it.

Growth

The mismatch between Ni and Cu lattices is below 3 %, so Ni grows pseudomorphically on Cu(100) up to thicknesses of 11 ML [67]. The deposition of Ni was performed identically to that of Co, with simultaneous growth control by MEED. As in the case of Co, the growth is not perfect, so the films have been annealed to 370 K after deposition. All of the deposited films were thick enough to suppress pinhole diffusion, so no additional precautions have been taken for thinner films.

Magnetism

Ni films on Cu(100) exhibit different magnetic properties depending on thickness and temperature. At room temperature the magnetisation of the film changes from in-plane to out-of-plane around 7 ML and back to in-plane at 15 ML. At 4 K, however, the film appears to be in-plane magnetised for the whole thickness range [68].

The magnon dispersion in bulk Ni has two intersecting bands, as predicted by theoretical calculations [69] and confirmed by inelastic neutron scattering [70]. The 'acoustic' branch, starting from zero with a spin-wave stiffness of 400 meV Å^2 reaches the top of the band at around 350 meV. The 'optical' branch exists in a much smaller energy range and crosses the 'acoustic' one at around 120 meV. The interaction between the two bands decreases magnon lifetimes and leads to a smearing of inelastic neutron scattering peaks. The magnons from the 'acoustic' branch are further strongly damped at energies above 200 meV due to dissipation of spin waves into the Stoner excitations, which for Ni lie between 300 and 400 meV.

5.2 Magnons in Co/Cu(100)

The measurements were done on 3.5, 6, 7 and 9 ML thick Co films. Experimental curves, presented on Fig. 5.4, show several general tendencies. First, the assumption that the number of peaks scales with film thickness seems to be confirmed. The 9 ML film shows approximately 3 times more peaks than the 3.5 ML one, but 6 and 7 ML Co/Cu(100) have a very similar signal shape.

Second, the peak intensity decreases with peak number, while the width of the peak increases. This means that higher energy magnons are more short-lived, as expected due to the proximity of the Stoner continuum. One also notices that the width of the peaks changes only slightly with film thickness, when comparing peaks in the same energy region. E.g. the peaks around 300 mV change from being 50 mV wide in 9 ML to 65 mV in 3.5 ML. The peaks are less pronounced in thinner films, that can be attributed to the mean free path of minority electrons being about 3 nm, as discussed in the previous chapter.

The third general feature is only visible on the negative side of the spectra, and is more pronounced for thinner films. There seems to be a broad dip around

−400 meV. For thin films (6 and 3.5 ML) this dip nearly completely hides the less intense structure expected for magnon excitations. Comparing the spectra with the band structure calculations for bulk fcc Co [71], one can attribute this feature to a majority band edge. The position of the dip changes slightly with film thickness, as expected due to the changes in the electronic structure of thin films as compared to bulk. In general, since the spectra on thin films were taken for a larger energy range than the spectra discussed in the previous chapter, there is more influence from the electronic DOS. When we concentrated on low energy magnons, the DOS was almost constant in the investigated energy region. Now that the region of interest is extended by more than an order of magnitude, this is no longer the case and care should be taken not to confuse DOS-related structure with inelastic features.

To obtain the dispersion and make sure that the peaks correspond to magnon excitations, we have to assign wave vector values to them. However, we cannot exclude the possibility that some of the peaks observed in the spectra are related to features in the density of states, to other inelastic excitations (for example due to defects or adatoms on the tip) or to a noticeable noise level. In order to eliminate the last possibility, several hundred inelastic spectra taken on an area of several square nanometres were averaged together to produce the final curves. This method also minimises the contribution from impurities on the surface (although care was taken to measure on areas clean of adsorbates, some effects might have made their way into the spectra). The DOS of bulk fcc Co has in addition to the already mentioned majority band edge also two minority edges at ≈ 200 and ≈ 800 meV. The first band edge does not seem to lead to any prominent features in the spectra, but cannot, of course, be totally excluded. The second band edge is already outside the investigated region, although one can attribute to it the general increase in the $\mathrm{d}^2I/\mathrm{d}U^2$ at the right edge of the spectra.

One more precaution that can be taken during peak analysis is to use the inherent peak symmetry of the inelastic excitation, i.e. the fact that peaks and dips should always come in pairs, as the basis for selecting and numbering peaks. This method is not 100 % foolproof, since inelastic excitations in the tip might also be symmetric, but it is a good starting point. Unfortunately, the strong elastic feature in the negative part of the spectra totally hides the dips in the thinner films. Thus, this method can only be applied to thick films. As a second step towards peak identification, one can compare spectra obtained before and after a tip change. The features that change significantly with tip changes must have been introduced by the tip. However, we have found that the tip condition may also affect the intensity of what appears to be peaks related to magnon creation. This introduces an additional difficulty in the interpretation of the experimental data.

The last criterion for peak selection is the expected energy difference between the individual modes. Although the exact form of the dispersion in thin films is unknown, we can safely assume that the spin-wave stiffness will not change too drastically, and so the distance between the peaks for our films should increase in thinner films and be at least 20 meV in the middle of the Brillouin zone. It should

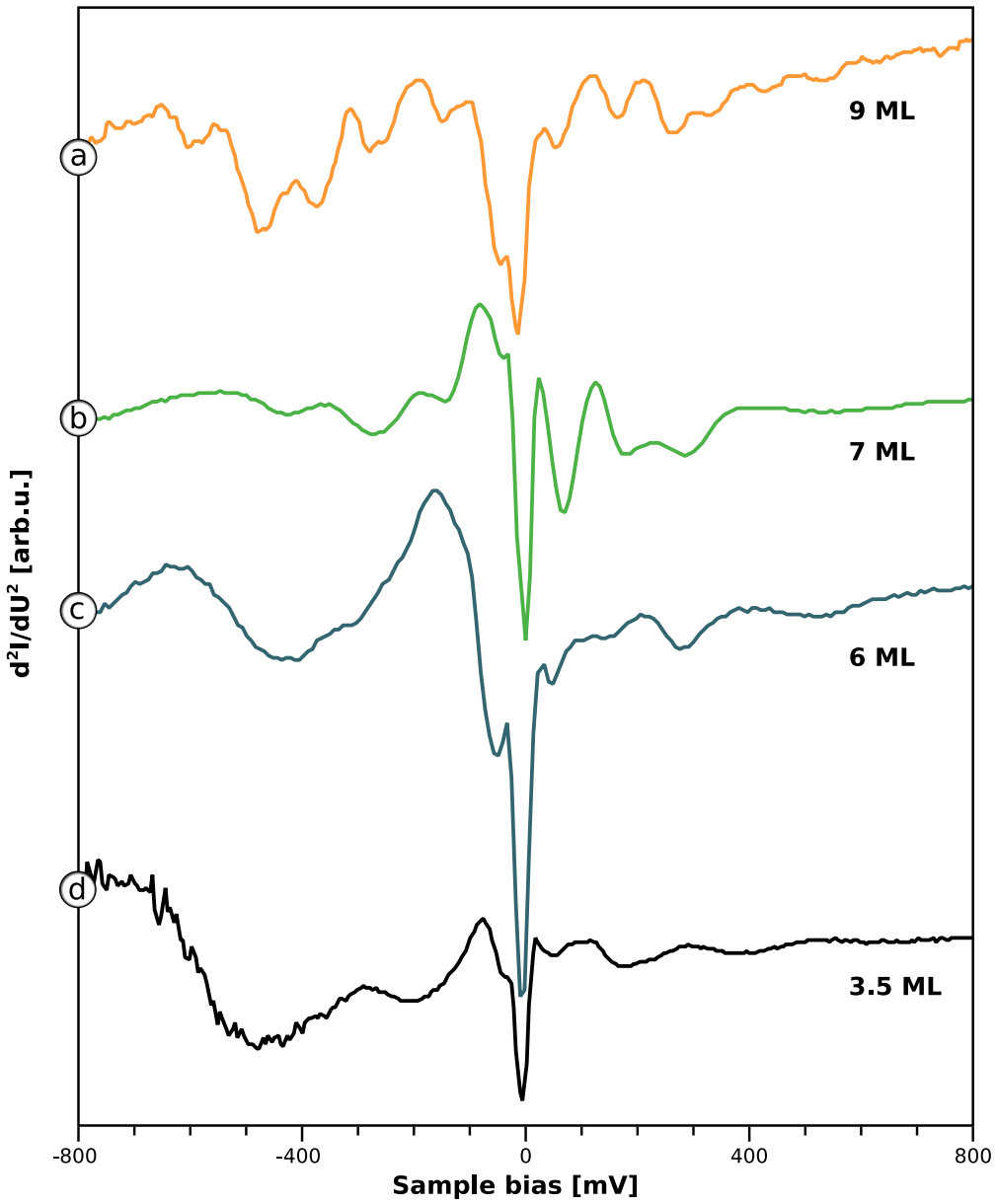

Figure 5.4: $\mathrm{d}^2I/\mathrm{d}U^2$ measured on Co films of indicated thickness on Cu(100).

also be increasing in the first half of the zone. Thus, if two peaks are very close to one another, they cannot both belong to the set of peaks expected for the given film thickness. This situation does not occur often, and its presence indicates a coexistence of modes belonging to different local film thicknesses, as will be shown later.

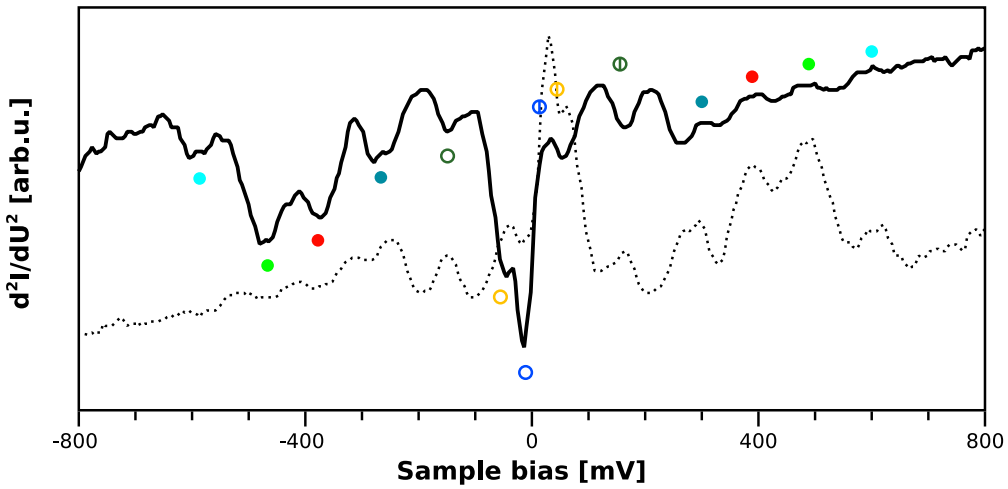

Figure 5.5: Matching peaks for 9 ML of Co/Cu(100). The solid curve is the experimental spectrum. The dotted curve is the same spectrum, mirrored on both axes so that the dips from the negative side become peaks at the positive side. Filled circles indicate well-matching peak-dip pairs. Unfilled circles indicate doubtful matching in the region around E_F.

5.2.1 9 ML

An example of the peak matching process is shown on Fig. 5.5, where the spectrum corresponding to 9 ML is displayed together with a superimposed mirrored version of the same curve. The peaks that appear at the same position in both curves, should correspond to an inelastic excitation. The higher energies match very well down to 200 meV. The peak, that appears at this position on the positive side, does not have a negative counterpart. The dip on the other side is nearly 50 meV away from the expected position. Accidentally, +200 meV is also the position for the minority band edge, so it can be that the feature of the DOS obscures the magnon peak. If this is true, then the real position of the peak can be deduced from the position of the dip at the negative side, where no DOS features exist. Closer to the Fermi edge the curve gets more irregular and the peaks appear more tightly spaced. This is expected, since the dispersion is only slowly rising in this region. One has also to consider the result from the previous chapter that the magnon peak is shifted with respect to its expected position due to a dependence of the interaction cross-section on the magnon wavevector. This shift is of the order of 10 meV, so it will most strongly affect the regions with tightly packed peaks, i.e. the small energies. Thus, we can expect that the first peak, corresponding to a 'collinear rotation' of spins (see Fig. 5.1b), expected at zero energy, will almost completely overlap with the second mode peak, that is expected for 9 ML at 20 meV assuming bulk dispersion. The peak for the next mode at 80 meV will also overlap with the second peak, producing a complicated structure. And since the resolution of the curves is about 5 meV, it becomes difficult to separate the peaks. One has also to consider, that due to variations of the DOS, peak and dip intensities might

not match, and their shape could be different. Thus, overlapping peaks produce different shapes on the positive and on the negative sides. For the analysis, we have assumed that there are three peaks in the region from −100 to +100 meV, and took the best matching peak-dip pairs for the dispersion. After the pairs have been identified, we assign a q value to each pair according to Eq. 5.1 in the order of increasing energies. The resulting $E(q_n)$ points form the dispersion on Fig. 5.6 (orange set). The obtained dispersion corresponds well to a theoretically calculated dispersion of magnons in bulk fcc Co, being, however, slightly lower in energy. The good agreement proves that the peaks correspond, indeed, to excitation of magnons and that magnons in 9 ML of Co/Cu(100) behave similarly to magnons in bulk.

5.2.2 6 and 7 ML

7 ML of Co on Cu(100) spectra have less peaks than 9 ML, making them easier to analyse. Although the structure at the Fermi edge still does not match perfectly, other peaks have clearly symmetric dips below zero. We have found that the area around E_F is also the most affected by tip changes, so the unmatchable structure can be partially explained by impurities on the tip. One notices, however, that no peaks could be reliably extracted from the curves above 500 meV. This is most likely related to the increasing peak width, meaning that the strong damping makes these magnon modes decay very quickly and denies observation. The obtained dispersion also matches the bulk dispersion in shape, but is generally lower than the dispersion for 9 ML (see the green set on Fig. 5.6).

In the 6 ML thick film, the band edge at −400 meV is very prominent and makes matching of the peaks tedious if not impossible. Thus, the dispersion was mainly extracted from the positive side of the curve. The magnon modes above 500 meV also appear strongly damped. The dispersion on Fig. 5.6 (blue set) appears lower than both the dispersions for 9 and 7 ML.

5.2.3 3.5 ML

This film was not annealed after deposition to avoid Cu diffusion, so it exhibits terraces of different thicknesses. To only obtain two different thicknesses, the deposition was stopped at half a monolayer. Otherwise, one would expect at least three different local thicknesses contributing to the dispersion, that would further complicate the analysis. We can expect that if two areas of different thicknesses are connected, magnons will be excited with both sets of energies. And indeed, the spectrum on Fig. 5.4d shows more than four peaks on the positive side. The negative side is again strongly obscured by DOS features. If we suppose that peaks on the positive side correspond to magnon modes in both 3 and 4 ML, we can construct two dispersions. This is also supported by the fact that spectra taken on different positions on the sample sometimes show that the intensity of some of the peaks increases, decreasing for the others. The double peak close to 100 meV

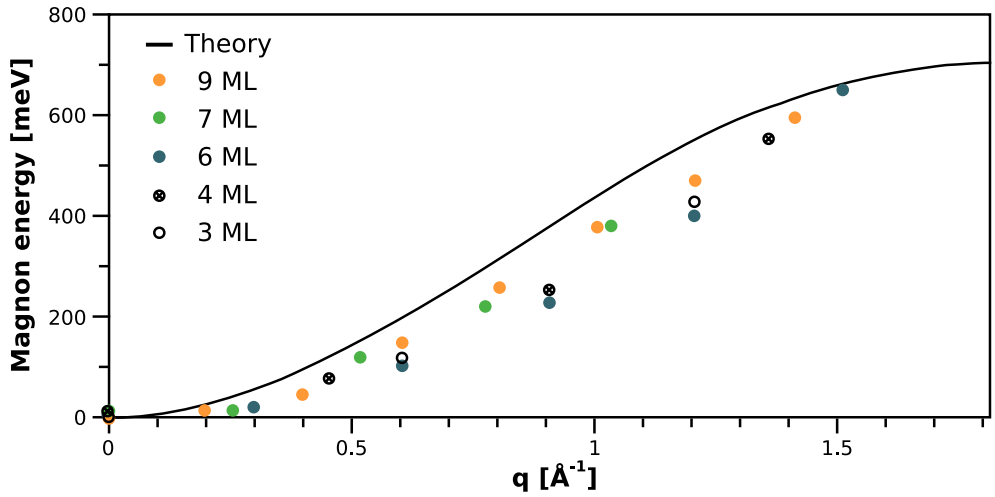

Figure 5.6: The dispersion obtained from the experimental curves by matching peaks and dips for Co/Cu(100). The solid line is the dispersion obtained by Pajda *et al.* for bulk fcc Co [25].

appears, however, practically unchanged in all scans, that can be due to similar energies of the second mode for both thicknesses. The two resulting dispersions (black sets on Fig 5.6) appear slightly higher than the dispersion for 6 ML, but are still below 9 and 7.

5.2.4 Magnon dispersion in Co/Cu(100)

The magnon dispersion extracted from all the spectra for different thicknesses is collected in Fig. 5.6 and compared to the bulk calculation by Pajda *et al.* [25]. Overall, the experiment shows that magnon dispersion in thin films closely follows the bulk dispersion down to 3 ML. The absolute values are, however, slightly lower than for bulk. To compare our results with neutron scattering investigations, we calculated the spin-wave stiffness by fitting the lower part of the dispersion with a parabola. The resulting value of $360 \pm 20\,\mathrm{meV\,Å^2}$ is very close to the ones obtained by other methods. We can conclude that Co films on Cu(100) have bulk-like magnon dispersion, and the magnetism of the films is well-describable by a localised spins Heisenberg model. Note, however, that the dispersion of a thinner film lies systematically below that of the thicker. Although the reduction is small, it indicates the softening of magnons by finite size effects. This can be due to an exchange beyond the nearest neighbour, that has not been taken into account in our model, or to a change of the electronic structure in very thin films.

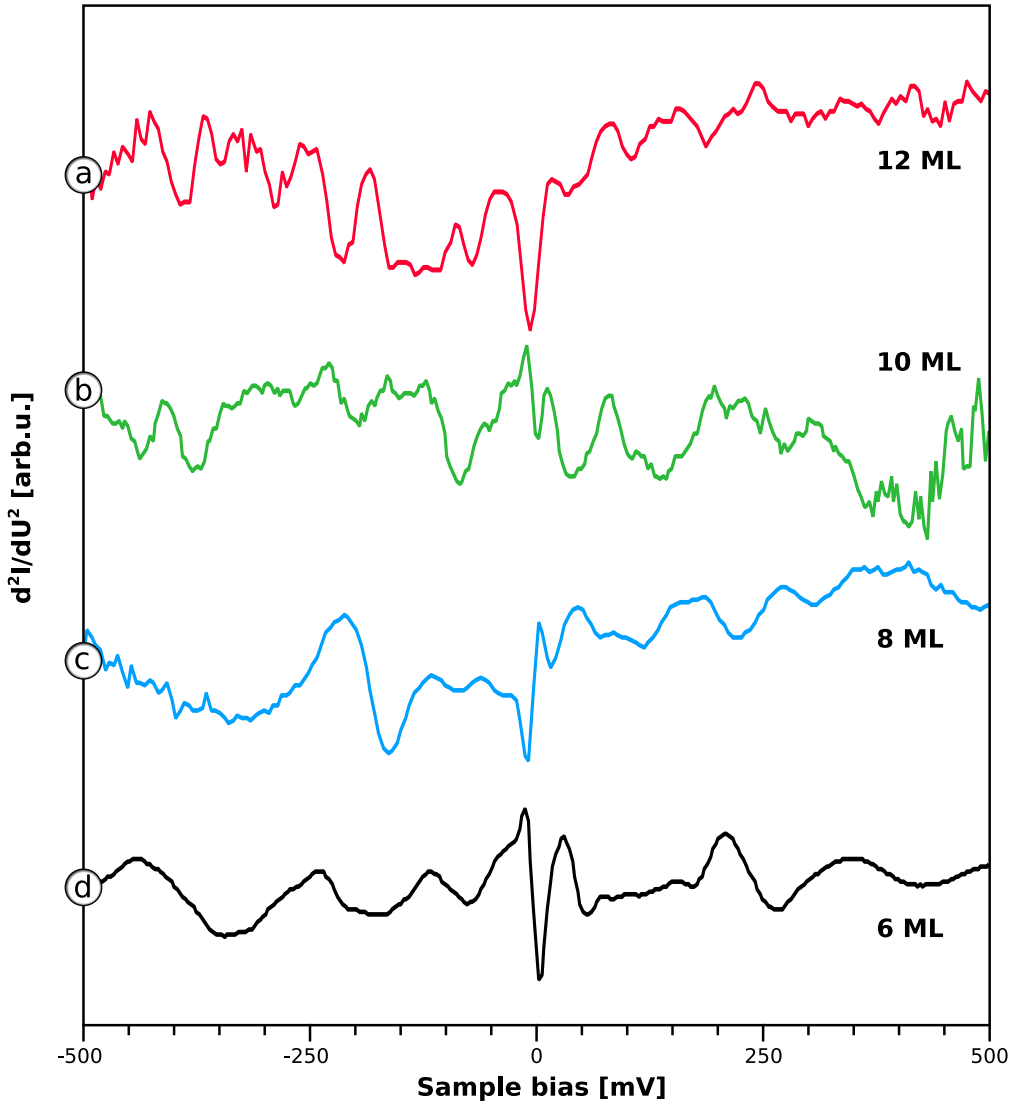

Figure 5.7: $\mathrm{d}^2I/\mathrm{d}U^2$ measured on Ni films of indicated thickness on Cu(100).

5.3 Magnons in Ni/Cu(100)

The measurements, performed on Ni films 6, 8, 10 and 12 ML thick, show a behaviour close to the one observed for Co. The number of peaks scales with film thickness and the peak width increases with energy. Features in the DOS of Ni are less pronounced than for Co in the investigated energy region, and matching the peaks with dips is easier. However, the spectra for 10 and 12 ML are more noisy than for thinner films, so only wide enough peaks were taken for analysis.

The expected strong damping of spin waves in the region around 120 meV, where the two magnon bands cross, is also manifested in our spectra. Notably, although the model predicts a peak in this region for 6 and 8 ML, the spectra

exhibit a plateau in its stead. For 10 ML the plateau appears to be shifted to higher energies, and then disappears for 12 ML.

A major problem, however, occurs when one tries to assign wavevectors to observed peaks. Although one does not see such a significant broadening for high-energy peaks as observed in Co films, the number of peaks is lower than the number of layers. This can be partially attributed to the 'missing' peaks, but even taking those into account does not increase the mode number enough. It seems that either the band is totally flat at high energies for a very significant part of the Brillouin zone, or that the Heisenberg model and with it the numbering criteria fail.

To check for the reason of this discrepancy and to understand more about the structure of the inelastic spectra, we have compared our spectra to the results of theoretical calculationsdone with a non-adiabatic approach to the magnetic excitations, which, in contrast to the Heisenberg picture, allows to see the interaction of the spin waves with the Stoner continuum, and is known to reproduce the lifetimes observed in experiments [72].

The calculated magnon DOS's in the (100) direction in bulk Ni, taken at the appropriate $q_\perp$, were compared to the positive side of the spectra as shown on Fig. 5.8. We see that the calculations reproduce the experimental results quite well, in what concerns peak positions and widths. The theoretical spectra had to be slightly scaled down to lower energies to obtain a better match. This is predictable, since the theoretical method is known to give higher energies than the experiment due to the limitations of the local density approximation. Note, that the peak for the first mode is removed from all the spectra, as it should be overlapping with the second peak, due to the maximum of the interaction cross-section at $q_\parallel \neq 0$, that is not taken into account in the calculations. One notices that the agreement between theory and experiment becomes worse for thinner films. This is also expected, because the theoretical calculations correspond to modes in bulk fcc Ni, and we know that the magnon dispersion can be different for thin films.

The calculations show that the small number of the peaks, observed in the spectra, is mostly related to a flat top of the band, such that the last two to three modes are indistinguishable within the experimental resolution. The calculations also indicate that some of the double peak structures are related to lower modes having two DOS maxima, one for the 'acoustic' and one for the 'optical' band. Now that we know the correspondence between peak and wavevector, the dispersion can be derived. The results, presented in Fig. 5.9, show that Ni thickness has a much more pronounced influence on the dispersion than seen for Co. The top of the band seems to be lower by about 100 meV in 6 ML of Ni as compared to 10 ML. Spin-wave stiffness, calculated via a parabolic fit to the 12 and 10 ML dispersion up to q =0.6 Å^{-1}, gives a value of 720 ± 20 meV Å^2. Strangely, this value is quite far from the results obtained by neutron scattering (400 ± 20 meV Å^2). Comparison to an earlier theoretical calculation of magnon dispersion in bulk fcc Ni by Pajda *et al.* [25] also shows that our energies are systematically higher than expected. The large discrepancy may mean one of the two possibilities. The first explanation is

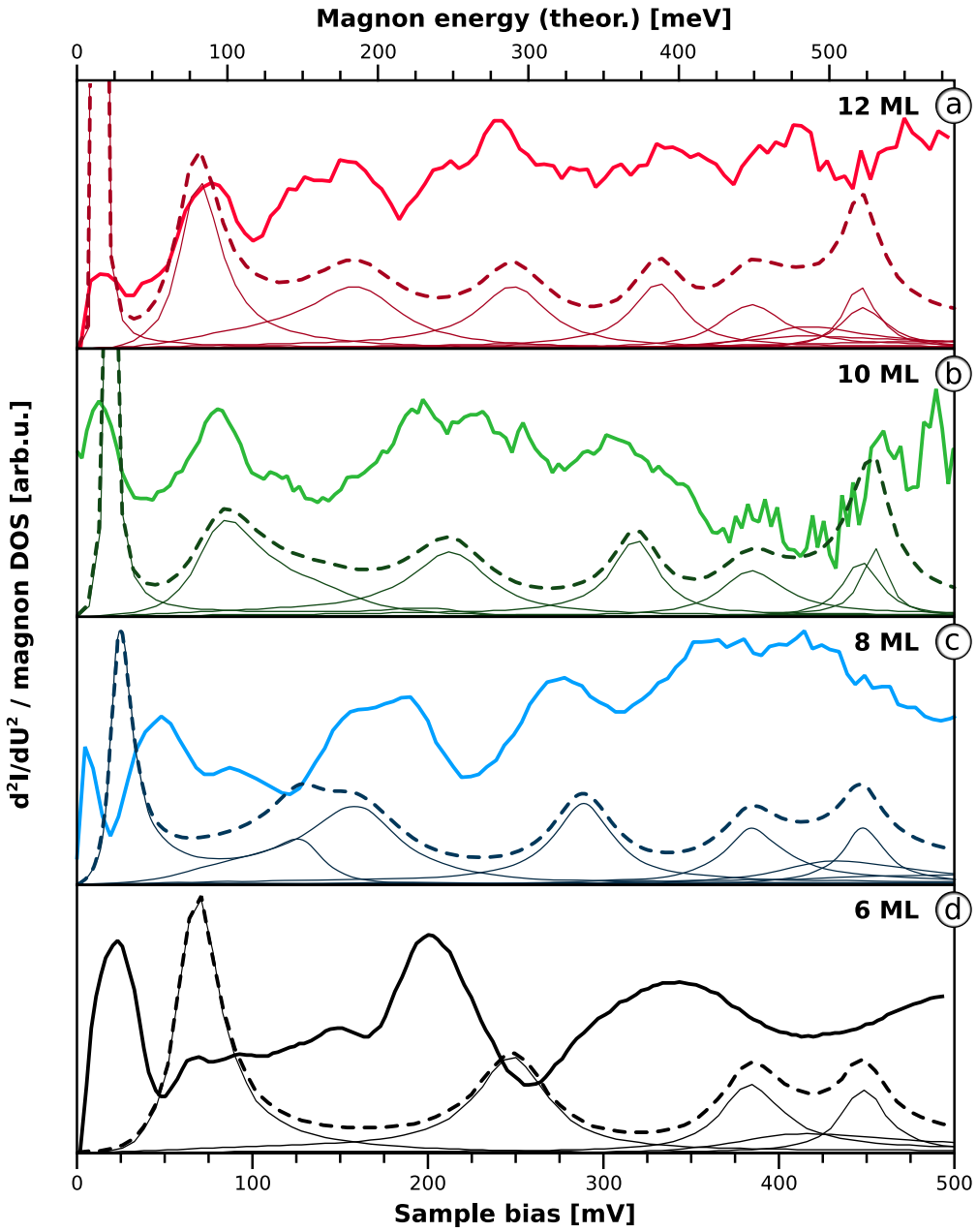

Figure 5.8: Comparison between experimental curves (solid) and the calculated magnon DOS (dashed) for Ni/Cu(100). The thin lines are the individual theoretically calculated magnon modes.

that our matching procedure for Ni is not acceptable and some of the peaks were missed during the evaluation leading to a general shift to lower q values and to a faster rising mode energy. As a second explanation it might be possible that our results indicate a significant difference of the electronic structure between bulk fcc Ni and thin films of Ni/Cu(100) in the investigated film thickness region. A hint

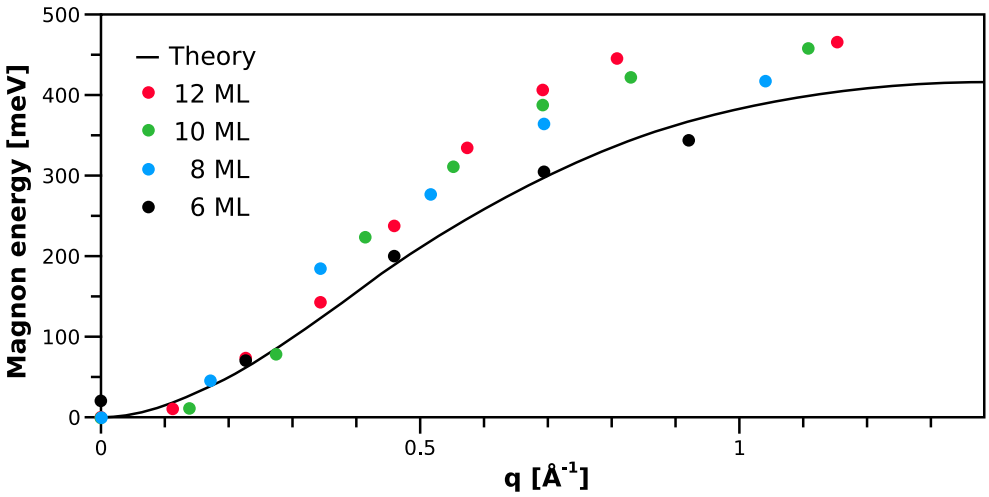

Figure 5.9: The dispersion obtained from the experimental curves by using the theoretical predictions of P. Buczek *et al.* The solid line is the dispersion obtained by Pajda *et al.* for bulk fcc Ni [25].

on that is provided by the double magnetisation reorientation transition observed in Ni at higher temperatures at about 7 and 15 ML, that exactly covers the region for with we observe elevated magnon energies (note that for 6 ML the obtained magnon dispersion corresponds well to the bulk). It could be that although the transition is not directly observed at 4 K, the underlying mechanism still works and manifests itself by changes in magnon dispersion. One way to check it would be to measure the dispersion in thicker films and to see if it returns to the bulk curve after a certain thickness.

In general, our research shows that ISTS can be used to investigate magnon dispersion in thin films and obtain the information from the whole Brillouin zone, inaccessible by standard methods. One needs, however, a good theoretical model that helps distinguishing magnon-related spectral features from background signals and electron density of states.

Chapter 6

Magnetic excitations of single atoms and clusters

Inelastic scanning tunnelling spectroscopy as a method to study magnetic excitations opens the possibility to investigate previously inaccessible systems with sizes in the low nanometre range that were not accessible before. It allows us to work with the smallest existing magnetic system — a single magnetic atom. In addition STM provides means for precise construction of larger systems by manipulating individual atoms [73]. As a result we could investigate inelastic excitations in individual magnetic atoms and clusters of up to three atoms in size.

The experiments were done with Fe and Co atoms deposited on a Pt(111) substrate. The deposition was done at 4.3 K to prevent thermal diffusion of the atoms. To achieve this, the evaporator was mounted directly in front of the cryostat and deposition took place when the sample was in the microscope. Short deposition times of ≈ 3 s ensured a low coverage of ≈ 0.006 ML (mean distance between atoms of the order of 3.5 nm, cf. Fig. 6.1a) and negligible temperature variation during deposition.

Atomic manipulation was performed by positioning the tip over an atom, approaching the tip towards the surface and displacing the tip in the approached position. With a certain probability, depending on the tip condition, tip-sample distance and positioning accuracy, the atom followed the moving tip on the surface and remained in the new position after tip retraction [74]. If two atoms were brought in a close proximity to one another (of the order of 2 Å) they would attract to each other and form a dimer [75]. The later can be distinguished from a single atom by a two times larger apparent height and a slight elongation (Fig. 6.1c). These features are even more pronounced for a trimer, formed by adding one more atom to a prepared dimer. Note, that after forming the cluster, it was found to be practically impossible to move it without risking crashing the tip into the surface.

The inelastic tunnelling spectra were measured directly with the tip above the atom or cluster and also, for comparison, on the substrate far away from any visible objects (see Fig. 6.2). For this experiment, low modulation voltages of the order

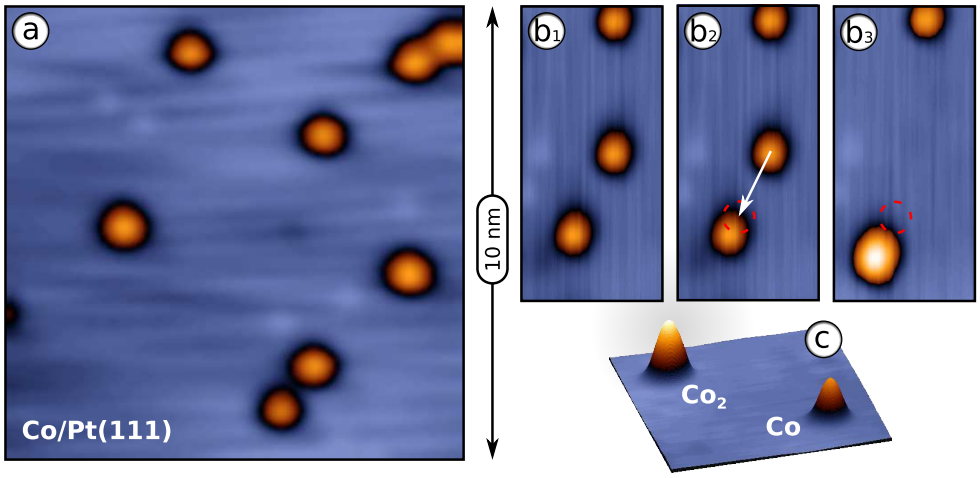

Figure 6.1: (a) Co atoms deposited on Pt(111). Bright blue dots on the surface are the adsorbed hydrogen atoms. (b) Forming a dimer by manipulating Co atoms. The resulting dimer on (b_3) is shifted from the expected position, showing that both atoms moved during manipulation. (c) 3D view of Co atom and dimer. The dimer appears much higher than the atom (220 pm vs. 160 pm).

of 2 mV had to be used to achieve a decent energy resolution, and to compensate for the low intensity of inelastic features, tunnelling currents were higher than for thin film or bulk systems and in the 100 nA range. Since high currents also lead to moving of atoms (dimer and trimers are stable) reasonable caution was exercised. Note that the Pt(111) surface has two different kinds of three-fold hollow adsorption sites: an *hcp* site, when the atom is placed just above the atom of the first sub-surface layer and an *fcc* site, when the nearest atom directly underneath the adsorbate is three layers deep. One can expect that the properties of atoms adsorbed on two different sites will not be the same. However, if one site is more energetically stable than the other, the high currents can lead to all the investigated atoms moving to the more stable adsorption site.

6.1 Inelastic excitations of single magnetic atoms

A single inelastic excitation is visible in the $\mathrm{d}^2I/\mathrm{d}U^2$ spectrum recorded on an Fe atom (Fig 6.2a). The spectrum recorded simultaneously on Pt only displays a minute signal (b), as expected for a sample with smooth DOS around E_F [76] in case no inelastic excitations exist in the investigated region. The genuine excitation spectrum (c) was obtained by subtracting the Pt background signal from the Fe spectrum (a). To evaluate the energy of the excitation, the spectrum was fitted with two antisymmetric Gaussians, giving peak positions at ±5.2 meV. The same process repeated for Co atoms on Pt gives very similar results with an excitation energy of 9.2 meV (Fig. 6.3).

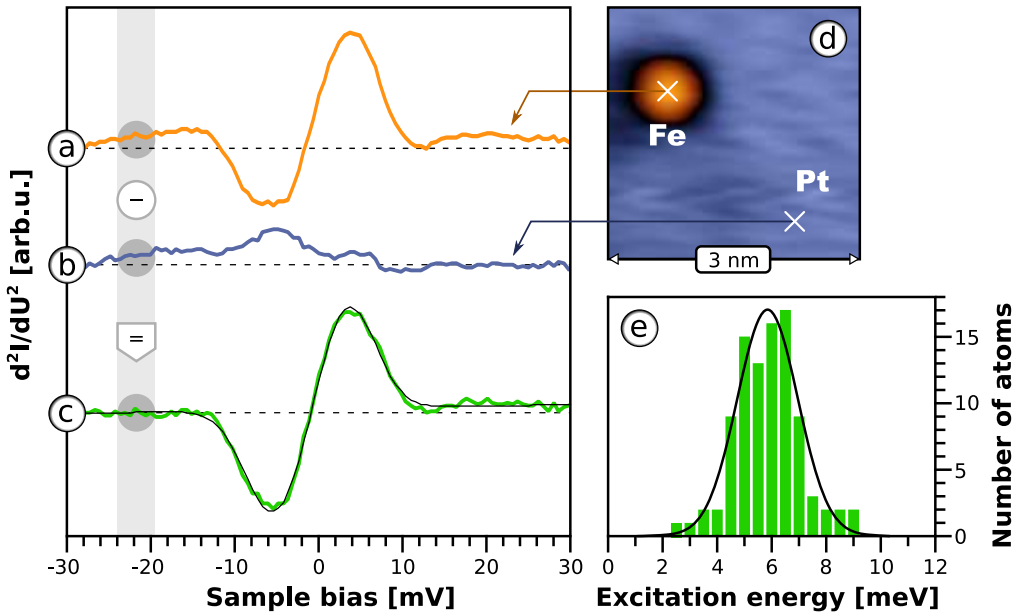

Figure 6.2: The genuine Fe excitation spectrum (c) was obtained by subtracting the substrate signal (b) from the spectrum taken on the Fe atom (a) like shown in (d). Evaluation of peak positions on 94 different curves gives an energy distribution (e). The distribution was fitted with a Gaussian [black curve in (e)] to obtain the excitation energy of 5.83 meV.

Measurements performed on different atoms or several times on the same atom tend to show slightly different results from spectrum to spectrum. To investigate the reason for this effect and to increase the precision of the experiment, the excitation energies measured on several dozens of atoms were collected in a histogram. The histogram bin size of 0.5 meV was chosen significantly smaller than the energy resolution of the measurement of ≈ 3 meV. Both Fe and Co histograms seem to show a single normal distribution of energies (Fig. 6.2e and Fig. 6.3e). The width of the distribution is comparable to the energy resolution of the experiment. The centre of the distribution is found by fitting the histogram with a Gaussian yielding an energy of 5.83 ± 0.08 meV for Fe and 10.25 ± 0.15 meV for Co atoms.

The fact, that the energies are normally distributed, indicates that this scattering is most likely caused by statistical reasons, such as fitting errors, limited energy resolution and lock-in integration delays. The single peak of the histogram suggests that either the excitation energy does not depend on the adsorption site within the energy resolution of the experiment, or atoms only in one configuration are found.

6.1.1 The origin of the excitation

As in the case of the other systems, there is no direct way for us to know the nature of the observed excitations. The energy transferred to the atom can go

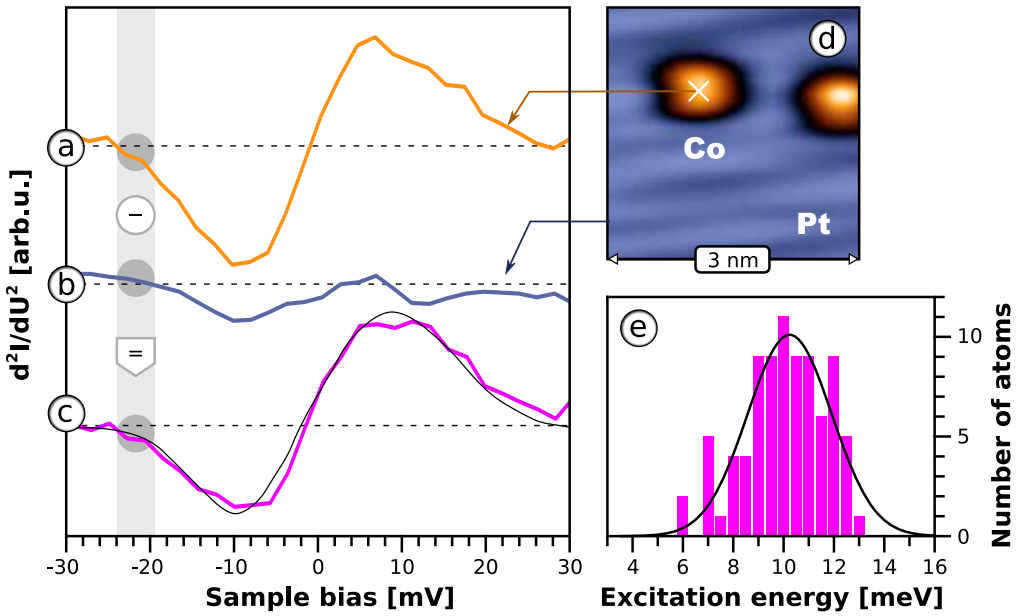

Figure 6.3: The genuine Co excitation spectrum (c) was obtained by subtracting the substrate signal (b) from the spectrum taken on the Co atom (a) like shown in (d). Evaluation of peak positions on 84 different curves gives an energy distribution (e). The distribution was fitted with a Gaussian [black curve in (e)] to obtain the excitation energy of 10.2 meV.

into mechanical vibrations (phonons) or charge density waves (plasmons). It can also mean a spin transfer between the electron and the atom. We have to exclude the other possibilities before proceeding. Note that although one could directly check for a magnetic origin of the excitation by applying a high magnetic field that would shift the states of the atom, leading to an increase of the spin-flip excitation energy [12], the field required to produce a noticeable shift is of the order of 10 T and is outside our experimental capabilities.

To rule out phonon excitations, we have determined the vibration energy of Fe and Co atoms on Pt(111) by first-principles calculations [77]. The atom was moved from its ground state position in all directions and the potential landscape was obtained by calculating the atom energy for each position. The potential has 3-fold rotational symmetry, but to simplify the calculation it is enough to estimate the lowest possible phonon energy. It is given by the energy difference of the ground state and the first excited state in the parabolic potential with a curvature equal to the lowest curvature of the real potential. For an Fe atom a cut of the landscape along the direction of lowest curvature, i.e. the line connecting two neighboring sites of the surface, is shown in Fig. 6.4. A parabolic fit to the potential of the form $E_a = Ax^2$ gives a stiffness A of 4.7 eV/Å^2. Using the solution for the harmonic oscillator with a potential $V(x) = \frac{1}{2}m\omega^2x^2$, the lowest excitation energy is

$$E_{\mathrm{ph}} = \hbar\omega = \hbar\sqrt{2A/m_{\mathrm{Fe}}}, \tag{6.1}$$

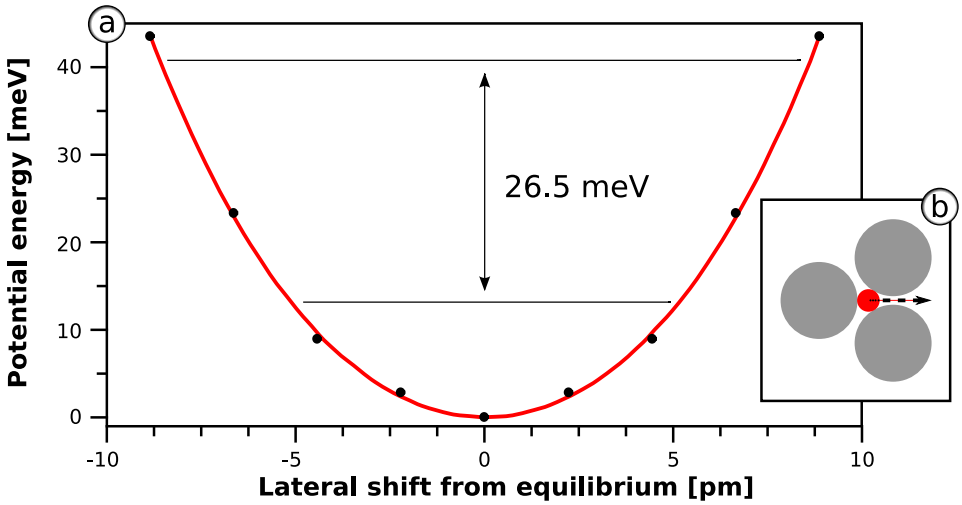

Figure 6.4: (a) A parabolic fit (red line) to the potential energy of an Fe atom (black dots) when shifted from its ground state along the (122) axis (b). The values for negative shifts are mirrored from the positive side.

giving 27 meV, i.e. six times higher than the experimental energy. The analogous calculation for Co yields a phonon energy of 24 meV, which is more than two times higher than the observed excitation energy.

As a cross-check, we assumed a sinusoidal potential $V(x) = \epsilon/2 \times (1 - \cos(2\pi x/d))$, with ϵ equal to the experimental value for the diffusion barrier of Pt atoms on Pt(111) of 260 meV [78] and d the distance between the neighbouring hollow sites. The stiffness in this case evaluates to 1.0 eV/Å^2, giving two times smaller phonon energies, still much higher than the observed energy for the Fe atom. The new value is somewhat close to the excitation energy of the Co atom, but first, this approach uses some severe approximations, and second, there is no reason for the phonons to be excitable in Co atoms but not in Fe atoms. This being said, we can exclude phonons as a reason for the observed peak. We can also exclude the excitation of plasmons, since, as detailed in Chapter 4, plasmon energies in metals are of the order of several eV.

The features in the $\mathrm{d}^2I/\mathrm{d}U^2$ could also be a signature of a Kondo resonance, when there is an exchange of electrons of opposite spins between the localised atom and the conduction electrons. However, no Kondo effect was observed for Fe and Co on Pt(111) in the results of other groups [28, 79]. The absence of a Kondo resonance for Fe and Co atoms and clusters on Pt(111) can be explained by their considerable perpendicular magnetic anisotropy [28, 80] which lifts the spin degeneracy of the atom. As a consequence, a first-order Kondo process, that would change the spin of the atom by 1, would require energy and is suppressed[1]. Only higher order Kondo processes coupling the states with $S_z = \pm S$ are possible, resulting in very small Kondo temperatures [81, 82]. Additionally, experimental

[1]The only exception would be an atom with $S = 1/2$, that is not the case for both Fe and Co.

evidence on magnetic impurities like Fe embedded in a Pt host or placed onto a Pt surface shows that large magnetic moments are induced at the neighboring Pt atoms, i.e. the net magnetic moment per magnetic impurity is enhanced [28, 80, 83]. This induced polarisation is opposite to the Kondo effect, which instead would decrease the magnetic moment by screening.

Thus, the only process left is a spin-flip of the tunnelling electron, accompanied by a change of the spin of the atom.

6.1.2 The relationship between the excitation energy and the magnetic anisotropy

It is known that the easy magnetisation axis of Fe and Co atoms on Pt(111) is out-of-plane [28, 80], and so the ground state of the atom is $|\pm S\rangle$ (i.e. $S_z = \pm S$), where S is the spin of the atom and the z axis is along the surface normal. Transfer of angular momentum between the atom and the electron leads to spin rotation and brings the atom to a state $|\pm(S-1)\rangle$. Due to a non-zero uniaxial magnetic anisotropy, this process costs energy. In the quantum limit, i.e. for an isolated atom with spin S, the uniaxial anisotropy energy term can be written as DS_z^2 ($D < 0$ for an out-of-plane easy axis). This description is linked to the classical uniaxial MAE $K\cos^2\theta$ (with $K < 0$) by the correspondence principle $\cos\theta = S_z/S$, where θ is the angle of the magnetisation with respect to the surface normal. The energy of the excitation is given by $E_\mathrm{x} = D(S-1)^2 - DS^2 = -D(2S-1)$. The classical MAE is then $K = DS^2 = -E_\mathrm{x}S^2/(2S-1)$.

Thus, in order to obtain the MAE from the experimentally measured energy, one has to know the spin of the relevant atom. Here we use the value calculated by A. Ernst [77]. The calculations considered a system consisting of a 80-atoms Pt block[2], embedded in a semi-infinite Pt(111) crystal, with a single metallic atom on top. The system was relaxed by varying the distance between the atom and the Pt block till the energy minimum was reached. The influence of the STM tip was simulated by a cluster of four atoms 4 Å above the magnetic adatom. Total spin magnetic moments for Fe and Co atoms were calculated scalar-relativistically from first principles. It was found that a strong hybridisation between the atom and Pt electron states causes noticeable delocalisation of impurity $3d$ electrons. As a result, a magnetic moment is induced on previously non-magnetic Pt atoms. To properly account for that, the spin value was calculated from the total magnetic moment of the atom together with its surrounding Pt. Magnetic moments of Co of $2.2\,\mu_\mathrm{B}$ and of Fe of $3.4\,\mu_\mathrm{B}$, when taking a Landé factor of $g \approx 2$ for electrons and assuming a half-integer spin, transform to $S_\mathrm{Co} = 1$ and $S_\mathrm{Fe} = 3/2$.

Here, treating the impurity as a quantum spin ($S = n/2$ with an integer n) is an idealisation, strictly valid only in the limit of vanishing hybridisation with the substrate. For the actual systems we investigate, the hybridisation is significant,

[2] 5 layers with 16 atoms per layer

Table 6.1: Relationship between measured excitation energies and MAE.

Cluster	spin	spin transition	excitation energy [meV]	MAE [meV/atom]
Fe_1	3/2	3/2→1/2	5.83±0.08	6.53±0.09
Fe_2	3	3→2	5.98±0.09	5.20±0.09
Fe_3	9/2	9/2→7/2	6.5±0.2	5.5±0.2
Co_1	1	1→0	10.25±0.15	10.25±0.15
Co_2	2	2→1	8.2±0.4	5.5±0.3
Co_3	3	3→2	8.3±1.2	5.0±0.8

resulting in impurity spins that are not exactly half integer. Thus this treatment is only an approximation. More sophisticated approaches would be needed to fully account for the itinerant character of the impurity.

Knowing the spin of the system enables us to translate the excitation energy to the MAE. The resulting values are 10.25 meV per Co and 6.53 meV per Fe atom (see Table 6.1).

6.1.3 Comparison between experimental and theoretical MAE for single atoms

The task of measuring the magnetic anisotropy of single Co atoms on Pt(111) has already been accomplished using a different method, namely X-ray magnetic circular dichroism (XMCD) [28]. There have been as well several attempts to calculate the MAE theoretically [80, 28, 77]. Here we can compare our results with the findings of others (see Table 6.2).

The MAE value measured by XMCD is 9.3 ± 1.6 meV for a Co atom, matching perfectly with our value within the error bar. Note that the lateral resolution of XMCD is limited by the cross-section of the X-ray beam, meaning that the measurement is not performed on individual atoms, but shows an average value for a large ensemble of atoms. This also makes it impossible to distinguish between atoms on fcc and hcp sites.

The calculations by Etz *et al.* [80], modelling the atom as an impurity embedded into a two-dimensional translationally invariant semi-infinite fcc host, only take into account atoms adsorbed on fcc sites. These calculations also totally neglect relaxations, which can strongly affect the anisotropy (see below). Surprisingly, the results obtained for the Fe atom on Pt(111) are quite close to the value obtained in our experiment. The value for Co is, however, way off from both experimental results.

A more precise calculation, including the adatom relaxation and addressing both fcc and hcp adsorption sites, was done by A. Ernst [77]. These calculations show that the magnetic moment and the MAE strongly depend on the distance between the atom and the surface. As this distance is also slightly affected by the STM tip, the experiment geometry was taken into account. The calculations

Table 6.2: Theoretical and experimental values of the MAE of Fe and Co.

Atom	STS	XMCD [28]	Theory [80]	Theory [77]
Fe	6.53 ± 0.09	-	5.3 (fcc)	3.2 (fcc) 0.4 (hcp)
Co	10.25 ± 0.15	9.3 ± 1.6	5.0 (fcc)	3.1 (fcc) 3.8 (hcp)

also show that there is a rather strong difference in the MAE of atoms on different crystallographic sites. However, in the energy minimum, the calculated MAE for Fe atoms is approximately 3.2 meV in fcc and 0.4 meV in hcp positions and for Co atoms 3.1 meV in fcc and 3.8 meV in hcp positions. The values are smaller than the experimental ones, but of the same order of magnitude. The MAE value for Fe in hcp position is, however, significantly smaller than the experimental value. This suggests that Fe in the fcc position is mainly probed in the experiment. Since the potential barrier for hopping from an fcc to an hcp site is ≈ 0.2 eV [84], thermal diffusion between these two sites is unlikely at 4.3 K. A more likely reason lies in high currents used in the experiment, that would supply enough energy for the atom to hop from an hcp to a more stable fcc site.

To conclude, the results of our STS investigation confirm the high magnetic anisotropy of Co atoms on Pt(111), as first discovered by XMCD [28], and are significantly more precise. We discover that Fe atoms on the same substrate have a comparable, but lower MAE. The results also show a reasonable agreement with theory. Theoretical calculations also provide a possible explanation for the fact that we do not see a difference between fcc and hcp adsorption sites in the experiment.

6.2 Modes in dimers and trimers

The XMCD measurements, mentioned in the previous section, have also been performed for atomic clusters, to study the evolution of MAE in a system of changing symmetry. The clusters, however, were self-assembled via thermal diffusion, leading to an uncertainty in cluster size, and, consecutively, to a large error of the final values. The MAE was determined to 3.3 ± 0.4 meV for cluster with a size of 2.8 ± 1.5 atoms [28]. The possibility of atomic manipulation with an STM allows us to avoid this problem and to investigate individual clusters of well-defined dimensions.

6.2.1 Dimers

In the case of a dimer, the interaction with an electron leads to a transition from a ground state $|s, s\rangle$, where s is the spin of a single atom in the dimer, to a superposition of states, where the spin of one of the composing atoms is changed by one, namely $|s, s-1\rangle$ and $|s-1, s\rangle$. There are two linear combinations of these

states that form an eigenstate,

$$\Psi_1 = \frac{1}{\sqrt{2}} |s,\, s-1\rangle + \frac{1}{\sqrt{2}} |s-1,\, s\rangle \,, \tag{6.2}$$

$$\Psi_2 = \frac{1}{\sqrt{2}} |s,\, s-1\rangle - \frac{1}{\sqrt{2}} |s-1,\, s\rangle \,. \tag{6.3}$$

The energies of the two states are different, so two inelastic excitation signatures are expected in the spectrum.

The cluster in the first state has a total spin of $S = 2s$ and the z projection $S_z = 2s - 1$. Thus, this state can be described as a rotation of the total spin of the cluster in the analogy to the excitation of an individual atom. The energy of this excitation can therefore be related to the classical MAE of the whole cluster as before. Another description of this state is an in-phase rotation of the two atomic spins.

The experimentally obtained energy of the first excitation of the cluster is lower than the value obtained for the single atom, but is of the same order of magnitude. This excitation is observed with equal ease in Fe and Co dimers. As before, a Gaussian fit to the spectra is used to obtain the energies and a statistical analysis provides the final value, due to a certain dispersion of the energy values between measurements. The results for Fe and Co dimers are presented in Fig. 6.5 and in Table 6.1. Note that the fit of the histogram for Co dimers is not entirely unambiguous, as one can argue that more than one distinct peak is visible. However, the small amount of measurements does not allow a decisive statement at this point. Therefore, we assume here that there is only one energy value and fit the histogram accordingly. The MAE was calculated from obtained excitation energies analogously to the case of single atoms. The resulting MAE values are 5.2 meV for an Fe dimer and 5.5 meV for a Co dimer.

In the second state the dimer has a spin of $S = S_z = 2s - 1$. Viewed classically, the time evolution of this state is equivalent to an out-of-phase precession of the two spins (a magnon with $q \neq 0$). The energy of the state is higher due to the exchange interaction between the two spins coming into play. The total energy cost of this excitation is a sum of the exchange and the anisotropy contributions, $E_{\mathrm{x}} = 2Js - D(4s - 1)$ (see A.3.2). As the exchange constant J is of the order of tens of meV/$\hbar^2$ in bulk Fe and Co, one can expect an inelastic peak around 100 meV. And indeed such a peak is observed, as shown on Fig. 6.6. Combining the data for all dimers into a histogram gives two groups of energies, one with the mean of 54 ± 2 meV and the other at 108 ± 2 meV, giving J of 16 ± 1 meV/$\hbar^2$ and 34 ± 1 meV/$\hbar^2$, respectively. Again, the limited number of measurements hinders our ability to determine the reason for the variation in the excitation energy. One possible influencing factor might be the exact configuration of a dimer. Two types of adsorption sites give rise to a multitude of possible configurations, such as fcc-fcc, fcc-hcp and hcp-hcp dimers. The number of configuration increases if one considers atoms not sitting in nearest-neighbour positions. To investigate

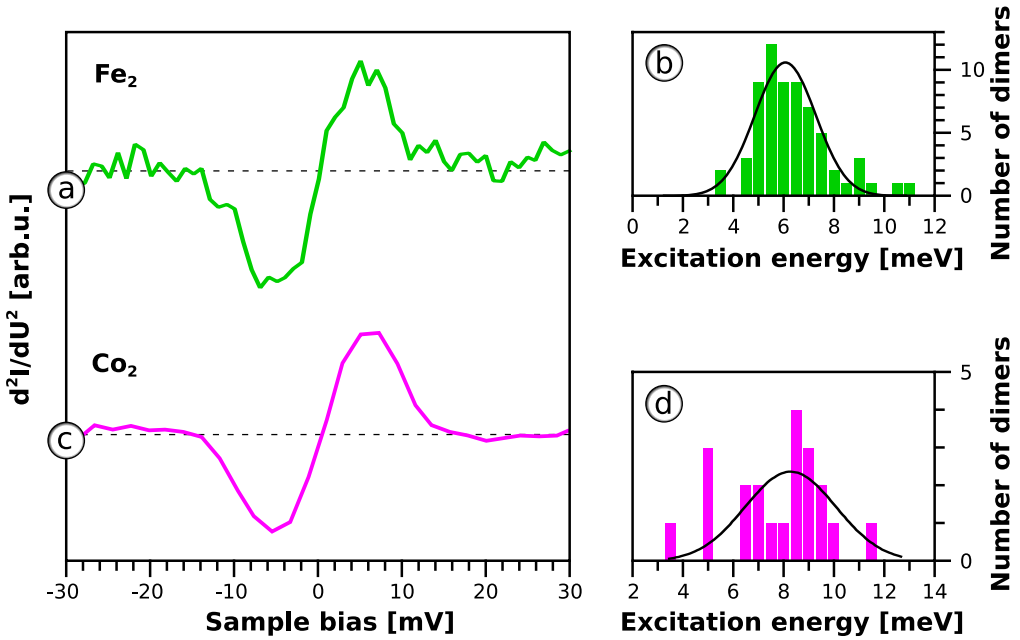

Figure 6.5: Inelastic spectra for Fe (a) and Co (c) dimers. The corresponding energy distribution histograms for (b) 65 measurements on Fe and (d) 27 measurements on Co dimers are fitted each with a single Gaussian to obtain the mean excitation energy value.

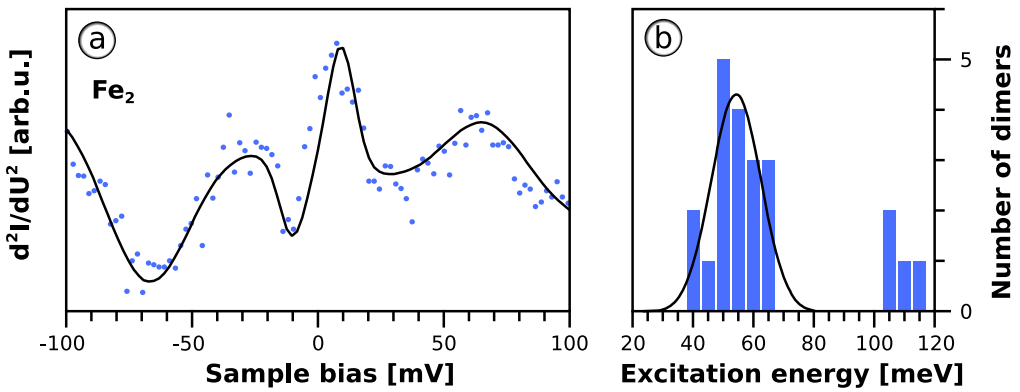

Figure 6.6: (a) Inelastic spectrum taken on an Fe dimer, with two inelastic excitations visible. (b) Energies of the second excitation collected from 22 measurements.

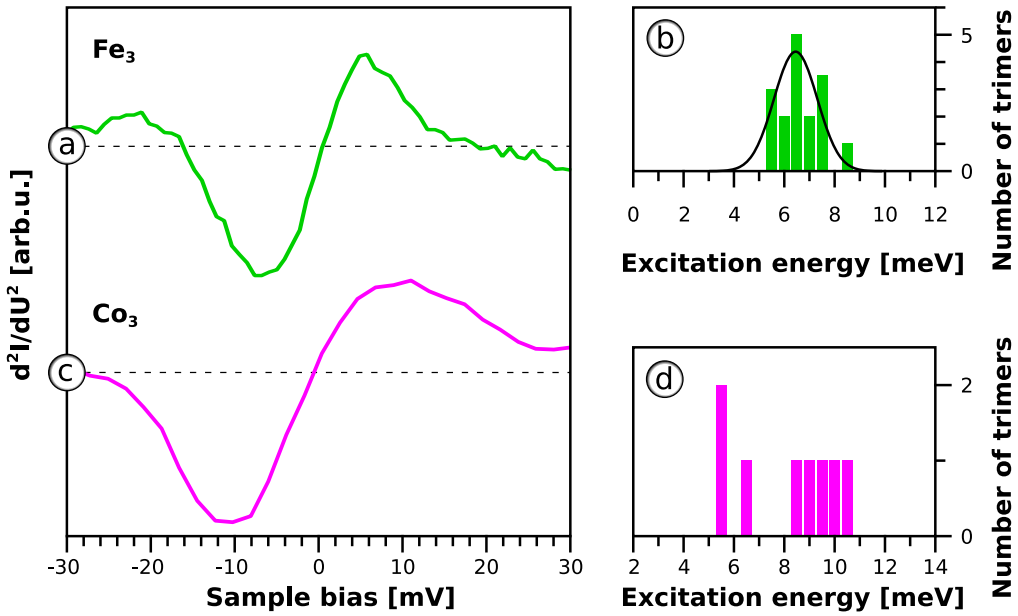

Figure 6.7: Inelastic spectra for Fe (a) and Co (c) trimers. The corresponding energy distribution histograms for (b) 16 measurements on Fe and (d) 8 measurements on Co trimers are fitted each with a single Gaussian to obtain the mean excitation energy value.

this issue, theoretical first-principles calculations of the exchange energy of a Fe dimer on Pt(111) were performed and various configurations of the Fe dimer were investigated [77]. The energetically favourable configuration is a dimer with Fe atoms occupying next nearest neighbour fcc and hcp positions. In this case the magnetic moments of Fe atoms align in parallel and are about 2.85 μ_B per Fe atom including the substrate. The exchange constant J was estimated to be 11 meV in good agreement with the first measured energy. The lower probability of finding a dimer with a second excitation energy at 100 meV seems to confirm that the first configuration is favourable. However, all investigated dimers are stable in the sense that the energy of the second excitation may vary from measurement to measurement, but never jumps from one group to another.

6.2.2 Trimers

In the trimer, the excited state is a superposition of three states, one for each atom, giving three possible excited configurations. The actual energy of the states depends strongly on the physical configuration of a trimer, which affects the exchange coupling. As trimers appear round in our topographic scans, one can assume a triangular configuration with equal coupling between all atomic pairs. In this case there are two possible excitation energies as the higher state is degenerate. The energy of this state is $3Js - D(6s - 1)$ (see A.3.2).

The MAE of trimers, estimated from the inelastic spectra, gives values that

are very close to the dimer values (see Fig. 6.7 and Table 6.1). Once again, the values obtained for the Co trimer do not display a single pronounced peak in the histogram. The energy value was obtained in the assumption that there really exists only one configuration.

The higher mode could also be observed, but due to an increased peak width it is often impossible to separate the signal from the noise and to reliably deduce the excitation energy. An average of the best five measurements gives an energy of $60 \pm 10\,\mathrm{meV}$ and J equal to $16 \pm 4\,\mathrm{meV}/\hbar^2$.

6.3 Magnetisation dynamics

The probability of the scattering event can be estimated from the inelastic curves. Since it is impossible to discern the step in the numerically differentiated $I(U)$, one has to use the area under the peak in $\mathrm{d}^2I/\mathrm{d}U^2$. But since the $\mathrm{d}^2I/\mathrm{d}U^2$ curve was obtained with a lock-in amplifier, there is an unknown scaling factor introduced during measurement. However, it is known a priori that this factor scales linearly with the tunnelling current, quadratically with the lock-in modulation and linearly with signal amplification. Therefore, the final value was calculated by comparing the area under the magnon peak for bulk Fe(100) from Chapter 4, where the absolute value is known, with the area under the anisotropy peak, scaled to match the measurement conditions of the other experiment. This calculation gives a scattering probability of 2 %.

6.3.1 Peak widths and lifetimes

One notices that not only the position of the peaks changes for different clusters and materials, but also their widths. The width of the peak W in the ISTS experiment depends on three parameters: the intrinsic width W_{in}, that depends on lifetime τ of the excitation via the uncertainty principle $\tau W_{\mathrm{in}} \gtrapprox \hbar/2$, the experiment temperature T and the bias modulation U_{mod} used to obtain the second derivative. Since the last two parameters are known, the lifetime can be extracted from the spectra [11],

$$\tau = \hbar / \left[2\sqrt{W^2 - (5.4kT)^2 - (1.7\mathrm{e}U_{\mathrm{mod}})^2} \right] \tag{6.4}$$

This procedure, applied to the observed excitations, gives the values as detailed in Table 6.3. All the values are of the order of tens of femtoseconds. As the width of the peaks tends to disperse more than the peak position, the precision of the values is around $\pm 5\,\mathrm{fs}$.

A general conclusion that can be drawn from these values is that the lifetime of any of the excitations is much shorter than the time between scattering events. The maximal currents used in the experiment are of the order of 100 nA, i.e. approximately 10^{12} electrons per second. With 2 % of the electrons scattering, it gives

Table 6.3: Lifetimes of excited states of atoms and clusters in fs

	atom	dimer	trimer	dimer non-collinear
Fe	55	45	30	10
Co	20	45	30	

a maximum of one spin flip in 10 ns, a time scale at least six orders of magnitude larger than the relaxation time. It follows that it is impossible to excite higher order events in these experiments, as the system will fully relax way before the second scattering event[3].

Secondly, the excitation lifetimes tend to decrease with decreasing cluster size. The only exception from this rule is the lifetime of a single excited Co atom, that is noticeably smaller than the value for the Fe atom. A possible reason for this effect may lay in the spin configuration of the excited state. An excited Co atom has $S_z = 0$, and can thus relax into states with $S_z = \pm 1$, that both have the same energy. All the other clusters have a higher spin in the excited state and only one relaxation direction. This would effectively halve the lifetime of the excited state of Co with respect to other clusters, in good agreement with the measured value. A further reduction of the lifetime is caused by a stronger hybridisation of Co with the substrate, as manifested by the higher MAE values.

These observations also explain the absent hysteresis in recent experiments on the influence of magnetic field on the magnetisation of Co atoms on Pt(111) [85]. The authors have shown that the local DOS of a Co atom depends on its magnetisation direction. It was expected that by applying a magnetic field perpendicular to the surface and measuring the DOS with STM it would be possible to observe a hysteretic behaviour. The experimental results show, however, a paramagnetic behaviour of the magnetisation with no visible hysteresis. Taking into account the chosen bias voltage of 200 mV, the tunnelling current of 1 nA and the averaging times of 10 ms one realises that the magnetisation state of the atom is not stable during the experiment, but is switched to the $S_z = 0$ state and relaxed many times on the experimental timescale. The probability to relax to one of the $S_z = \pm 1$ states is defined by the magnetic field and at zero field both relaxation directions become equally probable. The average magnetisation direction observed in the experiment should then gradually go from 'up' for high 'up' fields through zero for zero field to 'down' for a 'down' field in full agreement with the experimental observation. It follows that the hysteresis can only be observed for atoms with higher spins, where the spin direction cannot be totally reversed with one spin-flip and is not equal to zero on average in zero field but depends on the initial state.

Finally, the non-collinear state has the shortest lifetime of all. A likely reason for this is given by the exchange interaction between electrons. While this interaction conserves S_z, it may alter S such that the noncollinear state can quickly decay into

[3]Using higher currents in the μA range will, of course, decrease the time between scattering events, but it will also heat up the system locally, leading to "wandering" atoms and clusters.

a collinear excited state with identical S_z.

These lifetimes give information on the magnetisation dynamics of the atoms not accessible by earlier mentioned XMCD measurements. The extremely short lifetimes in these metallic systems indicate an efficient relaxation process, which is absent for magnetic ions in insulator structures [86]. Since comparable MAEs were found in our metallic structures and in insulator structures, one can exclude the responsibility of the spin-orbit interaction for the short lifetimes in the metallic case. More likely, the strong hybridisation of the atomic states with the Pt substrate states leads to efficient electron-electron scattering processes that relax the magnetic state of the atom.

6.3.2 Stability of magnetic atoms and clusters

The thermal stability of Fe and Co atoms and clusters can be obtained within the classical Boltzmann description as

$$f = -K/h \times \mathrm{e}^{K/k_\mathrm{B}T}$$

where f is the frequency of switching between the two out-of-plane states ($S_z = \pm S$). At the temperature of 4 K this gives a time between termally induced flips of less than a second. Stability required for applications is only reachable at temperatures below 3 K.

The stability is further reduced by quantum-mechanical effects. One of the possible spin reversal mechanism is a tunnelling between magnetic states [87]. This tunnelling is induced by either a transversal magnetic field (absent in our studies) or by in-plane anisotropy terms. Due to the threefold symmetry of the substrate, the lowest in-plane term is of sixth order. Such a term is, however, only possible for spin states with at least $S = 3$ and can thus be excluded for Fe and Co single atoms. An additional mechanism for spin reversal is provided by electron-electron interaction. As we know, the excited state is smeared in energy due to its short lifetime. Thus an overlap of the ground state and the excited state is possible even for a large MAE. This results in a non vanishing transition probability between the degenerate ground states via an excited intermediate state.

We note that the stability of magnetisation in small clusters is therefore related to the hybridisation in two opposing ways. On one hand, the hybridisation increases the splitting between the ground states and the excited states, increasing the thermal stability. On the other hand it decreases the lifetime of the excited state and thus increases the overlap between the ground state and the excited state, leading to an increased probability of the spin transition.

Chapter 7

Conclusions

The actively growing field of nanomagnetism and spintronics needs a reliable technique to study the interaction between an external actor (e.g. an electric current) and the magnetic system. This technique should also be able to explore the evolution of the magnetically excited state on a scale of few nanometres. We believe that inelastic scanning tunnelling spectroscopy (ISTS) may become such a technique. The elementary excitations of a magnetic system, that largely determine its behaviour under external influence, are well accessible with ISTS even in systems consisting only of few atoms — the size that is too small to reach with conventional methods.

ISTS can not only be applied to studies of the energy distribution of such excitations, but can also provide information on the mechanism of the interaction between the current and the magnetic system, i.e. the spin torque effect. This effect has a great future in applications, such as magnetic random access memory. The STM is a well defined tunnel junction, and can be used to directly study the effect of spin torque in system of different magnetic configuration and with high lateral resolution.

Currently ISTS is unrivalled in the area of magnetic excitations of systems consisting of a small number of atoms. Combined with the possibility of atomic manipulation this opens a way to a study of magnetic excitations in manually engineered systems and to a possible construction of a system with a well defined magnetic excitation spectrum, acting as a logical spin gate or a spin-dependent low-pass electron filter.

In this work we have shown how elementary magnetic excitations can be accessed with ISTS and have studied the influence of the magnetic configuration of the system and the external magnetic field on the spectra. We have demonstrated with help of theoretically calculated density of states of the samples, that the probability of magnon creation changes depending on the direction of the current, and the magnitude of the change is defined by the spin polarisation of the density of states. We have discovered that the interaction between the hot electrons and the electrons defining the magnetisation is not localised and has an oscillating RKKY-

like behaviour in real space, leading to a preferential creation of magnons with low energies.

Changing the dimensions of the systems also changes its properties and we have investigated the behaviour of magnetic excitations in two-dimensional systems, i.e. magnetic thin films. We obtained the magnon dispersion for almost the whole Brillouin zone in Co and Ni on Cu(100), well matching with the dispersion in bulk Co and Ni. We have shown that reduced dimensions lead to a decrease of the excitation energies in the whole zone. We have also seen the decrease of the excitation lifetimes with increasing energies due to the proximity of the Stoner continuum.

A further reduction of dimensions brought us to the magnetic system consisting of a single magnetic atom with only one excited state. We have explored the influence of the coupling with the substrate on the lifetime of the excited state and on the magnetic anisotropy of the system. By constructing larger systems with several atoms combined to a cluster we have studied the influence of the symmetry of the environment on the magnetic stability of the cluster and the energy of the excited state. We have extracted magnetic anisotropy energies for Fe and Co atoms, dimers and trimers on Pt(111). The obtained results agree well with previous investigations of the magnetic anisotropy of Co atoms and clusters on Pt(111) obtained with X-ray magnetic circular dichroism. Due to a better resolution, however, our results have smaller errors in both energies and cluster sizes. We have registered non-collinear excited states in the clusters with a much reduced lifetime and determined the strength of the exchange coupling between individual magnetic atoms.

We can conclude that ISTS is able to provide a lot of information on the magnetic excitations in any magnetic system. The excitation probability, the spectrum and the lifetimes of magnons are accessible by this technique where the established techniques fail. This makes it a promising and a unique method and we expect many interesting results from future experiments.

The biggest difficulty in the ISTS experiments performed here is the inadequacy of the theoretical models in the description of the investigated systems. Some questions, arising in the process of data analysis, remain partially unanswered or one has to resort to crude models, often leading to unsatisfactory agreement with the experiment. Several of these questions have not been asked before and some are too difficult to be answered in the current state of theory development. The itinerant electrons magnetism is poorly described, especially in the case that the second-order effects like electron correlations start to be noticeable. The future development of theory and experiment might shed some new light on these results and affect our understanding of magnetic excitations.

Appendix A

Calculating magnon modes

A.1 General information

To solve the Schrödinger equation with the Heisenberg Hamiltonian in the standard form for the interaction between two spins $\vec{S}_i$ and $\vec{S}_j$

$$\mathcal{H}_{ij} = -J_{ij}\vec{S}_i\vec{S}_j \tag{A.1}$$

the Hamiltonian should be written in different operators, namely one has to select the z axis and go to S^+, S^- and S^z, where operators

$$S^+ = S^x + iS^y \tag{A.2}$$
$$S^- = S^x - iS^y \tag{A.3}$$

act like

$$S^+ |s\rangle = \hbar\sqrt{(S-s)(S+s+1)}\,|s+1\rangle \tag{A.4}$$
$$S^- |s\rangle = \hbar\sqrt{(S+s)(S-s+1)}\,|s-1\rangle \tag{A.5}$$

The $|s\rangle$ above is the wavefunction for spin s state[1]. Maximum spin is S.

One also needs the commutator

$$\left[S^z, S^\pm\right] = \pm\hbar S^\pm \tag{A.6}$$

extended to

$$\left[S_i^z, S_j^\pm\right] = \pm\hbar S_j^\pm \delta_{ij} \tag{A.7}$$

Now the interaction can be rewritten as

$$\mathcal{H}_{ij} = -J_{ij}\left[\frac{1}{2}\left(S_i^- S_j^+ + S_i^+ S_j^-\right) + S_i^z S_j^z\right] \tag{A.8}$$

[1]Here and further on "spin state s" means the state with $S^z |s\rangle = \hbar s |s\rangle$

A.2 General solution of the Schrödinger equation

A.2.1 The ansatz

A magnon is a collective excitation. This means that its wavefunction must be a superposition of individual excitations. For practical ISTS purposes an individual excitation must be the ground state $|\mathcal{G}\rangle$ with one of the spins reduced by $1\hbar$. This means (in a ferromagnet)

$$\Psi_i = \frac{1}{\sqrt{2S}} S_i^- |\mathcal{G}\rangle \tag{A.2.1.1}$$

$$\Psi = \sum_i \tilde{A}_i \Psi_i = \sum_i A_i S_i^- |\mathcal{G}\rangle \tag{A.2.1.2}$$

with the normalisation

$$1 = \sum_i 2\hbar^2 S_i |A_i|^2 \tag{A.2.1.3}$$

A.2.2 Solving the equation

The equation that we want to solve looks like

$$\begin{aligned} E\Psi &= \mathcal{H}\Psi \\ &= -\frac{1}{2} \sum_{i \neq j} J_{ij} \left[\frac{1}{2} \left(S_i^- S_j^+ + S_i^+ S_j^- \right) + S_i^z S_j^z \right] \sum_m A_m S_m^- |\mathcal{G}\rangle \end{aligned} \tag{A.2.2.1}$$

Let's first calculate some partial sums ($i \neq j$).

$$S_i^+ S_j^- S_m^- |\mathcal{G}\rangle = \delta_{im}(1 - \delta_{jm}) 2\hbar^2 S_m S_j^- |\mathcal{G}\rangle = 2\hbar^2 S_m \delta_{im} S_j^- |\mathcal{G}\rangle \tag{A.2.2.2}$$

$$S_i^- S_j^+ S_m^- |\mathcal{G}\rangle = (1 - \delta_{im}) \delta_{jm} 2\hbar^2 S_m S_j^- |\mathcal{G}\rangle = 2\hbar^2 S_m \delta_{jm} S_i^- |\mathcal{G}\rangle \tag{A.2.2.3}$$

$$S_i^z S_j^z S_m^- |\mathcal{G}\rangle = \hbar^2 S_i S_j S_m^- |\mathcal{G}\rangle - \hbar^2 S_j \delta_{im} S_m^- |\mathcal{G}\rangle - \hbar^2 S_i \delta_{jm} S_m^- |\mathcal{G}\rangle \tag{A.2.2.4}$$

Expanding Eq. A.2.2.1

$$
\begin{aligned}
E\Psi &= -\frac{1}{2}\sum_{i\neq j}\sum_{m} J_{ij}\left[\frac{1}{2}\Big(A_m S_i^- S_j^+ S_m^- \left|\mathcal{G}\right\rangle + A_m S_i^+ S_j^- S_m^- \left|\mathcal{G}\right\rangle\Big) + A_m S_i^z S_j^z S_m^- \left|\mathcal{G}\right\rangle\right] \\
&= -\frac{1}{2}\sum_{i\neq j}\sum_{m} J_{ij}\left[\frac{1}{2}\Big(2\hbar^2 A_m S_m \delta_{jm} S_i^- \left|\mathcal{G}\right\rangle + 2\hbar^2 A_m S_m \delta_{im} S_j^- \left|\mathcal{G}\right\rangle\Big)\right. \\
&\qquad \left. + \hbar^2 A_m S_i S_j S_m^- \left|\mathcal{G}\right\rangle - \hbar^2 A_m S_j \delta_{im} S_m^- \left|\mathcal{G}\right\rangle - \hbar^2 A_m S_i \delta_{jm} S_m^- \left|\mathcal{G}\right\rangle\right] \\
&= -\frac{\hbar^2}{2}\sum_{i\neq j} J_{ij}\Big(A_j S_j S_i^- \left|\mathcal{G}\right\rangle + A_i S_i S_j^- \left|\mathcal{G}\right\rangle + S_i S_j \sum_m A_m S_m^- \left|\mathcal{G}\right\rangle \\
&\qquad - A_i S_j S_i^- \left|\mathcal{G}\right\rangle - A_j S_i S_j^- \left|\mathcal{G}\right\rangle\Big) \\
&= -\frac{\hbar^2}{2}\sum_{i\neq j} J_{ij}\Big(S_i S_j \Psi + (A_j - A_i) S_j S_i^- \left|\mathcal{G}\right\rangle + (A_i - A_j) S_i S_j^- \left|\mathcal{G}\right\rangle\Big) \qquad \text{(A.2.2.5)} \\
&= -\frac{\hbar^2}{2}\sum_{i\neq j} J_{ij} S_i S_j \Psi - \hbar^2 \sum_{i\neq j} J_{ij}(A_j - A_i) S_j S_i^- \left|\mathcal{G}\right\rangle \qquad \text{(A.2.2.6)} \\
&= E_0\Psi + \hbar^2 \sum_i \sum_j (1-\delta_{ij}) J_{ij} S_j \left(1 - \frac{A_j}{A_i}\right) A_i S_i^- \left|\mathcal{G}\right\rangle \\
&= E_0\Psi + E^*\Psi \qquad \text{(A.2.2.7)}
\end{aligned}
$$

where

$$
E^* = \hbar^2 \sum_j (1-\delta_{ij}) J_{ij} S_j \left(1 - \frac{A_j}{A_i}\right) \qquad \text{(A.2.2.8)}
$$

must be i-independent.

In the case of nearest-neighbour (n.n.) approximation with $J_{ij} = J\delta_{ij}^{\text{n.n.}}$ and $S_i = S$

$$
E^* = \hbar^2 JS \left(N_{\text{n.n.}} - \frac{\sum_{\text{n.n.}} A_j}{A_i}\right) \qquad \text{(A.2.2.9)}
$$

A.3 Application to individual systems

A.3.1 Periodic lattice

In the case of a periodic lattice, Eq. A.2.2.9 has a general solution of the form

$$
A_i = \frac{1}{\hbar\sqrt{2S}}\, \mathrm{e}^{i\vec{q}\vec{R}_i} \qquad \text{(A.3.1.1)}
$$

This is a wave with wavevector $\vec{q}$. The energy of the wave is

$$E^* = \hbar^2 JS \left(N_{\text{n.n.}} - \sum_{\text{n.n.}} \mathrm{e}^{i\vec{q}(\vec{R}_j - \vec{R}_i)} \right) \tag{A.3.1.2}$$

$$= \hbar^2 JS \left(N_{\text{n.n.}} - \sum_{\vec{r}} \cos \vec{q}\vec{r} \right) \tag{A.3.1.3}$$

where $\vec{r}$ iterates over the vectors between an arbitrary atom and its nearest neighbours.

The top of the band is thus at

$$E^*_{\max} = 2\hbar^2 JSN_{\text{n.n.}} \tag{A.3.1.4}$$

Examples

Simple cubic lattice

$$\vec{r} = \left\{ (\pm a, 0, 0), (0, \pm a, 0), (0, 0, \pm a) \right\} \tag{A.3.1.5}$$

$$E^* = 2\hbar^2 JS \left(3 - \cos q_x a - \cos q_y a - \cos q_z a\right) \tag{A.3.1.6}$$

Body-centred cubic lattice

$$\vec{r} = \left(\pm\frac{a}{2}, \pm\frac{a}{2}, \pm\frac{a}{2} \right) \tag{A.3.1.7}$$

$$E^* = 8\hbar^2 JS \left(1 - \cos\frac{q_x a}{2} \cos\frac{q_y a}{2} \cos\frac{q_z a}{2} \right) \tag{A.3.1.8}$$

Face-centred cubic lattice

$$\vec{r} = \left\{ \left(\pm\frac{a}{2}, \pm\frac{a}{2}, 0 \right), \left(\pm\frac{a}{2}, 0, \pm\frac{a}{2} \right), \left(0, \pm\frac{a}{2}, \pm\frac{a}{2} \right) \right\} \tag{A.3.1.9}$$

$$E^* = 4\hbar^2 JS \left(3 - \cos\frac{q_x a}{2} \cos\frac{q_y a}{2} - \cos\frac{q_x a}{2} \cos\frac{q_z a}{2} - \cos\frac{q_y a}{2} \cos\frac{q_z a}{2} \right) \tag{A.3.1.10}$$

A.3.2 Linear chain

An infinite linear chain is a one-dimensional periodic lattice, so the solution

$$E^* = \hbar^2 JS \left(N_{\text{n.n.}} - \sum_{\vec{r}} \cos \vec{q}\vec{r} \right) \tag{A.3.2.1}$$

still holds with $\vec{r} = \pm a$. Thus

$$E^* = 2\hbar^2 JS(1 - \cos qa) \tag{A.3.2.2}$$

If the chain isn't infinite, the solution is less simple. Starting anew with Eq. A.2.2.9

$$E^* = \hbar^2 JS\left(1 - \frac{A_2}{A_1}\right) \tag{A.3.2.3}$$

$$= \hbar^2 JS\left(2 - \frac{A_{j-1} + A_{j+1}}{A_j}\right), \quad j = 2, \ldots, N-1 \tag{A.3.2.4}$$

$$= \hbar^2 JS\left(1 - \frac{A_{N-1}}{A_N}\right) \tag{A.3.2.5}$$

This is an eigenvalue problem with a matrix

$$\begin{pmatrix} 1 & -1 & & & 0 \\ -1 & 2 & -1 & & \\ & \ddots & \ddots & \ddots & \\ & & -1 & 2 & -1 \\ 0 & & & -1 & 1 \end{pmatrix}$$

A general solution for a system with this matrix is

$$A_j = \frac{1}{\sqrt{2S}} \cos qa(j - \frac{1}{2}) \tag{A.3.2.6}$$

$$E^* = 2\hbar^2 JS(1 - \cos qa) \tag{A.3.2.7}$$

where

$$q = \frac{\pi}{a}\frac{n}{N}, n = 0, 1, \ldots, N-1 \tag{A.3.2.8}$$

A.3.3 Atomic ring

An atomic ring is basically an infinite chain with quantisation. If

$$A_n = \mathrm{e}^{i\,q\,a\,n} \tag{A.3.3.1}$$

then

$$A_{N+1} = \mathrm{e}^{i\,q\,a(N+1)} \tag{A.3.3.2}$$

$$= A_1\,\mathrm{e}^{i\,q\,a\,N}, \tag{A.3.3.3}$$

so

$$\mathrm{e}^{i\,q\,a\,N} = 1 \tag{A.3.3.4}$$

$$qaN = 2\pi m \tag{A.3.3.5}$$

$$q_m = \frac{2\pi}{aN} m, m = 0, \ldots, N-1 \tag{A.3.3.6}$$

$$E^* = 2\hbar^2 JS(1 - \cos q_m a) \tag{A.3.3.7}$$

A.3.4 Thin film

A thin film is a finite chain of infinite 2D planes. The following form for the wavefunction coefficients can be assumed

$$A_i^k = \exp(i\vec{q_\parallel}\vec{R}_i)B_k \tag{A.3.4.1}$$

where k is the layer index. Eq. A.2.2.9 becomes

$$E^* = \hbar^2 JS\Bigg[\Big(N_{\text{in}} - \sum_{\vec{r}_{\text{in}}} \cos\vec{q}_\parallel\vec{r}_{\text{in}}\Big) \tag{A.3.4.2}$$

$$+ \Big(N_{\text{out}} - \frac{B_{k-1}}{B_k}\sum_{\vec{r}_{\text{out}}} \cos\vec{q}_\parallel\vec{r}_{\text{out}}\Big) \tag{A.3.4.3}$$

$$+ \Big(N_{\text{out}} - \frac{B_{k+1}}{B_k}\sum_{\vec{r}_{\text{out}}} \cos\vec{q}_\parallel\vec{r}_{\text{out}}\Big)\Bigg] \tag{A.3.4.4}$$

$$\frac{E^*}{\hbar^2 JS} = N_{\text{in}} + N_{\text{out}} - \sum_{\vec{r}_{\text{in}}} \cos\vec{q}_\parallel\vec{r}_{\text{in}} - \frac{B_2}{B_1}\sum_{\vec{r}_{\text{out}}} \cos\vec{q}_\parallel\vec{r}_{\text{out}} \tag{A.3.4.5}$$

$$= N_{\text{in}} + 2N_{\text{out}} - \sum_{\vec{r}_{\text{in}}} \cos\vec{q}_\parallel\vec{r}_{\text{in}} - \frac{B_{k-1}+B_{k+1}}{B_k}\sum_{\vec{r}_{\text{out}}} \cos\vec{q}_\parallel\vec{r}_{\text{out}}, \quad k = 2,\ldots,N-1 \tag{A.3.4.6}$$

$$= N_{\text{in}} + N_{\text{out}} - \sum_{\vec{r}_{\text{in}}} \cos\vec{q}_\parallel\vec{r}_{\text{in}} - \frac{B_{N-1}}{B_N}\sum_{\vec{r}_{\text{out}}} \cos\vec{q}_\parallel\vec{r}_{\text{out}} \tag{A.3.4.7}$$

In the contrary to the case of a linear spin chain, there is no general solution. The eigenvalue problem has a matrix

$$\begin{pmatrix} a & -b & & & 0 \\ -b & a+1 & -b & & \\ & \ddots & \ddots & \ddots & \\ & & -b & a+1 & -b \\ 0 & & & -b & a \end{pmatrix}$$

where

$$a(\vec{q}_\parallel) = \frac{N_{\text{in}}}{N_{\text{out}}} + 1 - \sum_{\vec{r}_{\text{in}}} \cos\vec{q}_\parallel\vec{r}_{\text{in}}/N_{\text{out}} \tag{A.3.4.8}$$

$$b(\vec{q}_\parallel) = \sum_{\vec{r}_{\text{out}}} \cos\vec{q}_\parallel\vec{r}_{\text{out}}/N_{\text{out}} \tag{A.3.4.9}$$

At $\vec{q}_\parallel = 0$ the above becomes

$$a(0) = 1 \tag{A.3.4.10}$$

$$b(0) = 1 \tag{A.3.4.11}$$

which is exactly the case of an atomic linear chain. The corresponding energies should, however, be scaled up by N_{out}.

$$E^* = 2N_{\text{out}}\hbar^2 JS(1 - \cos(\pi n/N)), n = 0, \ldots, N-1 \tag{A.3.4.12}$$

List of abbreviations

bcc	Body-centered cubic structure
DOS	Density of states
fcc	Face-centered cubic structure
fct	Face-centered tetragonal structure
GMR	Giant magnetoresistance effect
ISTS	Inelastic scanning tunnelling spectroscopy
LEED	Low-energy electron diffraction
MAE	Magnetic anisotropy energy
MBE	Molecular beam epitaxy
MEED	Medium-energy electron diffraction
ML	Monolayer
RKKY	Ruderman-Kittel-Kasuya-Yoshida interaction
SPEELS	Spin-polarised electron energy loss spectroscopy
STM	Scanning tunnelling microscope
STS	Scanning tunnelling spectroscopy
STT	Spin transfer torque
UHV	Ultra-high vacuum
XMCD	X-ray magnetic circular dichroism

Bibliography

[1] Binasch, G., Grünberg, P., Saurenbach, F. & Zinn, W. Enhanced magnetoresistance in layered magnetic structures with antiferromagnetic interlayer exchange. *Phys. Rev. B* **39**, 4828–4830 (1989).

[2] Baibich, M. N., Broto, J. M., Fert, A., Van Dau, F. N., Petroff, F., Etienne, P., Creuzet, G., Friederich, A. & Chazelas, J. Giant magnetoresistance of (001)Fe/(001)Cr magnetic superlattices. *Phys. Rev. Lett.* **61**, 2472–2475 (1988).

[3] Chappert, C., Fert, A. & van Dau, F. N. The emergence of spin electronics in data storage. *Nature Mat.* **6**, 813–823 (2007).

[4] O'Leary, I., Labrune, V. & Lehane, S. Seagate ships desktop hard drive with world's highest areal density – 500 gb per disk. URL `http://media.seagate.com/2009/01/seagate-technology/seagate-ships-desktop-hard-drive-with-worlds-highest-areal-density-500gb-per-disk/`.

[5] Slonczewski, J. C. Conductance and exchange coupling of two ferromagnets separated by a tunneling barrier. *Phys. Rev. B* **39**, 6995–7002 (1989).

[6] Brockhouse, B. N. Scattering of neutrons by spin waves in magnetite. *Phys. Rev.* **106**, 859–864 (1957).

[7] Schreyer, A., Schmitte, T., Siebrecht, R., Bödeker, P., Zabel, H., Lee, S. H., Erwin, R. W., Majkrzak, C. F., Kwo, J. & Hong, M. Neutron scattering on magnetic thin films: Pushing the limits. *J. Appl. Phys.* **87**, 5443–5448 (2000).

[8] Hillebrands, B., Baumgart, P., Mock, R., Güntherodt, G., Boufelfel, A. & Falco, C. M. Collective spin waves in Fe-Pd and Fe-W multilayer structures. *Phys. Rev. B* **34**, 9000–9003 (1986).

[9] Pomerantz, M. Excitation of spin-wave resonance by microwave phonons. *Phys. Rev. Lett.* **7**, 312–313 (1961).

[10] Vollmer, R., Etzkorn, M., Kumar, P. S. A., Ibach, H. & Kirschner, J. Spin-polarized electron energy loss spectroscopy of high energy, large wave vector

spin waves in ultrathin fcc Co films on Cu(001). *Phys. Rev. Lett.* **91**, 147201 (2003).

[11] Stipe, B. C., Razaei, M. A. & Ho, W. Single-molecule vibrational spectroscopy and microscopy. *Science* **280**, 1732 (1998).

[12] Hirjibehedin, C. F., Lutz, C. P. & Heinrich, A. J. Spin coupling in engineered atomic structures. *Science* **312**, 1021–1024 (2006).

[13] Binnig, G. & Rohrer, H. Scanning tunneling microscopy—From birth to adolescence. *Rev. Mod. Phys.* **59**, 615 (1987).

[14] Bardeen, J. Tunnelling from a many-particle point of view. *Phys. Rev. Lett.* **6**, 57–59 (1961).

[15] Tersoff, J. & Hamann, D. R. Theory of the scanning tunneling microscope. *Phys. Rev. B* **31**, 805–813 (1985).

[16] Olesen, L., Brandbyge, M., Sørensen, M. R., Jacobsen, K. W., Lægsgaard, E., Stensgaard, I. & Besenbacher, F. Apparent barrier height in scanning tunneling microscopy revisited. *Phys. Rev. Lett.* **76**, 1485–1488 (1996).

[17] Julliere, M. Tunneling between ferromagnetic films. *Phys. Lett. A* **54**, 225–226 (1975).

[18] Wolf, E. L. *Principles of Electron Tunneling Spectroscopy* (Oxford University Press, New York, 1985).

[19] Olejniczak, W., Klusek, Z. & Bieniecki, M. Investigations of the fine structure of I(V) characteristics for highly oriented pyrolitic graphite surface by means of STM/STS at room temperature. *Appl. Phys. A* **66**, S191–196 (1998).

[20] Vitali, L., Schneider, M. A., Kern, K., Wirtz, L. & Rubio, A. Phonon and plasmon excitation in inelastic electron tunneling spectroscopy of graphite. *Phys. Rev. B* **69**, 121414 (2004).

[21] Balashov, T., Takács, A. F., Wulfhekel, W. & Kirschner, J. Magnon excitation with spin-polarized scanning tunneling microscopy. *Phys. Rev. Lett.* **97**, 187201 (2006).

[22] Sakurai, J. J. *Modern quantum mechanics* (Addison-Wesley, 1994), revised edn.

[23] Kittel, C. *Introduction to solid state physics* (Wiley, 1996), 7 edn.

[24] Heisenberg, W. Zur Theorie des Ferromagnetismus. *Z. Phys.* **49**, 619 (1928).

[25] Pajda, M., Kudrnovský, J., Turek, I., Drchal, V. & Bruno, P. Ab initio calculations of exchange interactions, spin-wave stiffness constants, and Curie temperatures of Fe, Co, and Ni. *Phys. Rev. B* **64**, 174402 (2001).

[26] Cottam, M. G. *Linear and non-linear spin waves in magnetic films and superlattices* (World Scientific, Singapore; River Edge, NJ, 1994).

[27] Gambardella, P., Dallmeyer, A., Maiti, K., Malagoli, M. C., Eberhardt, W., Kern, K. & Carbone, C. Ferromagnetism in one-dimensional monatomic metal chains. *Nature* **416**, 301–304 (2002).

[28] Gambardella, P. *et al.* Giant magnetic anisotropy of single cobalt atoms and nanoparticles. *Science* **300**, 1130 (2003).

[29] Bruno, P. Tight-binding approach to the orbital magnetic moment and magnetocrystalline anisotropy of transition-metal monolayers. *Phys. Rev. B* **39**, 865(R) (1989).

[30] Ibach, H. *Physics of Surfaces and interfaces* (Springer, Berlin, 2006).

[31] DeBlois, R. W. & C. D. Graham, J. Domain observations on iron whiskers. *J. Appl. Phys.* **29**, 931–939 (1958).

[32] Stroscio, J. A., Pierce, D. T., Davies, A., Celotta, R. J. & Weinert, M. Tunneling spectroscopy of bcc (001) surface states. *Phys. Rev. Lett.* **75**, 2960–2963 (1995).

[33] Lazewski, J., Korecki, J. & Parlinski, K. Phonons of (100) and (110) iron surfaces from first-principles calculations. *Phys. Rev. B* **75**, 054303 (2007).

[34] Xu, R., Hong, H., Zschack, P. & Chiang, T.-C. Direct mapping of phonon dispersion relations in copper by momentum-resolved X-ray calorimetry. *Phys. Rev. Lett.* **101**, 085504 (2008).

[35] Ishiki, M. & Igaki, K. Temperature dependence of the electrical resistivity of pure iron at low temperatures. *Transactions of the Japan Institute of Metals* **19**, 431–437 (1978).

[36] Wulfhekel, W., Zavaliche, F., Porrati, F., Oepen, H. P. & Kirschner, J. Nanopatterning of magnetic anisotropy by controlled strain relief. *Europhys. Lett.* **49**, 651–657 (2000).

[37] Wachowiak, A., Wiebe, J., Bode, M., Pietzsch, O., Morgenstern, M. & Wiesendanger, R. Direct observation of internal spin structure of magnetic vortex cores. *Science* **298**, 577–580 (2002).

[38] Wulfhekel, W., Zavaliche, F., Hertel, R., Bodea, S., Steierl, G., Liu, G., Kirschner, J. & Oepen, H. P. Growth and magnetism of Fe nanostructures on W(001). *Phys. Rev. B* **68**, 144416 (2003).

[39] Bode, M., Getzlaff, M. & Wiesendanger, R. Spin-polarized vacuum tunneling into the exchange-split surface state of Gd(0001). *Phys. Rev. Lett.* **81**, 4256–4259 (1998).

[40] Hong, J. & Mills, D. L. Theory of the spin dependence of the inelastic mean free path of electrons in ferromagnetic metals: A model study. *Phys. Rev. B* **59**, 13840–13848 (1999).

[41] Dastoor, P. C. & Allison, W. Growth of Co on Cu(111): Temperature dependence and interlayer spacings. *Phys. Rev. B* **64**, 085414 (2001).

[42] Hong, J. & Mills, D. L. Spin dependence of the inelastic electron mean free path in Fe and Ni: Explicit calculations and implications. *Phys. Rev. B* **62**, 5589–5600 (2000).

[43] Balashov, T., Takács, A. F., Däne, M., Ernst, A., Bruno, P. & Wulfhekel, W. Inelastic electron-magnon interaction and spin transfer torque. *Phys. Rev. B* **78**, 174404 (2008).

[44] de la Figuera, J., Prieto, J. E., Ocal, C. & Miranda, R. Scanning-tunneling-microscopy study of the growth of cobalt on Cu(111). *Phys. Rev. B* **47**, 13043–13046 (1993).

[45] Heckmann, O., Magnan, H., le Fevre, P., Chandesris, D. & Rehr, J. Crystallographic structure of cobalt films on Cu(001): elastic deformation to a tetragonal structure. *Surf. Sci.* **312**, 62–72 (1994).

[46] Sankey, J. C., Cui, Y.-T., Sun, J. Z., Slonczewski, J. C., Buhrman, R. A. & Ralph, D. C. Measurement of the spin-transfer-torque vector in magnetic tunnel junctions. *Nature Phys.* **4**, 67 (2008).

[47] Kubota, H. *et al.* Quantitative measurement of voltage dependence of spin-transfer torque in MgO-based magnetic tunnel junctions. *Nature Phys.* **4**, 37 (2008).

[48] Fominykh, N., Berakdar, J., Henk, J. & Bruno, P. Spectroscopy of the electron-electron interaction in solids. *Phys. Rev. Lett.* **89**, 086402 (2002).

[49] Ruderman, M. A. & Kittel, C. Indirect exchange coupling of nuclear magnetic moments by conduction electrons. *Phys. Rev.* **96**, 99 (1954).

[50] Moodera, J. S., Kinder, L. R., Wong, T. M. & Meservey, R. Large magnetoresistance at room temperature in ferromagnetic thin film tunnel junctions. *Phys. Rev. Lett.* **74**, 3273–3276 (1995).

[51] Tsoi, M., Jansen, A. G. M., Bass, J., Chiang, W.-C., Seck, M., Tsoi, V. & Wyder, P. Excitation of a magnetic multilayer by an electric current. *Phys. Rev. Lett.* **80**, 4281–4284 (1998).

[52] Krivorotov, I. N., Berkov, D. V., Gorn, N. L., Emley, N. C., Sankey, J. C., Ralph, D. C. & Buhrman, R. A. Large-amplitude coherent spin waves excited by spin-polarized current in nanoscale spin valves. *Phys. Rev. B* **76**, 024418 (2007).

[53] Berkov, D. & Miltat, J. Spin-torque driven magnetization dynamics: Micromagnetic modeling. *J. Magn. Magn. Mater.* **320**, 1238–1259 (2008).

[54] Morgenstern, K., Laegsgaard, E., Stensgaard, I., Besenbacher, F., Böhringer, M., Schneider, W.-D., Berndt, R., Mauri, F., De Vita, A. & Car, R. Stability of two-dimensional nanostructures. *Appl. Phys. A* **69**, 559–569 (1999).

[55] Schmid, A. K., Atlan, D., Itoh, H., Heinrich, B., Ichinokawa, T. & Kirschner, J. Fast interdiffusion in thin films: Scanning-tunneling-microscopy determination of surface diffusion through microscopic pinholes. *Phys. Rev. B* **48**, 2855–2858 (1993).

[56] Kowalewski, M., Schneider, C. M. & Heinrich, B. Thickness and temperature dependence of magnetic anisotropies in ultrathin fcc Co(001) structures. *Phys. Rev. B* **47**, 8748–8753 (1993).

[57] Liu, X., Steiner, M. M., Sooryakumar, R., Prinz, G. A., Farrow, R. F. C. & Harp, G. Exchange stiffness, magnetization, and spin waves in cubic and hexagonal phases of cobalt. *Phys. Rev. B* **53**, 12166–12172 (1996).

[58] Shirane, G., Minkiewicz, V. J. & Nathans, R. Spin waves in 3d metals. *J. Appl. Phys.* **39**, 383–390 (1968).

[59] Sinclair, R. N. & Brockhouse, B. N. Dispersion relation for spin waves in a fcc cobalt alloy. *Phys. Rev.* **120**, 1638–1640 (1960).

[60] Pickart, S. J., Alperin, H. A., Minkiewicz, V. J., Nathans, R., Shirane, G. & Steinsvoll, O. Spin-wave dispersion in ferromagnetic Ni and fcc Co. *Phys. Rev.* **156**, 623–626 (1967).

[61] Vollmer, R., Etzkorn, M., Kumar, P. S. A., Ibach, H. & Kirschner, J. Spin-wave excitation in ultrathin Co and Fe films on Cu(001) by spin-polarized electron energy loss spectroscopy. *J. Appl. Phys.* **95**, 7435–7440 (2004).

[62] Brown, R. H., Nicholson, D. M. C., Wang, X. & Schulthess, T. C. First principles theory of spin waves in Fe, Co, and Ni. *J. Appl. Phys.* **85**, 4830–4832 (1999).

[63] Mryasov, O. N., Freeman, A. J. & Liechtenstein, A. I. Theory of non-Heisenberg exchange: Results for localized and itinerant magnets. *J. Appl. Phys.* **79**, 4805–4807 (1996).

[64] Rosengaard, N. M. & Johansson, B. Finite-temperature study of itinerant ferromagnetism in Fe, Co, and Ni. *Phys. Rev. B* **55**, 14975–14986 (1997).

[65] Shallcross, S., Kissavos, A. E., Meded, V. & Ruban, A. V. An ab initio effective Hamiltonian for magnetism including longitudinal spin fluctuations. *Phys. Rev. B* **72**, 104437 (2005).

[66] van Schilfgaarde, M. & Antropov, V. P. First-principles exchange interactions in Fe, Ni, and Co. *J. Appl. Phys.* **85**, 4827–4829 (1999).

[67] Platow, W., Bovensiepen, U., Poulopoulos, P., Farle, M., Baberschke, K., Hammer, L., Walter, S., Müller, S. & Heinz, K. Structure of ultrathin Ni/Cu(001) films as a function of film thickness, temperature, and magnetic order. *Phys. Rev. B* **59**, 12641–12646 (1999).

[68] Farle, M., Platow, W., Anisimov, A. N., Poulopoulos, P. & Baberschke, K. Anomalous reorientation phase transition of the magnetization in fct Ni/Cu(001). *Phys. Rev. B* **56**, 5100–5103 (1997).

[69] Cooke, J. F., Lynn, J. W. & Davis, H. L. Calculations of the dynamic susceptibility of nickel and iron. *Phys. Rev. B* **21**, 4118–4131 (1980).

[70] Mook, H. A. & Paul, D. M. Neutron-scattering measurement of the spin-wave spectra for nickel. *Phys. Rev. Lett.* **54**, 227–229 (1985).

[71] Mankey, G. J., Willis, R. F. & Himpsel, F. J. Band structure of the magnetic fcc pseudomorphs: Ni(100), Co(100), and Fe(100). *Phys. Rev. B* **48**, 10284–10291 (1993).

[72] Savrasov, S. Y. Linear response calculations of spin fluctuations. *Phys. Rev. Lett.* **81**, 2570–2573 (1998).

[73] Eigler, D. M. & Schweizer, E. K. Positioning single atoms with a scanning tunnelling microscope. *Nature* **344**, 524 (1990).

[74] Bartels, L., Meyer, G. & Rieder, K.-H. Basic steps of lateral manipulation of single atoms and diatomic clusters with a scanning tunneling microscope tip. *Phys. Rev. Lett.* **79**, 697–700 (1997).

[75] Stepanyuk, V. S., Niebergall, L., Longo, R. C., Hergert, W. & Bruno, P. Magnetic nanostructures stabilized by surface-state electrons. *Phys. Rev. B* **70**, 075414 (2004).

[76] Wiebe, J., Meier, F., Hashimoto, K., Bihlmayer, G., Blügel, S., Ferriani, P., Heinze, S. & Wiesendanger, R. Unoccupied surface state on Pt(111) revealed by scanning tunneling spectroscopy. *Phys. Rev. B* **72**, 193406 (2005).

[77] Balashov, T. *et al.* Magnetic anisotropy and magnetization dymanics of individual atoms and clusters of Fe and Co on Pt(111) (2009). Accepted for publication in Phys. Rev. Lett.

[78] Bott, M., Hohage, M., Morgenstern, M., Michely, T. & Comsa, G. New approach for determination of diffusion parameters of adatoms. *Phys. Rev. Lett.* **76**, 1304–1307 (1996).

[79] Crommie, M. F., Lutz, C. P. & Eigler, D. M. Spectroscopy of a single adsorbed atom. *Phys. Rev. B* **48**, 2851 (1993).

[80] Etz, C., Zabloudil, J., Weinberger, P. & Vedmedenko, E. Y. Magnetic properties of single atoms of Fe and Co on Ir(111) and Pt(111). *Phys. Rev. B* **77**, 184425 (2008).

[81] Leuenberger, M. N. & Mucciolo, E. R. Berry-phase oscillations of the Kondo effect in single-molecule magnets. *Phys. Rev. Lett.* **97**, 126601 (2006).

[82] Otte, A. F., Ternes, M., von Bergmann, K., Loth, S., Brune, H., Lutz, C. P., Hirjibehedin, C. F. & Heinrich, A. J. The role of magnetic anisotropy in the Kondo effect. *Nature Phys.* **4**, 847–850 (2008).

[83] Herrmannsdoerfer, T., Rehmann, S., Wendler, W. & Pobell, F. Magnetic properties of highly diluted $PdFe_x$ and $PtFe_x$ alloys. Part I. Magnetization at Kelvin temperatures. *J. Low Temp.* **104**, 49 (1996).

[84] Ternes, M., Lutz, C. P., Hirjibehedin, C. F., Giessibl, F. J. & Heinrich, A. J. The force needed to move an atom on a surface. *Science* **319**, 1066 (2008).

[85] Meier, F., Zhou, L., Wiebe, J. & Wiesendanger, R. Revealing magnetic interactions from single-atom magnetization curves. *Science* **320**, 82–86 (2008).

[86] Hirjibehedin, C. F., Lin, C.-Y., Otte, A. F., Ternes, M., Lutz, C. P., Jones, B. A. & Heinrich, A. J. Large magnetic anisotropy of a single atomic spin embedded in a surface molecular network. *Science* **31**, 1199 (2007).

[87] Bertaina, S., Gambarelli, S., Mitra, T., Tsukerblat, B., Müller, A. & Barbara, B. Quantum oscillations in a molecular magnet. *Nature* **453**, 203–206 (2008).

Acknowledgements

First of all, I would like to thank Prof. Wulf Wulfhekel for all the patience, guiding and support he has given me over these years.

I would also like to thank Prof. Georg Weiß for agreeing to be the second referee, and for investing time and effort into reading and commenting on this work.

I thank Dr. Arthur Ernst for providing the theoretical support for the experimental results.

I want also to thank Dr. Yasmine Nahas, my father Sergey Balashov and my wife Inna for reading the manuscript and providing me with a non-specialist impression of it.

I thank Tobias, Florian, Nicolai, Lukas, Annika, Stefan and Stefan for 'stupid' questions that are so difficult to answer and for occasionally giving me a hard time.

I want to thank Dr. Albert Takács for the Romanian jokes and Dr. Toshio Miyamachi for the Japanese ones.

Special thanks go to Dr. Monika Kaempfe for helping me through the bureaucratic catches during the first months of my life in Germany.

I am also grateful to all the people I met during these years in Germany, and who made my stay a pleasant one.

A separate mention goes to the group of Prof. Shigemasa Suga from Osaka, for accommodating and caring about me during the time spent in their group in Japan.

Deutsche Zusammenfassung

Vor 20 Jahren gab die Entdeckung des Riesenmagnetowiderstands dem Bereich der magnetischen Datenspeicherung einen großen Impuls. Die Anwendung des Magnetowiderstandseffektes in Leseköpfen von Festplatten erlaubt sehr hohe Speicherdichten und rief deshalb großes wissenschaftliches Interesse an magnetischen Nanostrukturen und dem Zusammenwirken zwischen dem elektrischen Strom und magnetischen Materialien hervor. Heutzutage bringt der Miniaturisierungstrend die Datendichte auf einige GBit/Zoll^2, entsprechend die magnetischen Bits auf eine Größe von $25 \times 80\,\mathrm{nm}^2$. In diesem Größenbereich unterscheiden sich die Eigenschaften des magnetischen Systems sehr von makroskopischen Magneten, besonders in der Dynamik. Nanomagnetische Systeme lassen sich nicht durch Makrospinmodelle beschreiben. Ihr Verhalten in angeregten Zuständen muss durch elementare Anregungen des Magneten, d.h. Spinwellen oder Magnonen beschrieben werden. Leider eignen sich die traditionellen experimentellen Methoden der Magnonenuntersuchung nicht zur Erforschung von Nanostrukturen. Inelastische Neutronenstreuung benötigt große Proben aufgrund der schwachen Wechselwirkung mit Materie. Die laterale Auflösung von Brillouin-Lichtstreuung und ferromagnetischer Resonanz ist limitiert durch die Wellenlänge der verwendeten Photonen, und diese Techniken sind auf den zentralen Teil der Brillouin-Zone beschränkt.

In dieser Dissertation werden mit Hilfe der inelastischen Rastertunnelspektroskopie (IRTS) Anregungen von Magnonen untersucht. Die Abhängigkeit des Tunnelstroms I von der angelegten Spannung U wird gemessen. Ohne inelastische Anregungen ist $I(U)$ in der Nähe von E_F linear, da die Elektronen elastisch tunneln. Wenn die Energie der Elektronen hoch genug ist, um inelastische Anregungen zu erzeugen, wird die Tunnelleitfähigkeit vergrößert und der Tunnelstrom nimmt stark zu. In der zweiten Ableitung des Tunnelstroms $\mathrm{d}^2I/\mathrm{d}U^2$ erhält man am entsprechenden Spannungswert einen Peak. Auf diese Art können unterschiedliche inelastische Anregungen wie Phononen oder Plasmonen untersucht werden. In magnetischen Proben können auch Magnonen angeregt werden, wenn ein Austausch des Spins zwischen Elektron und Probe stattfindet. Bei diesem Prozess wird der Spin des Elektrons erhöht und die Magnetisierung der Probe reduziert. Die Erniedrigung der Magnetisierung entspricht der Erzeugung eines Magnons. Die hohe laterale Auflösung der IRTS erlaubt die Untersuchung von Magnonenanregungen

auf der Ångström-Skala.

In dieser Arbeit werden magnetische Systeme unterschiedlicher Dimension mit IRTS untersucht, von dreidimensionalen Fe-Kristallen bis zu einzelnen Co-Atomen auf Pt(111). Alle Experimente wurden im Ultrahochvakuum bei 4.3 K durchgefürt.

Die sorgfältige Betrachtung der auf Fe(100) gemessenen $\mathrm{d}^2I/\mathrm{d}U^2$-Spektren offenbart inelastische Strukturen im Bereich von 10 meV. Die Änderung dieser Strukturen mit dem äußeren Magnetfeld lassen auf einen magnetischen Ursprung der betrachteten Anregungen schließen. Die Streuwahrscheinlichkeit der Elektronen wurde zu 25 % bestimmt. Ähnliche Strukturen findet man in den Spektren auf dünnen Co-Schichten auf Cu(111). Die Intensität der Peaks steigt mit der Dicke der Co-Filme an, und man erhält eine mittlere freie Weglänge der tunnelnden Elektronen von 3 nm.

Aus der Asymmetrie der inelastischen Peaks bestimmen wir, dass die Wahrscheinlichkeit der Magnonanregung proportional zur Spin-Polarisation des Tunnelstroms ist. Die Analyse der Form der Peaks führt zur Erkenntnis, dass die Wechselwirkung zwischen tunnelnden Elektronen und den Elektronen der Probe keine Punktwechselwirkung ist, sondern durch delokalisierte Elektronenzustände bestimmt ist.

Diese Resultate zeigen, dass das Zusammenwirken zwischen elektrischem Strom und magnetischer Probe für kleine angelegte Spannungen größtenteils durch inelastische Prozesse bestimmt ist, und dass eine quantenmechanische Beschreibung benötigt wird, da die etablierte klassische elastische Beschreibung nicht ausreicht.

Um die Dispersion von Magnonen messen zu können, untersuchen wir auch Magnonen in dünnen Schichten von Co/Cu(100) und Ni/Cu(100). In dünnen Schichten ist die Dispersion senkrecht zur Oberfläche quantisiert und unterschiedliche Moden führen zu mehreren Peaks in $\mathrm{d}^2I/\mathrm{d}U^2$, die die ganze Brillouin-Zone aufspannen. Aus den Peakpositionen kann man die Dispersion aufbauen, wenn man für jeden Peak einen Wellenvektor q in der Form

$$q = \frac{\pi}{a}\frac{n}{N}, \quad n = 0, \ldots, N-1$$

aufträgt.

Die experimentellen $\mathrm{d}^2I/\mathrm{d}U^2$-Spektren zeigen allerdings etliche Peaks, deren genaue Anzahl von der Schichtdicke abhängt. Eine Dispersionskurve wird für jede Dicke erstellt. Für Co/Cu(100) ist die Dispersion von Magnonen fast unabhängig von der Schichtdicke und ähnelt der von Volumen-Proben. Eine kleine Verringerung der Magnonenenergie in dünnen Schichten lässt sich durch die Änderung der elektronischen Struktur erklären. Ansonsten folgt die Dispersion in dünnen Schichten der Dispersion eines fcc Co-Kristalls mit einer Spinwellensteifigkeit von 360 meV Å^2.

Die dünnen Schichten von Ni auf Cu(100) verhalten sich komplizierter als die Co-Schichten, und die Dispersion ist nicht einfach zu konstruieren. Theoretische Berechnungen von IRTS-Spektren werden durchgefürt, um die inelastischen Peaks richtig nummerieren zu können. In diesem Fall unterscheiden sich die Dispersionskurven von dünnen Schichten stark von denen dicker Proben. Die Energie der

Magnonen steigt in den Schichten doppelt so schnell an, wie in einem Ni-Kristall. Der Grund dieses Unterschieds ist noch nicht klar. Es ist wahrscheinlich ein Zeichen einer sehr starken Änderung der Elektronenstruktur.

Die atomare Auflösung des IRTS ermöglicht die Untersuchung eines magnetischen Systems, das nur aus einem Atom besteht. Durch atomare Manipulation können die Atome zusammengebracht werden, um Cluster (Dimere und Trimere) zu bilden. Die magnetischen Anregungen solcher Systeme besitzen keine Dispersion, sondern nur noch einzelne Energiewerte. Die Anzahl der Moden hängt von der Anzahl der Atome im Cluster und vom Spin des Clusters ab. In unseren Experimenten besitzen einzelne Atome nur eine Anregung, Dimere und Trimere zwei. Die Energie des ersten angeregten Zustands ist proportional zur magnetischen Anisotropie-Energie (MAE), d.h. der Energie, die man braucht, um den Spin des Clusters zu drehen. Diese Energie bestimmt die Stabilität des Spins und ist wichtig für die magnetische Datenspeicherung. Höhere Anregungzustände hängen auch von der Austauschkopplung zwischen den Atomen ab.

Wir haben Fe- und Co-Atomen auf Pt(111) untersucht. Die $\mathrm{d}^2I/\mathrm{d}U^2$ Spektren, gemessen auf einzelnen Atomen, haben eine symmetrische Peak-Dip-Struktur. Aus einer Gaußschen Anpassung an die Daten wird die Anregungsenergie bestimmt. Die Energie variiert für die einzelnen Messungen und den Endwert erhält man durch Mittelung. Damit die MAE bestimmt werden kann, wurden ab-initio-Rechnungen für die Spins von Fe und Co auf Pt(111) durchgeführt. Die resultierenden Werte für die MAE sind 6.5 meV für Fe und 10.2 meV für Co. Die Messung der Lebensdauer des angeregten Zustands ergibt 55 fs bzw. 20 fs für Fe bzw. Co.

In den Spektren der Dimere und Trimere erkennt man zwei inelastische Anregungen. Die erste Anregung ist die Drehung des Gesamt-Spins des Clusters und ist mit der MAE verbunden. Die zweite Anregung ist eine Anregung der inneren Spin-Struktur des Clusters. Die Energie dieser Anregung hängt von der Austauschkopplungskonstante ab. Die Analyse der Spektren liefert für die Konstante einen Wert von 16 meV.

Im Allgemeinen liefert IRTS viele interessante Eigenschaften magnetischer Nanostrukturen, die sich nicht mit anderen Methoden messen lassen. Die Anregungswahrscheinlichkeit, die Dispersion und die Lebensdauer magnetischer Anregungen in Nanostrukturen können mit IRTS bestimmt werden.